

University of Windsor

Scholarship at UWindor

Electronic Theses and Dissertations

Theses, Dissertations, and Major Papers

2012

Forming of Ferritic Stainless Steel Bipolar Plates

Lakshmi Ravi Narayan
University of Windsor

Follow this and additional works at: <https://scholar.uwindsor.ca/etd>

Recommended Citation

Ravi Narayan, Lakshmi, "Forming of Ferritic Stainless Steel Bipolar Plates" (2012). *Electronic Theses and Dissertations*. 205.

<https://scholar.uwindsor.ca/etd/205>

This online database contains the full-text of PhD dissertations and Masters' theses of University of Windsor students from 1954 forward. These documents are made available for personal study and research purposes only, in accordance with the Canadian Copyright Act and the Creative Commons license—CC BY-NC-ND (Attribution, Non-Commercial, No Derivative Works). Under this license, works must always be attributed to the copyright holder (original author), cannot be used for any commercial purposes, and may not be altered. Any other use would require the permission of the copyright holder. Students may inquire about withdrawing their dissertation and/or thesis from this database. For additional inquiries, please contact the repository administrator via email (scholarship@uwindsor.ca) or by telephone at 519-253-3000ext. 3208.

Forming of Ferritic Stainless Steel Bipolar Plates

by

Lakshmi Ravi Narayan

*A Thesis
Submitted to the Faculty of Graduate Studies
through Engineering Materials
in Partial Fulfillment of the Requirements for
the Degree of Master of Applied Science at the
University of Windsor
Windsor, Ontario, Canada
2012*

© 2012 Lakshmi Ravi Narayan

Forming of Ferritic Stainless Steel Bipolar Plates

by

Lakshmi Ravi Narayan

APPROVED BY:

Dr. S. Holger Eichhorn, Outside Program Reader
Department of Chemistry and Biochemistry

Dr. Daniel E. Green, Program Reader
Department of Mechanical, Automotive and Materials Engineering

Dr. Ahmet T. Alpas, Advisor
Department of Mechanical, Automotive and Materials Engineering

Dr. H. Hu, Chair of Defense
Department of Mechanical, Automotive and Materials Engineering

April 10, 2012

DECLARATION OF ORIGINALITY

I hereby certify that I am the sole author of this thesis and that no part of this thesis has been published or submitted for publication.

I certify that, to the best of my knowledge, my thesis does not infringe upon anyone's copyright nor violate any proprietary rights and that any ideas, techniques, quotations, or any other material from the work of other people included in my thesis, published or otherwise, are fully acknowledged in accordance with the standard referencing practices. Furthermore, to the extent that I have included copyrighted material that surpasses the bounds of fair dealing within the meaning of the Canada Copyright Act, I certify that I have obtained a written permission from the copyright owner(s) to include such material(s) in my thesis and have included copies of such copyright clearances to my appendix.

I declare that this is a true copy of my thesis, including any final revisions, as approved by my thesis committee and the Graduate Studies office, and that this thesis has not been submitted for a higher degree to any other University or Institution.

ABSTRACT

The effect of temperature and lubrication on the stamping of ferritic stainless steel bipolar plates has been studied. Stamping of micro-scale bipolar plate channels in ferritic stainless steel foils of 75 μm thickness was carried out at 25, 100 and 200 °C with stamping loads varying between 36 and 56 kN, without and with lubrication. In unlubricated stamping, high contact friction between the sheet and the die caused strain localisation that increased with stamping load and temperature, and heavy surface damage was observed. Boron nitride, tungsten disulphide and molybdenum disulphide were used as solid lubricants in the process. No necking was observed at 200 °C, the strain distribution improved with temperature and the surface damage was considerably reduced, although WS_2 and MoS_2 produced transfer layers on the surfaces. MoS_2 -lubrication, 200 °C and stamping loads between 45 and 50 kN have been identified as the most suitable conditions for this process.

ACKNOWLEDGEMENTS

I would like to thank first and foremost my advisor Dr. A. T. Alpas for entrusting me with such a challenging and engaging project. His patient guidance and experience were instrumental in bringing the project this far.

My committee members Dr. D. E. Green and Dr. S. H. Eichhorn provided valuable suggestions that set the project in the right direction, and their experienced insight provided a sharper perspective. Dr. A. T. Morales of GM Global Research and Development has been of immense support from the inception of this project and has guided it to where it stands now. I also acknowledge the assistance provided by Mr. R. Slade in making the dimensional measurements with automatic microscopy and Mr. J. Lasceski in operating the punch stretching machine.

I cannot thank Mr. A. Jenner enough for the technical assistance he has provided me from the very start, including the design and fabrication of the stamping equipment used in this work. His positive attitude to solve any problem this project presented, and his speed and efficiency in delivering all of my requests allowed this project to maintain its tight schedule. Dr. S. Bhowmick initiated the stamping project with the construction of the machine. I also thank Mr. P. Seguin, Mr. S. Budinsky and the members of the Technical Support Center of the University of Windsor for their technical assistance, and Ms. B. Tattersall for her administrative assistance during my study.

I thank my friends and my fellow researchers of the NSERC/General Motors of Canada Industrial Research Chair, to whom I turned to for help on a daily basis. In particular, I thank Dr. S. Das, Dr. S. Dey and Dr. M. Iqbal, who made it easy for me. Most of all, I thank my brother Mr. A. R. Narayan, for without his efforts I could not have embarked on this graduate program.

TABLE OF CONTENTS

DECLARATION OF ORIGINALITY	iii
ABSTRACT	iv
ACKNOWLEDGEMENTS	v
NOMENCLATURE	x
LIST OF TABLES	xii
LIST OF FIGURES	xiii
<u>CHAPTER 1: Introduction</u>	<u>1</u>
1.1 Metallic Bipolar Plates for Polymer Electrolyte Membrane Fuel Cells	1
1.2 Motivation for this Research	3
1.3 Objectives of this Research	4
<u>CHAPTER 2: Review of Literature</u>	<u>5</u>
2.1 Introduction.....	5
2.2 The Stamping Process.....	5
2.2.1 <i>Deformation of sheet metal in the stamping process</i>	5
2.2.2 <i>Failure by necking in sheet metals</i>	11
2.2.3 <i>Springback</i>	13
2.2.4 <i>Tribology of the stamping process</i>	14
2.3 Ferritic Stainless Steels.....	19
2.3.1 <i>Material selection and alloy design</i>	22
2.3.2 <i>The deformation behaviour of ferritic stainless steels</i>	23
2.3.3 <i>The yielding phenomenon and strain ageing</i>	25
2.3.4 <i>The dislocation theory of yielding</i>	30
2.4 Lubrication by Lamellar Solids	34
2.5 Summary of the Review of Literature	38
<u>CHAPTER 3: Materials and Experimental Methods.....</u>	<u>39</u>
3.1 Introduction.....	39
3.2 Materials and Microstructures	39

3.2.1 <i>Microstructure and properties of the 30 % cr ferritic stainless steel</i>	39
3.3 Description of the Stamping Experiments.....	42
3.3.1 <i>Fabrication and operation of the stamping machine</i>	42
3.3.2 <i>Procedure of the stamping experiments</i>	45
3.4 Measurement and Characterisation.....	48
3.4.1 <i>Strain measurement</i>	48
3.4.2 <i>Springback measurement: channel depth</i>	50
3.4.3 <i>Microstructural characterisation</i>	51
3.4.4 <i>Characterisation of stamped surfaces</i>	51
<u>CHAPTER 4: Experimental Results</u>	<u>52</u>
4.1 Introduction.....	52
4.2 Distribution of Strain along the Stamped Channel	52
4.2.1 <i>Unlubricated stamping at elevated temperatures</i>	54
4.2.2 <i>Lubricated stamping at elevated temperatures</i>	57
4.3 Microstructural Evolution.....	62
4.3.1 <i>Unlubricated stamping</i>	62
4.3.2 <i>Lubricated stamping at elevated temperatures</i>	64
4.4 Springback Effects.....	66
4.4.1 <i>Channel depth</i>	66
4.5 Roughening and Morphology of Stamped Surfaces	67
4.5.1 <i>Roughness of stamped surfaces</i>	67
4.5.2 <i>Surface morphology of stamped channels</i>	73
<u>CHAPTER 5: Discussion of Results</u>	<u>81</u>
5.1 Introduction.....	81
5.2 Tribology of the Stamping Process.....	81
5.3 Effect of Temperature on the Process.....	84
5.4 Effect of Lubricants on the Process	86
5.5 Surface Roughening and Evolution of Stamped Surfaces	87
5.6 Optimum Processing Window	89
5.7 Behaviour of the Alloy	91

<u>CHAPTER 6: Summary and Conclusions</u>	<u>93</u>
6.1 Warm Unlubricated Stamping of Ferritic Stainless Steel.....	93
6.2 Lubricated Warm Stamping of Ferritic Stainless Steel	94
6.3 Recommendations for Future Work	95
REFERENCES	96
VITA AUCTORIS	101

NOMENCLATURE

Abbreviations

EDS	Energy-Dispersive X-Ray Spectroscopy
ICP	Inductively-Coupled Plasma spectroscopy
PEMFC	Polymer Electrolyte Membrane Fuel Cell
PLC	Portevin-Le-Chatelier
SEM	Scanning Electron Microscopy

Symbols

A	Cross-sectional area
D	Diffusivity
E	Young's modulus
G	Elastic (shear) modulus
P	Applied load
R	Lankford ratio (plastic anisotropy coefficient, radial distance from core)
U	Energy of interaction of solute atom and mobile dislocation
X	Slope of the plot of punch radius versus punch-sheet interface boundary
b	Burger's vector
l	Distance between solute atom and mobile dislocation
n	Strain hardening exponent
p	Pressure at the interface
r_0	Point of inflection in the load-displacement plot
t	Time
ν	Poisson's ratio, velocity of dislocation
ν_c	Critical speed of dislocation
$\bar{\nu}$	Mean dislocation velocity
θ	Angle between the punch axis and the normal to the sheet
λ	Slip distance
ε	True strain
ϵ	Elastic strain
ρ	Radius of the punch, dislocation density

σ	True stress
σ_y	Yield stress
τ	True shear stress

LIST OF TABLES

Chapter 3: Materials and Experimental Methods

Table 3.1: Composition of the ferritic stainless steel used in this work.....	39
Table 3.2: The conditions under which stamping was carried out.....	47

Chapter 5: Discussion

Table 5.1: The text matrix incorporating the results of this work to aid in the determination of the optimum processing window.....	91
---	----

LIST OF FIGURES

Chapter 1: Introduction

Figure 1. 1: Schematic of the arrangement of the components of a PEM fuel cell and the working [7].....	2
---	---

Chapter 2: Review of Literature

Figure 2. 1: Schematic of a polymer electrolyte membrane fuel cell stack with repeating units [1].	5
Figure 2. 2: Schematic of the stamping process for the forming of sheet metal products [57].....	6
Figure 2. 3: (a) Schematic representation of the hemispherical punch-stretching process, (b) a partially deformed sheet with circle grids for strain measurements (c) geometry of the punch-stretching process [13].	7
Figure 2. 4: The forming limit diagram showing the strain paths for different types of forming [13].	8
Figure 2. 5: Distribution of radial and circumferential strains in a steel sheet upon unlubricated punch stretching, showing the shifting of the strain peak from the pole of the punch [13].	10
Figure 2. 6: Schematic of the springback effects in plane-strain channel stamping after removal of the deforming load [21].	13
Figure 2. 7: Distribution of circumferential strain in punch stretching of annealed copper and brass, from finite element simulation [27]. The forming limit shows a 50 % increase with a 0.2 decrease in the coefficient of friction.....	16
Figure 2. 8: The model of punch stretching used to determine the coefficient of friction between the sheet and the die during forming [14].....	17
Figure 2. 9: Tribological model of the deep-drawing process which explains the nature of contact along different regions of the sheet due to the geometry of the process. Regions 1 and 2 are clamped under the blank-holder and do not experience deformation due to the frictional force holding the sheet in place.....	18
Figure 2. 10: The Schaeffler diagram which aids in determining the phase composition of stainless steels. At 30% Cr, the stainless steel is fully ferritic [29].	20
Figure 2. 11: The binary Iron-Chromium phase diagram [58].	21
Figure 2. 12: The precipitation diagram for ferritic stainless steel AISI type 444 [59]....	21
Figure 2. 13: The tensile deformation behaviour of a 40 % Cr ferritic stainless steel showing serrated flow and low uniform elongation [37].....	24

Figure 2. 14: Ferritic stainless steels deform by wavy slip due to the absence of a distinct slip system in the bcc crystal structure. Surfaces of deformed tensile specimens show wavy slip bands because mobile dislocations change slip systems often during plastic deformation [38]. 24

Figure 2. 15: (a) the different types of serrations that can occur during tensile deformation and (b) the temperature and strain-rate dependence of the different types of serrations in a ferritic stainless steel [49]. 28

Figure 2. 16: Strain ageing quantified by the strain ageing parameter for a ferritic stainless steel [60]. 30

Figure 2. 17: The crystal structure of hexagonal Boron Nitride. The dotted lines represent weak van der Waals bonds permitting the ‘easy shear’ of the planes bonded thus [61]. 35

Figure 2. 18: (a) The crystal structure of molybdenum disulphide [52], and (b) scanning electron microscope image of the lamellar arrangement and displacement of the hexagonal planes of molybdenum disulphide [62]. 37

Chapter 3: Materials and Experimental Methods

Figure 3. 1: (a) The microstructure of the sheet parallel to the surface and (b) microstructure of the cross-section of the sheet showing the equiaxed grains of the annealed condition. 40

Figure 3. 2: (a) SEM micrograph of the coarse precipitates aligned along the rolling direction in the cross-section of the ferritic stainless steel and (b) EDS mapping of the area in (a) identifying the elements present in the precipitates as Ti, Al, V and N. 41

Figure 3. 3: The experimental stamping machine used in this work showing the punch and die assembly, with the cartridge heaters and thermocouple used to maintain the test temperatures. 42

Figure 3. 4: (a) A closer view of the die set that was used the stamping the bipolar plate micro-channels along with a stamped foil. (b) Cross-sectional dimensions of the bipolar plate channels that were evaluated in this work. 44

Figure 3. 5: SEM image of the distribution of lubricant particles over the ferritic stainless steel sheet surface applied using the technique described, (a) boron nitride, (b) tungsten disulphide and (c) molybdenum disulphide. 47

Figure 3. 6: The procedure employed in measuring tensile strains along the channel using Vicker’s micro-hardness indents..... 48

Figure 3. 7: The method of measurement used for calculating thickness strains in the stamped channel. Sheet thickness and channel depth measurements are made from polished cross-sections of the channels using an optical microscope as shown above, (a) in the seven locations indicated and (b) at 30 µm intervals for a finer strain distribution. 49

Figure 3. 8: The method of measuring channel depth using optical microscopy. 51

Chapter 4: Experimental Results

- Figure 4. 1: (a) Locations of Vicker's indents along the cross-section of the channel after stamping. They were initially placed 100 μm apart and their spacing after stamping was measured using optical microscopy to calculate the tensile strain, plotted in (b). Through-thickness strains measured in the same locations as indicated in (a) are plotted in (c) to confirm plane-strain conditions..... 53
- Figure 4. 2: Through-thickness strain along the channel at the seven locations indicated in Figure 3. 7 under unlubricated conditions at (a) 25 $^{\circ}\text{C}$, (b) 100 $^{\circ}\text{C}$ and (c) 200 $^{\circ}\text{C}$. 55
- Figure 4. 3: Cross-sections of the channels stamped under unlubricated conditions at (a) 25 $^{\circ}\text{C}$, (b) 100 $^{\circ}\text{C}$ and (c) 200 $^{\circ}\text{C}$ 56
- Figure 4. 4: Through thickness strain along the channel stamped with boron nitride lubrication at (a) 25 $^{\circ}\text{C}$, (b) 100 $^{\circ}\text{C}$ and (c) 200 $^{\circ}\text{C}$ 58
- Figure 4. 5: Through thickness strain along the channel stamped with tungsten disulphide lubrication at (a) 25 $^{\circ}\text{C}$, (b) 100 $^{\circ}\text{C}$ and (c) 200 $^{\circ}\text{C}$ 59
- Figure 4. 6: Through thickness strain along the channel stamped with molybdenum disulphide lubrication at (a) 25 $^{\circ}\text{C}$, (b) 100 $^{\circ}\text{C}$ and (c) 200 $^{\circ}\text{C}$ 60
- Figure 4. 7: Thickness strains calculated from sheet thickness measured at 30 μm intervals along the stamped channel. (a) Locations of measurement on channel stamped without lubrication at 200 $^{\circ}\text{C}$ and (b) the strains at these locations, (c) locations of measurement on channel stamped with WS_2 at 200 $^{\circ}\text{C}$ and (d) the strains at these locations, (e) locations of measurement on channel stamped with MoS_2 at 200 $^{\circ}\text{C}$ and (f) the strains at these locations..... 61
- Figure 4. 8: The cross-sectional microstructures of the channels stamped without lubrication at (a) 25 $^{\circ}\text{C}$, (b) 100 $^{\circ}\text{C}$ and (c) 200 $^{\circ}\text{C}$. (Electrolytically etched with 60 % HNO_3)...... 63
- Figure 4. 9: The cross-sectional microstructures of the channels stamped at 200 $^{\circ}\text{C}$ with (a) BN, (b) WS_2 and (c) MoS_2 . (Electrolytically etched with 60 % HNO_3). 65
- Figure 4. 10: Variation of channel depth with load at 25, 100 and 200 $^{\circ}\text{C}$, (a) unlubricated, (b) BN, (c) WS_2 and (d) MoS_2 66
- Figure 4. 11: The variation of surface roughness of the stamped channels with stamping load on the punch and die sides stamped under unlubricated conditions at (a) 25 $^{\circ}\text{C}$, (b) 100 $^{\circ}\text{C}$ and (c) 200 $^{\circ}\text{C}$ 69
- Figure 4. 12: The variation of surface roughness of the stamped channels with stamping load on the punch and die sides stamped with boron nitride lubrication conditions at (a) 25 $^{\circ}\text{C}$, (b) 100 $^{\circ}\text{C}$ and (c) 200 $^{\circ}\text{C}$ 70

Figure 4. 13: The variation of surface roughness of the stamped channels with stamping load on the punch and die sides stamped with tungsten disulphide lubrication conditions at (a) 25 °C, (b) 100 °C and (c) 200 °C.....	71
Figure 4. 14: The variation of surface roughness of the stamped channels with stamping load on the punch and die sides stamped with molybdenum disulphide lubrication conditions at (a) 25 °C, (b) 100 °C and (c) 200 °C.....	72
Figure 4. 15: SEM images of channel surfaces stamped without lubrication at 200 °C on (a) the punch side and (b) the die side. (c) and (d) show high magnification images of the punch and die sides respectively.....	74
Figure 4. 16: SEM images of channel surfaces stamped without lubrication at 25 °C on the (a) inside and (b) outside of the die radius.....	75
Figure 4. 17: SEM images of the surfaces stamped at 200 °C with BN lubrication on (a) the punch side and (b) the die side.....	76
Figure 4. 18: SEM images of the surfaces stamped at 200 °C with WS ₂ lubrication on (a) the punch side and (b) the die side. (c) Backscattered electron image of the location corresponding to (a) showing bright patches indicative of the presence of the heavier tungsten in the transfer layers, whereas the backscattered electron image of the die side in (d) corresponding to (b) indicates the absence of tungsten and therefore any transfer layers.....	77
Figure 4. 19: SEM images of the surfaces stamped at 200 °C with MoS ₂ lubrication on (a) the punch side and (b) the die side. (c) and (d) are backscattered electron images corresponding to (a) and (b) respectively, and bright patches in both images indicate the presence of transfer layers containing molybdenum on both the punch and die sides of the stamped channel.....	78
Figure 4. 20: SEM images of the transfer layers formed on surfaces stamped at 200 °C with MoS ₂ lubrication showing the difference in morphology of the transfer layers formed on the two sides of the channel. (a) Punch side transfer layer assuming a lamellar morphology, (b) die side transfer layer of an agglomerated morphology and (c) the corresponding backscattered electron image of (b).	79
Figure 4. 21: Nature of damage made by the lubricant particles on the die-side of the channel stamped at 100 °C with BN lubrication.....	80

Chapter 5: Discussion

Figure 5. 1: Schematic of the forces acting on a sheet by the die during a channel stamping process.....	82
Figure 5. 2: Seven zones demarcated on the channel, where the deformation is distinctly different due to the different natures of contact in these locations and geometry of the process.....	84
Figure 5. 3: The major limiting criteria under unlubricated warm stamping conditions as a function of temperature and stamping load.	85

CHAPTER 1: Introduction

1.1 Metallic Bipolar Plates for Polymer Electrolyte Membrane Fuel Cells

Polymer electrolyte membrane fuel cells, or proton exchange membrane fuel cells (PEMFC) are the most promising alternative energy fuel source for automotive applications. Bipolar plates are the structural components of the PEMFC and act as an anode on one side and cathode on the other. They carry intricate flow fields for the transport of oxygen, hydrogen and water in order to distribute the reaction over the cross-section of the fuel cell [1], as seen in Figure 1. 1.

The functions of a bipolar plate are:

1. To separate the fuel cell into 200 to 400 individual cells
2. To carry an intricate network of channels that distributes the flow of hydrogen, oxygen (reactants) and water (product) over its surface area
3. To allow the passage of protons (hydrogen ions) through its thickness
4. To resist corrosion in the acidic environment of the fuel cell

The material selected for polymer electrolyte membrane fuel cells must fulfil the following requirements [2]:

1. Corrosion resistance in the fuel cell environment
2. Low electrical contact resistance
3. Formability into a low-volume and lightweight plate with intricate flow fields
4. Low cost

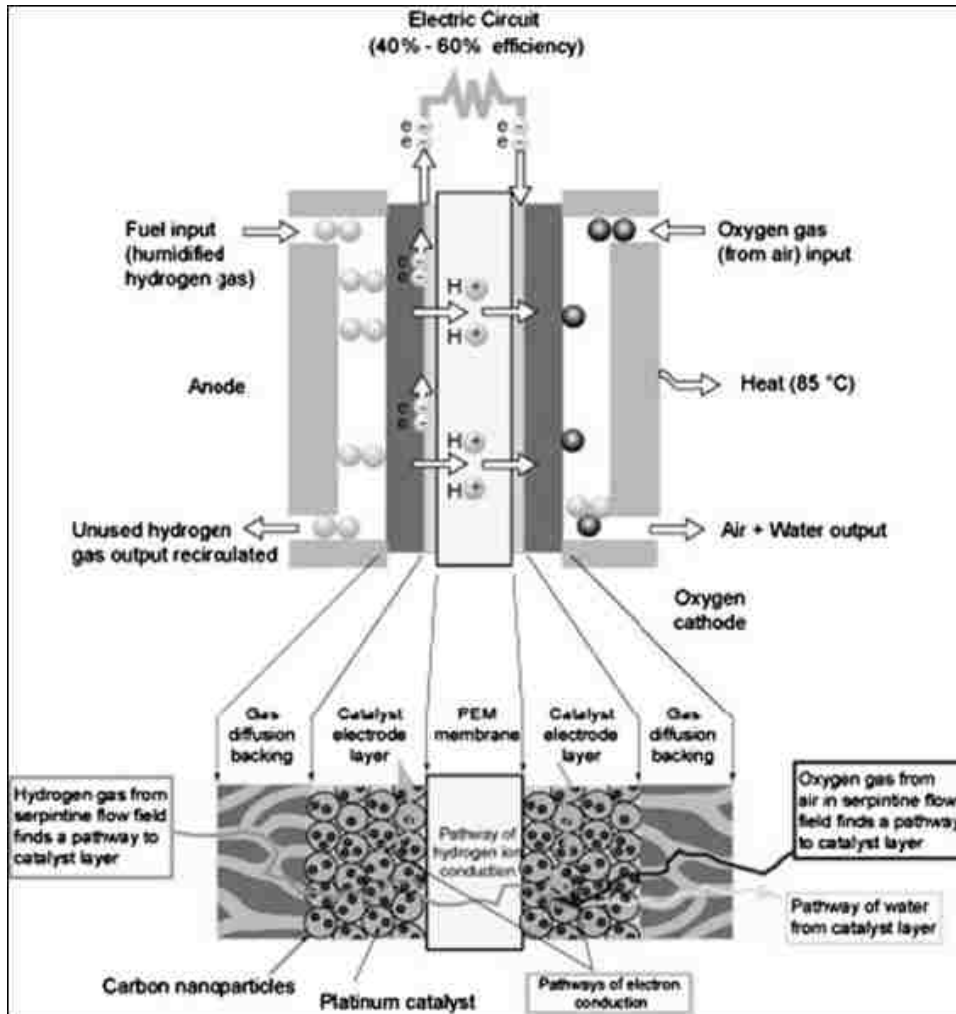


Figure 1. 1: Schematic of the arrangement of the components of a PEM fuel cell and the working [7].

Currently, bipolar plates are manufactured out of graphite and polymer-composites which have good electrical and corrosion properties, but are bulky, difficult to manufacture (they require machining) and are too expensive for commercial applications. Stamped metallic bipolar plates have the advantage of thin sections and mass-production at low cost. Metallic materials which have the electrical properties and corrosion resistance required of bipolar plate materials are not economical [3], such as titanium, aluminium and austenitic stainless steels (due to the large amounts of nickel in the alloys). Ferritic stainless steels have

the potential to replace these materials [4], but their formability must be better understood in order to manufacture them economically and effectively.

1.2 Motivation for this Research

Fuel cells are currently in the prototype stage. The commercialisation of fuel cells and their replacement of existing internal combustion engines require a cost reduction of the fuel cell components. Bipolar plates constitute a large percentage of the total cost of the fuel cell; an average automobile fuel cell requires 200 to 400 bipolar plates. In addition, they function in a harsh environment for which they must have improved corrosion and electrical properties. Metallic bipolar plates can achieve the cost, manufacturing and performance targets if these are better understood. It is known that the processing method and parameters affect the performance of the bipolar plate in terms of corrosion and electrical behaviour [5,6]. This work was aimed at understanding the stamping of thin foils of ferritic stainless steel to effectively manufacture this component, in the first step towards tailoring the processing conditions to impart optimum corrosion and electrical properties to the finished product.

Further steps in this larger picture involve testing the stamped samples in simulated fuel cell corrosion tests, measuring their electrical contact resistance and studying their mating with the gas diffusion layer. These are all primarily dependent on the surface roughening during the processing and also on the distribution of the strain along the channel. Further, the efficiency of the cell depends on the conformance of the physical dimensions to the design dimensions. This work provides useful information about the manufacturing process towards this end, and lays the groundwork for future work in this research.

1.3 Objectives of this Research

The objectives of this research were to improve the quality of stamped bipolar plate channels in 75- μm -thick ferritic stainless steel foils using lamellar-solid lubrication (boron nitride, tungsten disulphide, molybdenum disulphide):

1. In the 25 to 200 °C temperature range
2. In the 40 to 60 kN stamping load range

Where the quality of the stamping is decided on the basis of:

1. Dimensional accuracy (reduced springback)
2. No failure (thinning, necking, tearing)
3. Low surface damage and minimal surface roughening

CHAPTER 2: Review of Literature

2.1 Introduction

This chapter reviews the literature available to support the feasibility of the forming of ferritic stainless steel bipolar plates. It describes the physical metallurgy of the ferritic stainless steels, the deformation behaviour of this material and the tribological issues in the stamping process. Lamellar solids and their role as lubricants are discussed thereafter as a possible means of improving the stamping formability of the material selected for this application.

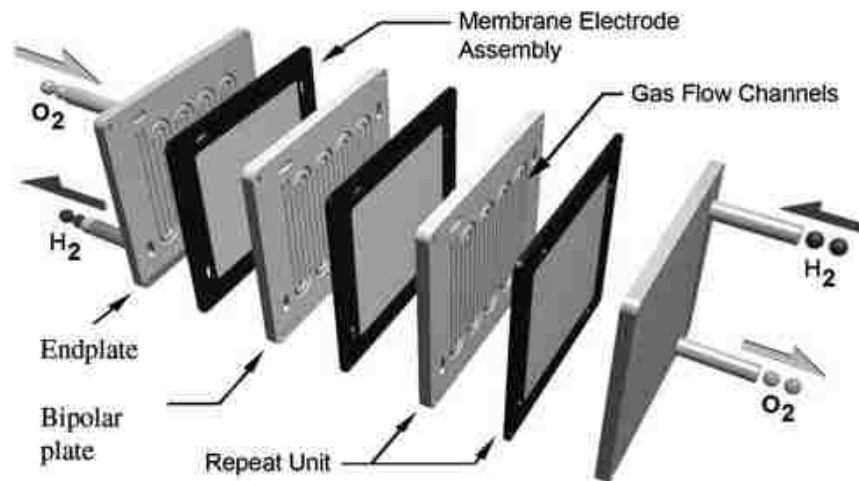


Figure 2. 1: Schematic of a polymer electrolyte membrane fuel cell stack with repeating units [1].

2.2 The Stamping Process

2.2.1 Deformation of sheet metal in the stamping process

Bipolar plates are structural and functional components of the PEMFC and they are located in the fuel cell as shown in Figure 2. 1. Stamping is the most efficient process for manufacturing these. Stamping is a sheet metal forming process in which a sheet of metal is

pressed under high pressure and speed between a punch and die carrying the desired shape as illustrated in a schematic of the process in Figure 2. 2.

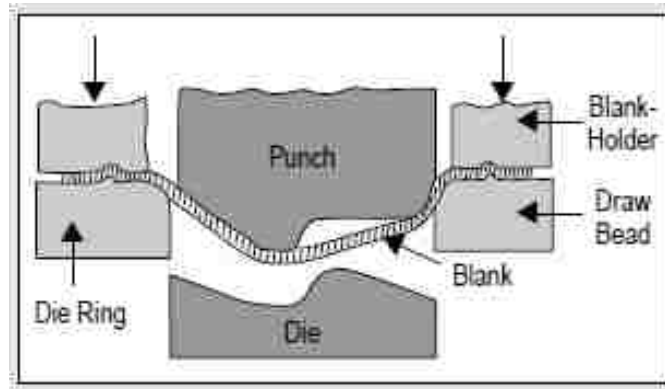


Figure 2. 2: Schematic of the stamping process for the forming of sheet metal products [57].

Common applications are the production of car-body panels on a large scale and PEMFC bipolar plates in the micro-scale (which is more correctly, embossing). The advantages of stamping are high-rate mass-production, elevated temperature processing and a wide range of geometries.

Stamping formability is evaluated by the hemispherical punch-stretching test, to determine the limiting strains which can be applied during the process, in an experiment described in Figure 2. 3. Strains measured from this test are charted in a forming limit diagram (FLD) and a typical FLD is shown in Figure 2. 4. Forming limit diagrams help identify the limit strains that can be safely applied in sheet-metal forming operations and also the strain-path [8]. Grids electrochemically etched onto the surface of the sheet prior to punch stretching or stamping aid in the measurement of the biaxial strain distribution over the sheet-metal product [9]. Forming limit diagrams as a function of temperature, strain rate

or strain path help design sheet-metal stamping products and processes, and are an important method for the automotive industry [10].

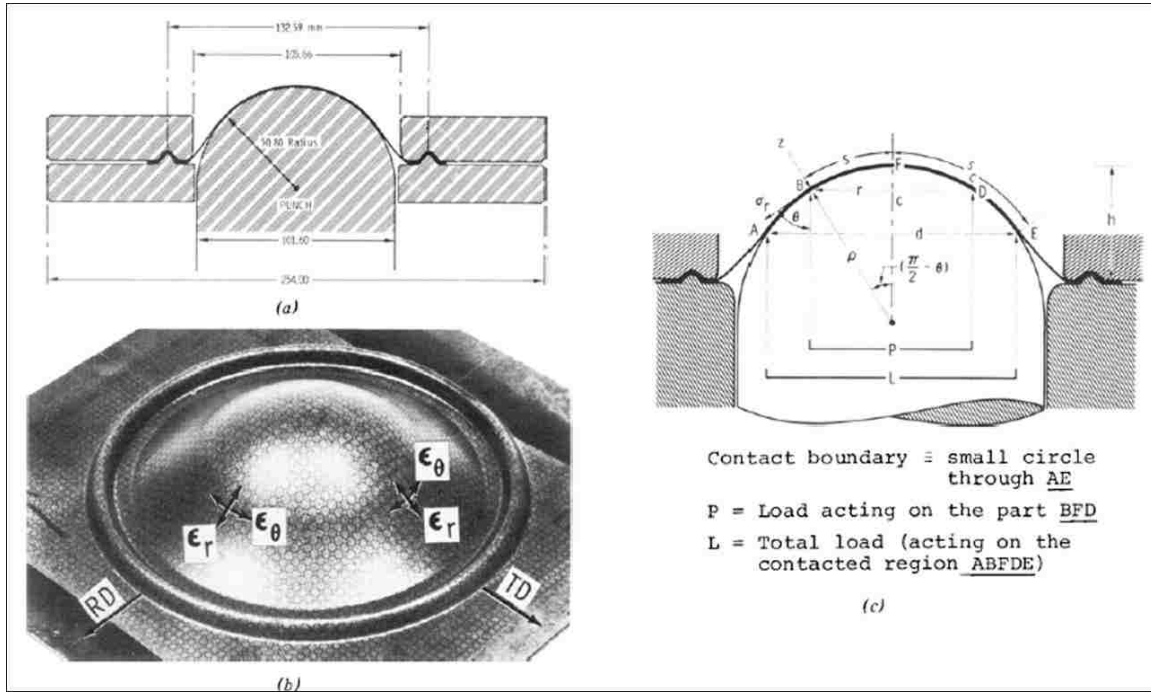


Figure 2. 3: (a) Schematic representation of the hemispherical punch-stretching process, (b) a partially deformed sheet with circle grids for strain measurements (c) geometry of the punch-stretching process [13].

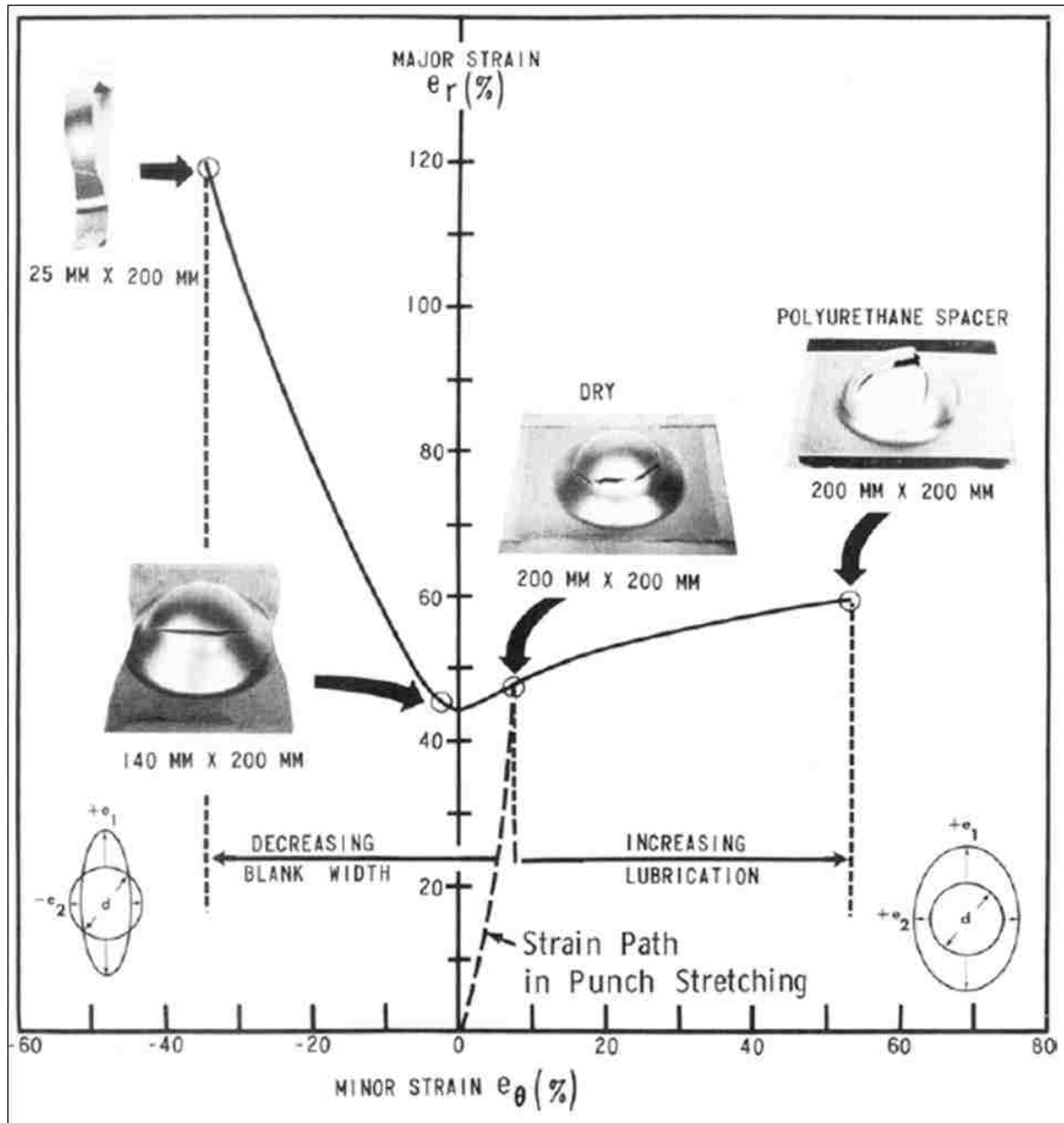


Figure 2. 4: The forming limit diagram showing the strain paths for different types of forming [13].

Punch stretching is a case of out-of-plane biaxial stretching, different from in-plane biaxial stretching [11]. In-plane sheet deformation does not encounter flow localisation due to friction between the punch and the sheet opposing deformation, and instability is caused by a previously existing inhomogeneity in the sheet. Marciniak and Kuczynski established the instability criterion for in-plane biaxial stretching by assuming the sheet to possess some inhomogeneity initially [12]. This is considered to be a thinned trough normal to the principal strain direction pre-existing in the sheet. In out-of-plane punch stretching, there is a flow localisation caused during the deformation due to the resistance to deformation caused by the frictional force in those parts of the sheet in contact with the punch as opposed to the freely deforming sheet held at one end under the blank holding force and in contact with the punch at the other. If the coefficient of friction due to the contact with the punch is disregarded, the centre of the sheet, that is at the pole of the punch experiences the greatest strain, due to which the failure should occur at this point. But the friction between the punch and the sheet is always finite, due to which, the location of the failure in stamping is always offset from the pole [13] (Figure 2. 5).

In a punch stretching operation, the deforming sheet can be divided into three zones in which the behaviour is different due to the die geometry and contact nature [14]. The first is the region that is in contact with the punch where the plastic deformation in biaxial tension is countered by the frictional force of contact with the punch surface. The second is the freely deforming region that is not in contact with any surface between the part of the sheet in contact with the punch and that part held under the blank-holding force. The third region is that held under the die which deforms by circumferential contraction if the punch stretching has axial symmetry.

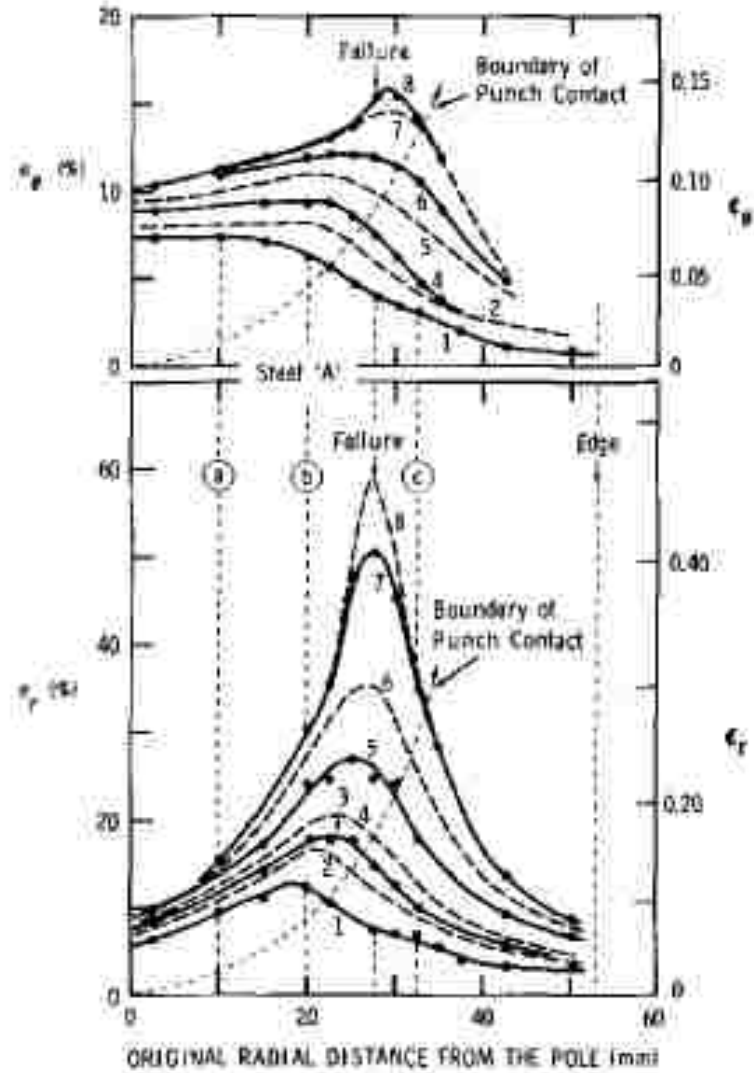


Figure 2. 5: Distribution of radial and circumferential strains in a steel sheet upon unlubricated punch stretching, showing the shifting of the strain peak from the pole of the punch [13].

The effect of the coefficient of friction on the forming limit curve by numerical analyses show that lower coefficient of frictions offset the failure limits to higher strains [15]. This is because the strain distribution is more uniform over the entire sheet, and under lubricated conditions, there is a most favourable even distribution of strains. There is sufficient evidence to show that a control over the friction between the sheet and the die can

be practically applied to improving the forming limits during stamping for a given set of processing parameters [14].

2.2.2 Failure by necking in sheet metals

Necking is the onset of failure in sheet metal forming and may be of two kinds, diffuse or localised [16]. Localised necking occurs when the instantaneous rate of strain hardening is balanced by the rate of geometric softening (caused by the decrease in cross-sectional area) and occurs only under conditions of plane strain [17]. Channel stamping is closely approximated to plane strain conditions because the width strain is negligible compared to the thickness strain, which can thus be considered equal to the longitudinal strain [18].

An analysis of necking in thin sheets stretched in tension under conditions of plane strain follows, as given by Hill in 1952 [17]. The rate of strain hardening with an increase in the axial force P keeping the cross-sectional area A instantaneously constant is:

$$\frac{1}{A} \left(\frac{\partial P}{\partial \varepsilon_1} \right) \Big|_A = \frac{d\sigma_1}{d\varepsilon_1} \quad (2.1)$$

The strain-induced geometrical softening due to change in the cross-sectional area at a constant flow stress is:

$$\frac{1}{A} \left(\frac{\partial P}{\partial \varepsilon_1} \right) \Big|_{\sigma_1} = \sigma_1 \frac{dA/A}{d\varepsilon_1} \quad (2.2)$$

Under conditions of plane strain, (where R is the Lankford ratio):

$$\frac{dA}{A} = -\left(\frac{1}{1+R}\right)d\varepsilon_1 \quad (2.3)$$

Substituting dA/A and equating the strain hardening and geometric softening,

$$\frac{d\sigma}{d\varepsilon} = \frac{\sigma}{1+R} \quad (2.4)$$

For a power-hardening material,

$$\frac{d\sigma}{d\varepsilon} = n \frac{\sigma}{\varepsilon} \quad (2.5)$$

Here, n is the strain hardening exponent. This gives the strain at local instability, ε_l to be:

$$\varepsilon_l = n(1+R) \quad (2.6)$$

Large values of n and R offset the localised necking to higher strains and are beneficial for forming operations such as plane strain draw forming. The angle θ between the localised neck and the tensile axis is found from the Mohr's circle of the above strain state which yields:

$$\cos(180 - 2\theta) = (1 - 2R)^{-1} \quad (2.7)$$

$$\tan\theta = \sqrt{\frac{(1+R)}{R}} \quad (2.8)$$

For isotropic materials and sheet metal in the annealed temper, this angle θ is 54.7° [18]. Therefore necking, as with other localisation effects such as shear bands and Lüders bands occur at an angle of around 55° with the tensile axis [19].

2.2.3 Springback

Springback is a major dimensional concern in sheet-metal stamping, which is attributed to the elastic unloading of a part after stamping. The effect of springback on a sheet stamped into a channel is illustrated in Figure 2. 6.

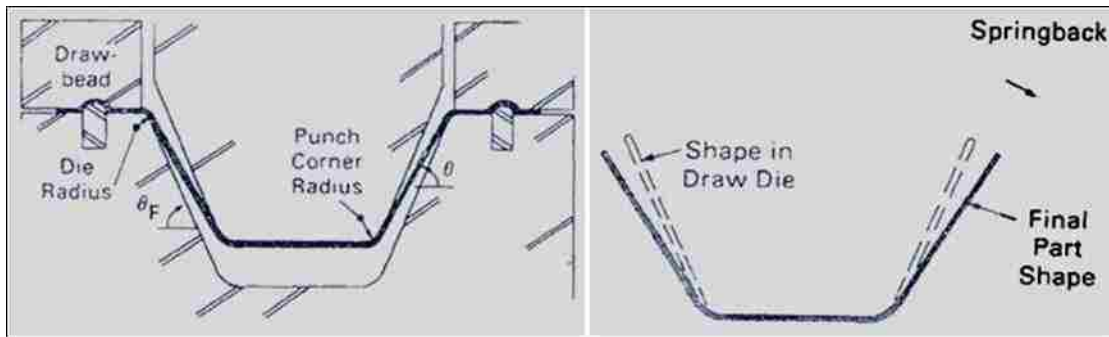


Figure 2. 6: Schematic of the springback effects in plane-strain channel stamping after removal of the deforming load [21].

Strain hardening behaviour is important to the springback nature of a material, as are the ratio of the punch radius to the sheet thickness, the wall angle, friction coefficient and the load. Two forming methods are possible which determine the springback angle- one assumes the sheet to stretch before being bent and the other assumes the sheet to bend around a radius before being stretched. The latter case is more favourable to reduce the effect of springback on the final dimensions of the stamped part [20-22].

Assuming that it is due to elastic unloading, Mickalich and Wenner [20] modelled springback in the stamping of a long continuous channel as follows, where p in the subscript denotes the plastic state:

According to the Hill criterion of plastic yielding due to transverse anisotropy:

$$\tau_y = \frac{\sigma_y}{\sqrt{\left(1 + \nu^2 - \frac{2\nu r}{1+r}\right)}} \quad (2.9)$$

$$\epsilon_y = \tau_y / D \quad (2.10)$$

Here τ is the true stress and ϵ is the true strain, σ_y is the yield stress, r is the anisotropy coefficient and D is related to the Young's modulus E and Poisson's ratio ν as:

$$D = \frac{E}{1 - \nu^2} \quad (2.11)$$

This leads to the elastic unloading from the attained plastic state according to:

$$\frac{\tau}{\tau_y} = \frac{\tau_p}{\tau_y} + \frac{(\epsilon - \epsilon_p)}{\epsilon_y} \quad (2.12)$$

Leading to the angle after springback upon being wrapped around an angle ϕ around a radius R being:

$$\phi_s = \frac{R\phi}{R_s} e^{\Delta\epsilon_B} \quad (2.13)$$

R_s is the radius of the concave face after springback, ϵ_B is the strain on the concave face and ϵ_{BS} is the strain on it after springback.

2.2.4 Tribology of the stamping process

Friction between the deforming sheet-metal and die in the punch-stretching process causes strain localisation. The deformation of that part of the sheet which is in contact with the punch is countered by the frictional force of the contact, while the part of the sheet not in contact deforms freely [14]. This strain localisation causes flow instability and reduces the

total forming limits of the sheet by necking or tearing [23,24]. Forming limits are not an intrinsic material property, but are dependent on friction with the forming die [14], the geometry of the process especially the radius of the punch [25,26] and strain path [18].

Stamping formability is limited by die friction, especially in micro-scales where the frictional force is significant to the deforming forces. Friction between the deforming sheet-metal and die in punch stretching causes strain localisation during stamping, thereby reducing the forming limits [27]. The effect of friction on the distribution of strain upon punch stretching is shown in the plot in Figure 2. 7. The deformation of that part of the sheet which is in contact with the punch is countered by the frictional force of the contact, while the part of the sheet not in contact deforms freely [14]. This strain localisation causes flow instability and reduces the biaxial forming limit of the sheet by necking or tearing [23,24]. Forming limits are not an intrinsic material property, but are dependent on friction with the forming die [14], geometry of the process especially the radius of the punch [25,26] and strain path. If the coefficient of friction due to contact with the punch is disregarded, the center of the sheet experiences the greatest strain and fails. But the friction between the punch and the sheet is always finite, due to which, the location of failure in stamping is always offset from the pole [13].

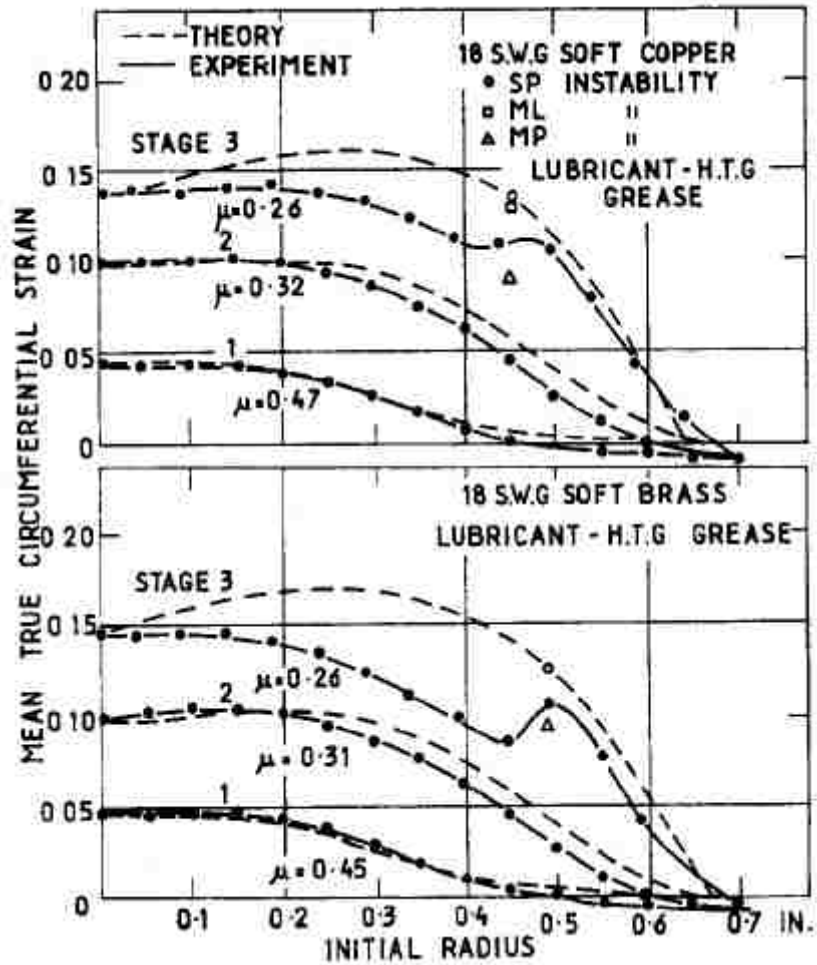


Figure 2. 7: Distribution of circumferential strain in punch stretching of annealed copper and brass, from finite element simulation [27]. The forming limit shows a 50 % increase with a 0.2 decrease in the coefficient of friction.

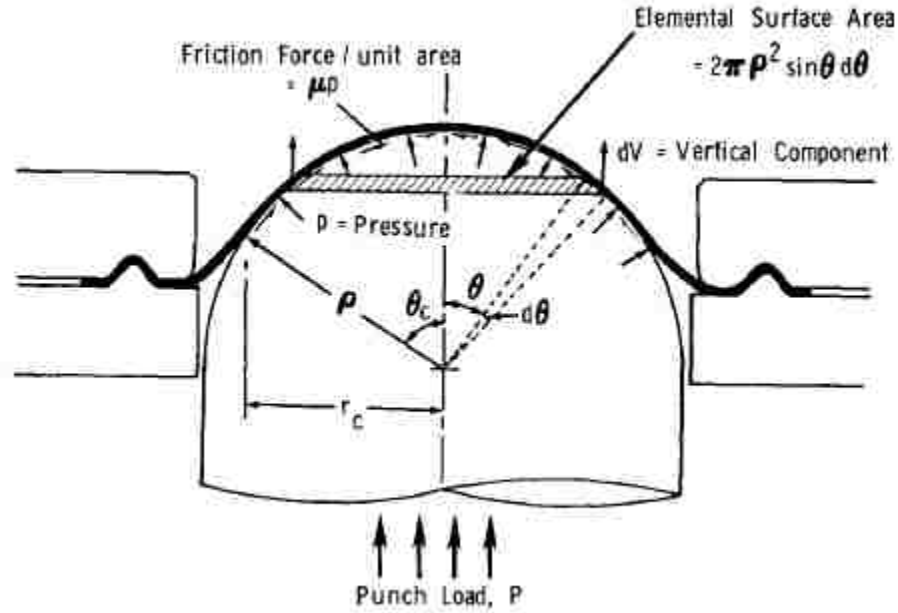


Figure 2. 8: The model of punch stretching used to determine the coefficient of friction between the sheet and the die during forming [14].

An analysis of the friction in punch stretching is as follows [14]. From the model in Figure 2. 8, the vertical component of the force acting on a ring of the sheet concentric with the pole of the punch is:

$$dV = (p \cos\theta + \mu p \sin\theta)(2\pi\rho^2 \sin\theta d\theta) \quad (2.14)$$

the integration and rearrangement of which gives:

$$\mu = \frac{2 - Xr_o}{X\left\{\left(\frac{\rho^2}{r_o}\right) \sin^{-1}\left(\frac{r_o}{\rho}\right) - \sqrt{(\rho^2 - r_o^2)}\right\} - (2r_o/(\rho^2 - r_o^2))} \quad (2.15)$$

Here, the symbols used are: p is the pressure at the interface, θ is the angle between the punch axis and the normal to the sheet, ρ is the radius of the punch, r_o is the point of

inflection in the load-displacement plot and X is the slope of the plot of the punch radius and the punch-sheet interface boundary.

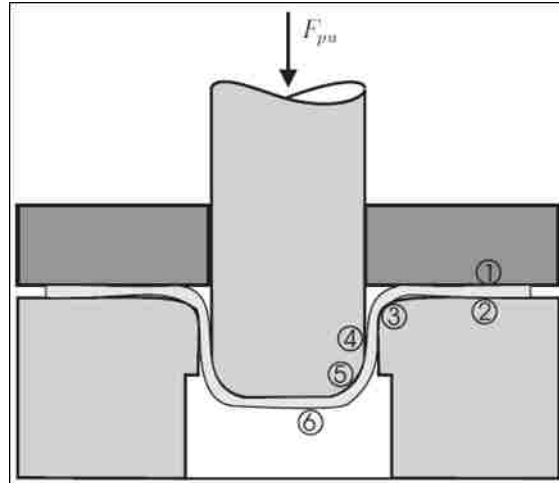


Figure 2. 9: Tribological model of the deep-drawing process which explains the nature of contact along different regions of the sheet due to the geometry of the process. Regions 1 and 2 are clamped under the blank-holder and do not experience deformation due to the frictional force holding the sheet in place.

Schey demarcated 6 zones in a sheet undergoing deep drawing depending on the distinct deformation and lubrication conditions that prevail there [28], which are applicable to channel drawing as well. The model is shown in Figure 2. 9. In the regions 1 and 2, the sheet is firmly clamped under the blank-holder and the frictional force holds the material here from being drawn in. No deformation occurs here. In regions 3 and 5, the sheet undergoes bending and restraightening. On the inside of the radius, there are high circumferential stresses on the sheet. Any lubricant film is almost always broken and high friction limits the transmission of stresses. Region 4 undergoes the most favourable mode of deformation akin to uniaxial deformation. Due to the geometry of the process, there is no contact between the

sheet and the die and high pressure of the trapped lubricant film produces a good surface finish on the stamped part. Region 6 experiences biaxial tension as in the case of punch stretching. Although this model describes a cylindrical-punch deep drawing process where the strain states are different from a case of plane-strain draw forming for stamping channels, the tribology and the contact nature between the sheet and the die are comparable.

The use of lubricants in channel stamping creates a more favourable distribution of strain and reduces the localised thinning effects. The prevention of metal-metal contact is critical since surface damage due to tool contact becomes significant as the scale of the process is reduced.

2.3 Ferritic Stainless Steels

Ferritic stainless steels are a class of stainless steels containing high chromium contents and little or no nickel or nickel-equivalent constituents. This makes them single-phase ferritic as can be seen in the Schaeffler diagram

Figure 2. 10 [29]. The behaviour of this class of steel is less like the austenitic stainless steels and more like plain low-carbon steels in their mechanical properties. Some of these properties include static strain ageing and dynamic strain ageing during tensile deformation, and a low strain-hardening exponent. Ferritic stainless steels show a remarkable increase in strength when aged at intermediate temperatures (475 °C) and higher temperatures (750 °C) due to the precipitation of intermetallics, carbides, nitrides and α' -ferrite. This undue strength, often more than the full-anneal strength by a factor of three is accompanied by a drastic reduction in ductility.

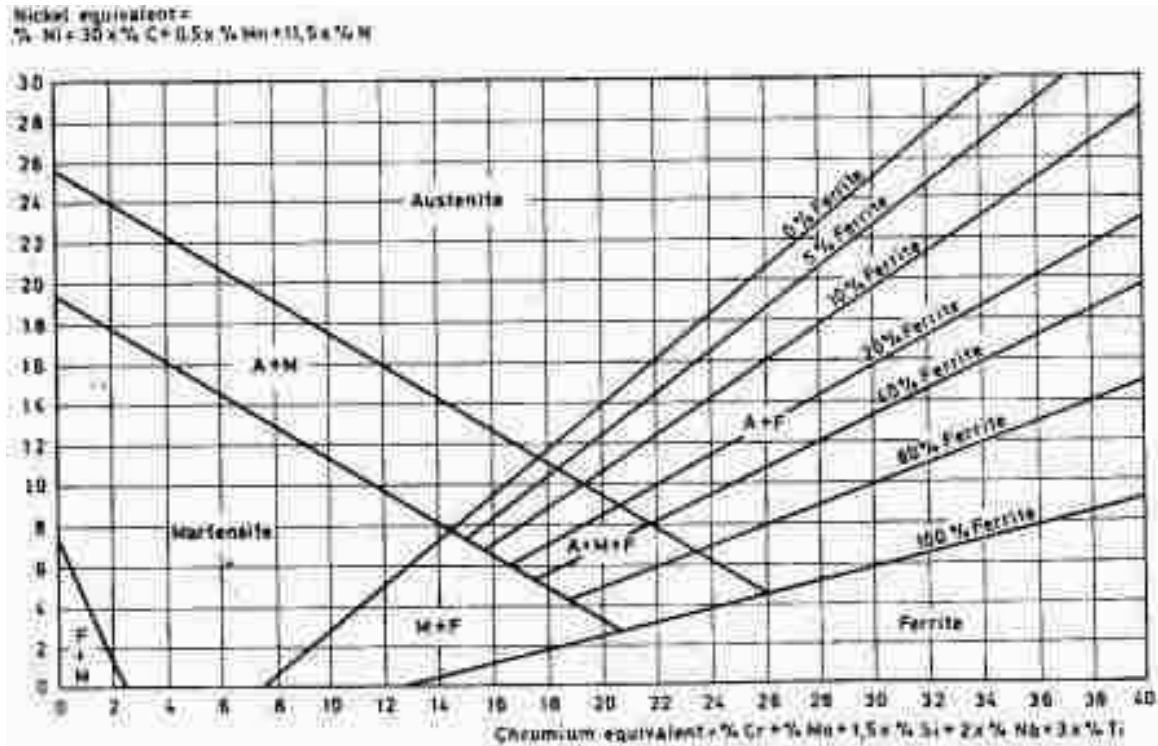


Figure 2. 10: The Schaeffler diagram which aids in determining the phase composition of stainless steels. At 30% Cr, the stainless steel is fully ferritic [29].

The iron-chromium binary alloy phase diagram in Figure 2. 11 shows an α -ferrite phase for the high chromium regions (>15 %) at all temperatures below liquidus [30]. The Fe-Cr binary phase diagram has a γ -Fe austenite region in the low-chromium high-temperature region. This region grows in size with increasing contents of interstitials such as carbon and nitrogen which are austenite-stabilising alloying elements. The Fe-Cr system is susceptible to embrittlement caused by spinodal decomposition at 475 °C [31], but the ageing time for this is usually above 100 hours and the more immediate precipitation of carbides, nitrides and intermetallic phases at this temperature is of greater concern, which can be discerned from the precipitation diagram of Figure 2. 12.

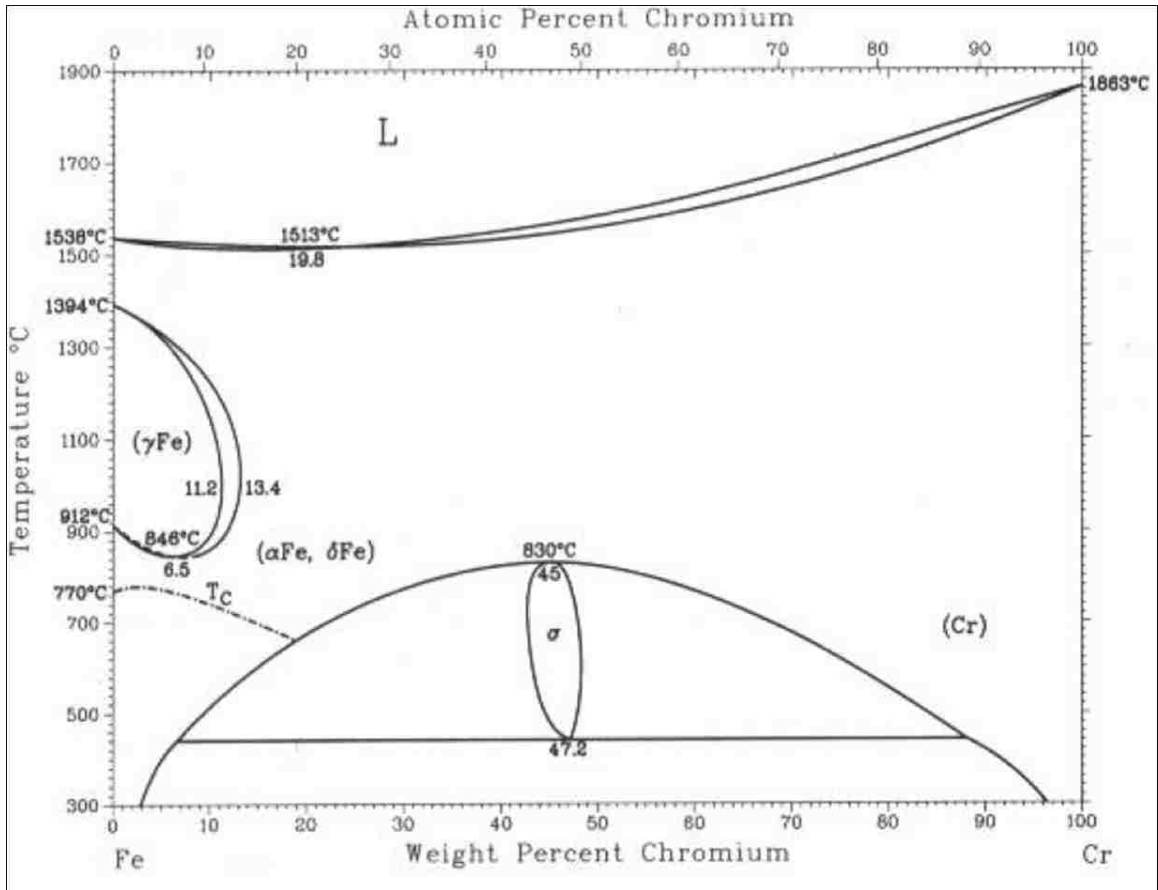


Figure 2. 11: The binary Iron-Chromium phase diagram [58].

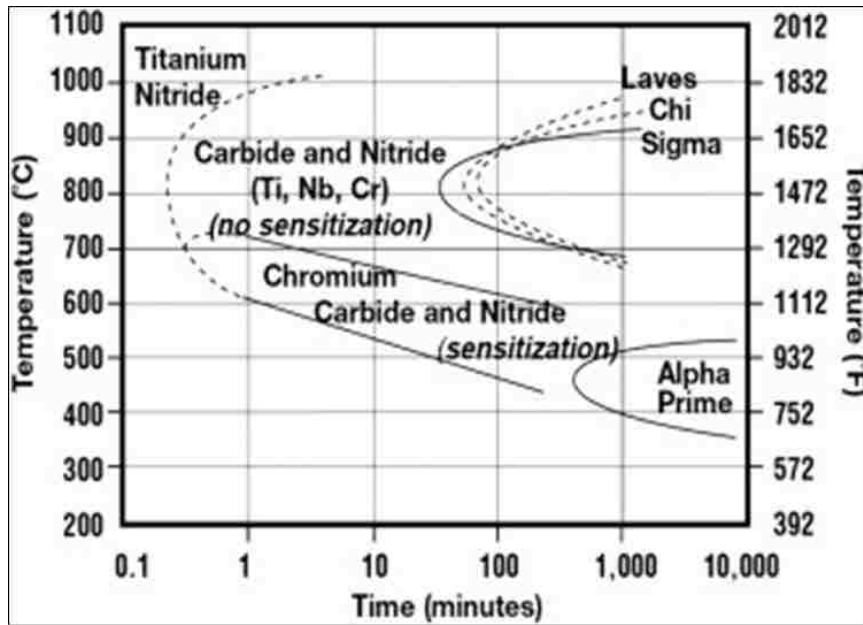


Figure 2. 12: The precipitation diagram for ferritic stainless steel AISI type 444 [59].

2.3.1 Material selection and alloy design

High chromium contents (greater than 25 %) in stainless steels improve the corrosion resistance even at high temperatures [32] and ensure a fully ferritic structure at all temperatures. Common alloying additions include rare earth metals as stabilisers, which preferentially form carbide and nitride precipitates over chromium, so as not to compromise the corrosion resistance. Chromium forms a passive layer over the surface in its oxide state and precipitation of it in carbides or nitrides would reduce its ability to do so. Titanium, vanadium, niobium and aluminium are common additions for this purpose in amounts of four to eight times the carbon content [33].

Interstitial alloying elements reduce the ductility of stainless steels, especially in deep drawing, due to dynamic strain ageing. But they also have advantageous effects such as the prevention of grain coarsening during recrystallisation annealing by the Zener pinning mechanism [34]. Nitrogen is especially effective in this and is usually added when a fine-grained microstructure is desired, such as for metallic foils and additions over 0.10 % by weight are effective [32]. When precipitated with the stabilisers in coarse intragranular distribution, they have little effect on the deformation behaviour and these precipitates are also effective in inhibiting grain growth.

Nickel is an austenite stabiliser and is added to increase the stacking-fault energy of the stainless steel for the improved cold-working properties [35]. It is both increasingly uneconomical and undesirable for a fully-ferritic microstructure, and the alloy under consideration is free of nickel additions.

Fine-grained microstructures are preferred for metallic foils which are to be cold-worked due to the size-effects that reduce the toughness and strain hardenability in reduced

scales. Ferritic stainless steels require cold-work and recrystallisation annealing to reduce the grain size [33]. Grain refinement is carried out by performing recrystallisation during rolling through high reductions per pass and low finishing temperatures [36]. In order to prevent excessive grain growth and embrittlement, annealing is carried out between 760-930 °C and cooled rapidly. Any embrittling sigma-phase particles are dissolved in this temperature range at short holding times.

2.3.2 The deformation behaviour of ferritic stainless steels

The mechanical properties of ferritic stainless steels are less like those of the austenitic stainless steels and more like those of the low-carbon steels, due to their bcc structure and low rate of strain hardening. The uniform elongation is in the range of 13-15 % in uniaxial tension, from the experiments of Wolff and Ball in Figure 2. 13 [37] and wavy slip occurs due to the lack of a distinct slip system in the body-centered cubic system (Figure 2. 14) [38]. They experience dynamic strain ageing due to interstitial-dislocation interaction and form Lüders bands during deformation as a result [39]. Ferritic stainless steels exhibit a distinct yield point, and because of a low strain hardening exponent of 0.12, localisation of deformation within these bands cannot be prevented and they have a low uniform elongation in tensile deformation [33].

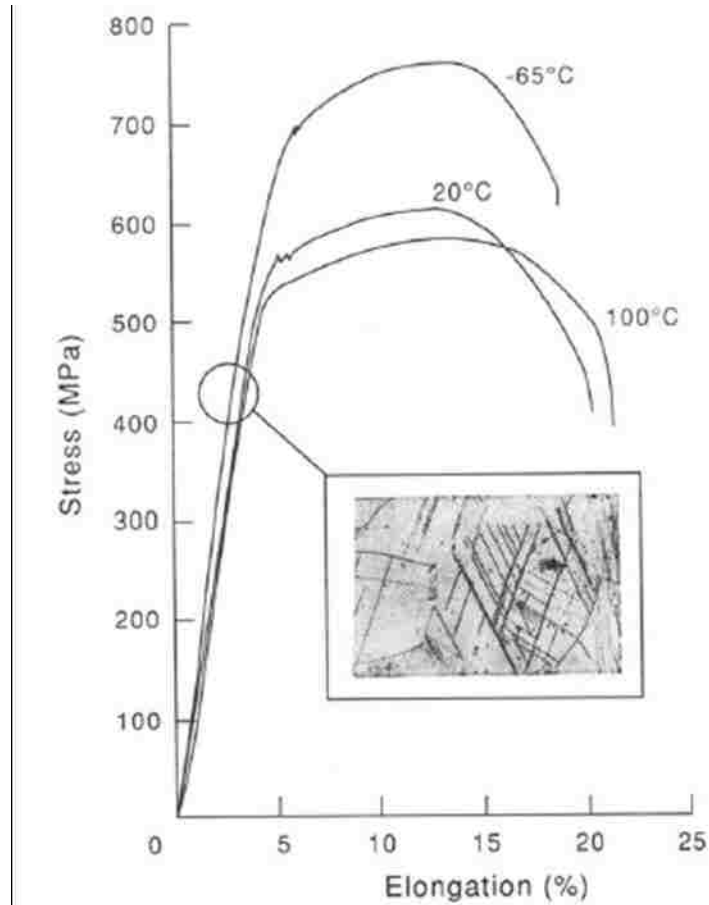


Figure 2. 13: The tensile deformation behaviour of a 40 % Cr ferritic stainless steel showing serrated flow and low uniform elongation [37].

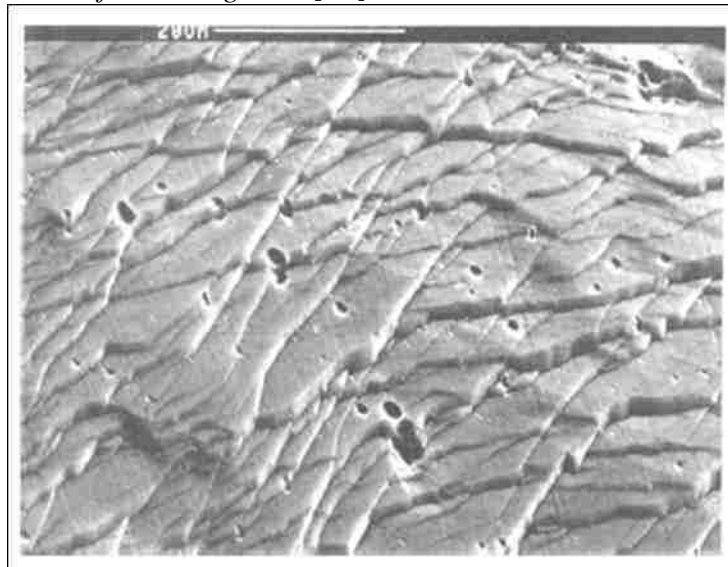


Figure 2. 14: Ferritic stainless steels deform by wavy slip due to the absence of a distinct slip system in the bcc crystal structure. Surfaces of deformed tensile specimens show wavy slip bands because mobile dislocations change slip systems often during plastic deformation [38].

2.3.3 The yielding phenomenon and strain ageing

Body-centered cubic metals with interstitial elements exceeding 0.001 % (weight percent) exhibit the yielding phenomenon, in which the yield point occurs at an elevated stress to subsequent flow stresses, sometimes greater by a factor of two [40]. The deformation of a material occurs in four distinct stages. In the initial stage upon application of load, say in uniaxial tension, the material undergoes elastic deformation and the flow curve shows an almost linear variation of load with extension. Some materials make a gradual transition from elastic to plastic deformation, but most engineering materials show a distinct peak and drop in the load upon entering the plastic state [41]. This is the yield point phenomenon and is caused by the strain ageing mechanism [40]. The subsequent elongation of the material occurs at an almost steady load that may fluctuate. These fluctuations may be further explained by dynamic strain aging and the formation and propagation of Lüders bands [42]. Another cause for the serrations in the flow curve is deformation twinning. The high stresses required for twinning to occur and the short time intervals over which twinning takes place causes the rise and fall in the flow stress. Serrated flow was first reported by Portevin and Le Chatelier in 1923 and is therefore known as the Portevin-Le Chatelier effect or PLC [43].

Strain ageing is a strengthening mechanism by which dislocations are pinned down and rendered immobile by interstitial solute atoms. The strength of the material is increased but the ductility is decreased due to a time-dependent exposure to warm temperatures after cold-working. Solute atoms preferentially settle at the line of dislocations due to the increased lattice spacing produced by the extra half-plane of atoms in an edge dislocation. This pinning down is due to the interaction forces of particles and dislocations and the force

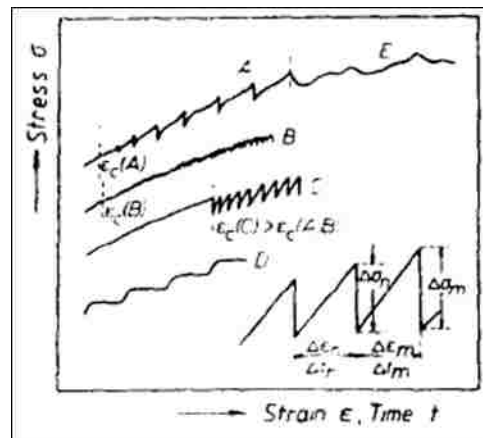
required to separate a dislocation from a particle is higher than the force required to keep a dislocation in motion during deformation [44]. The movement of interstitial solute atoms towards a dislocation is a diffusion-controlled process and is dependent on time and temperature. Age-hardening is therefore performed at moderate temperatures (so as not to cause recovery or recrystallisation at higher temperatures) and for long periods of time. Strain ageing explains the distinct yield point in the straining of a material in the form of a sharp kink, and also the drop in flow stress after this yield point. The reappearance of a yield point when a material is loaded past its yield point, unloaded, aged and then reloaded is also explained by the phenomenon of strain ageing.

Carbon and nitrogen are small-size interstitial solutes commonly found in steels and their ageing effect is considered the same due to the similar behaviour with moving dislocations. Henceforth, solute atoms refer to both carbon and nitrogen interstitials. Interstitials affect the mechanical properties of steels in three ways as listed by Nabarro in 1948 [45]. They cause the precipitation of iron and chromium carbides and nitrides in the process of quench ageing. Carbon and nitrogen interstitials arrange themselves along the line of edge dislocations in an equilibrium position that relieves the hydrostatic stresses around the dislocations. This is the ensuing explanation for strain ageing. The third mechanism is that by which interstitials order themselves in the interstitial lattice sites at dislocations, which is the theoretical explanation of the delayed yielding phenomenon.

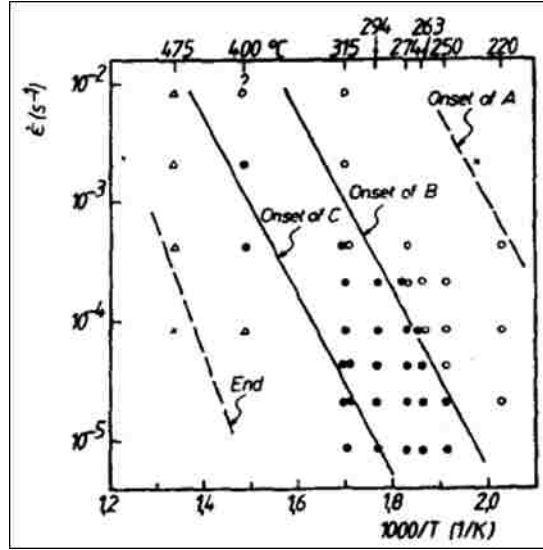
Edge dislocations possess a hydrostatic component of stress due to the extra half-plane of atoms, and there is a dilated and compressed region above and below it. These stresses can be partly relieved by the formation of an equilibrium atmosphere by solute

atoms. An elastic continuum theory is used to describe the force and energy fields of interaction, but this fails at the core of the dislocation.

Experiments on the static strain ageing and the activation energy for the ageing were reported by Gullberg and Plumtree in 1973 [46]. They found the activation energy for the ageing process to be 25.2 kcal/mol, which is comparable to that for the diffusion of nitrogen in chromium (24.3 kcal/mol). Since ferritic stainless steels contain more iron than chromium, which ranges from 13 to 30 % by weight, it would be more likely that the activation energy be dependent on iron. But this observation is attributed to the stronger nitride-forming tendency of chromium, which even in moderate ferritic stainless steels, averages to one chromium atom in every unit cell while the electronic interaction between nitrogen and chromium is more than four atomic distances.



(a)



(b)

Figure 2. 15: (a) the different types of serrations that can occur during tensile deformation and (b) the temperature and strain-rate dependence of the different types of serrations in a ferritic stainless steel [49].

Ferritic stainless steel shows a variation in the types of serration in the flow curve with temperature and strain rate and is shown in Figure 2. 15. Relatively low temperatures are sufficient for static strain ageing such as in the range of 100 °C and 150 °C. Experimental methods of Gullberg and Plumtree [46] involve straining test samples, ageing and then restraining. The lower yield point upon restraining and the flow stress during prestraining are used in quantifying the effect of static strain ageing as per Hartley's [47] modification of the Cottrell-Bilby [48] analysis of the effect of ageing as follows:

A strain ageing parameter is defined as:

$$\frac{\Delta\sigma}{\bar{\sigma}} = 2 \frac{(\sigma_a - \sigma_p)}{(\sigma_a + \sigma_p)} \quad (2.16)$$

where the subscript a and p denote aged and pre-aged.

The rate of increase in the yield stress due to ageing is directly related to the diffusion of interstitials to the dislocations as:

$$\frac{\Delta\sigma}{\bar{\sigma}} = K + St^{2/3} \quad (2.17)$$

Here, K is a constant, S is a material constant proportional to $D^{2/3}$, where D is the diffusivity of the rate-controlling interstitial (N or C) and t is the ageing time. It was found that ferritic stainless steels containing 25 % Cr showed a greater $\Delta\sigma = (\sigma_a - \sigma_p)$ when the interstitial content was higher, but concurrently so where the values of $\bar{\sigma} = 1/2(\sigma_a + \sigma_p)$ which calls for the need to define the strain ageing parameter as above. The results of the experiment performed with 25 % Cr ferritic stainless steel with different interstitial contents aged at different temperatures and time periods were plotted by [46] as shown in Figure 2. 16. The slope of these lines is used to find the activation energy for the ageing process as:

$$\log(ST_a^{2/3}) = \log K_1 + \frac{2}{3} \log D_0 - \frac{2}{3} \left(\frac{Q}{2.3RT_a} \right) \quad (2.18)$$

Here K_1 is a constant, D_0 is the temperature-dependent part of the diffusion coefficient, Q is the activation energy and R is the universal gas constant.

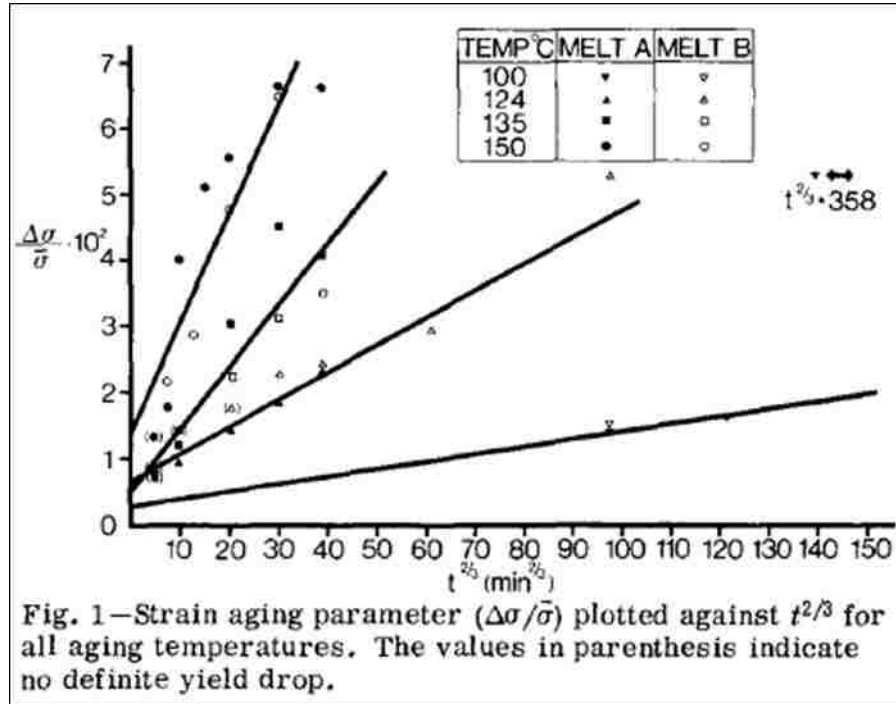


Figure 2. 16: Strain ageing quantified by the strain ageing parameter for a ferritic stainless steel [60].

Dynamic strain ageing is a phenomenon observed during the deformation of a material that takes place by the same mechanism as strain ageing. Dynamic strain ageing manifests as serrations in the flow curve of a deforming material when there are multiple kinks of rising and falling flow stress after the material has yielded. Each rise corresponds to the solute atoms pinning down the mobile dislocations and each subsequent drop in the flow curve indicates that the dislocations have broken free of the solute atoms and are moving due to the applied stress. This type of serrated flow was first reported in ferritic stainless steels by Pink and Grinberg [49].

2.3.4 The dislocation theory of yielding

The existence of the yield point and the yield stress required to cause plastic deformation was first explained in terms of the interaction of dislocations and solute atoms

by Cottrell and Bilby in 1949 [48]. The yield point phenomenon represents the larger stress required to break the mobile dislocations free of the solute atoms that pin them down than the stress required to keep the dislocations in motion, or the flow stress. At favourably high temperatures, diffusion allows solute atoms to catch up with the moving dislocations and realign themselves, thus causing repeated rise and fall in the flow curve serrated flow due to dynamic strain ageing, called so because this mechanism occurs during deformation and in the same manner as thermal ageing.

An edge dislocation creates a region of compressive stresses above it and tensile stresses below it. A screw dislocation does not possess these hydrostatic components due to the absence of an extra half-plane of atoms. Interstitial solute atoms can relieve the hydrostatic stresses of a dislocation by locating themselves along the dislocation line. The energy of interaction between a solute atom and an edge dislocation U creates an 'atmosphere' in equilibrium:

$$U = 4Gb \epsilon r^3 \frac{(\sin\theta)}{R} \quad (2.19)$$

Where U is the interaction energy of a solute atom at (R, θ) from a positive edge dislocation, r is the radius of the solute atom, G is the shear modulus and ϵ is the strain caused by increasing the atomic radius to r' as $\epsilon = (r'-r)/r$.

The elastic nature of the dislocation upon which this model is based, fails at the core of the dislocation at small values of R . The material constants are combined into one term, A and the above equation is simplified as:

$$U = A \frac{(\sin\theta)}{R} \quad (2.20)$$

There are two categories of dislocations in a deforming material- slow moving and fast moving dislocations. The fast moving dislocations remain relatively unhindered by solute atoms due to the limited diffusivity of the solute atoms, but the slow dislocations are caught up by the solute atoms. The speed of the fast-moving dislocations is limited to the speed of sound in that material. Cottrell and Jaswon in 1949 [50] described the movement dislocations and solute atoms together at slow speeds. The drift velocity v with which a dislocation and solute atom move together under a force F due to their mutual interaction is:

$$v = \frac{D}{kT} F \quad (2.21)$$

$$v = \frac{D}{kT} \frac{A}{r^2} = \frac{Dl}{r^2} \quad (2.22)$$

Where the characteristic length l ($=A/kT$) is the radius of the atmosphere.

The critical speed of the dislocation V_c (assuming $r = l/2$):

$$v_c = \frac{4D}{l} \quad (2.23)$$

Below critical speed, the particle and dislocation remain together, but the particle always lagging behind. Above this speed, the dislocation can pull away from the atom which lags behind by distance l .

The critical stress σ_c is that which is required to move it at critical speed v_c .

$$\sigma = \frac{v}{v_c} \sigma_c \quad (2.24)$$

The estimated value of σ_c is found to be:

$$\sigma_c = \frac{28Ac_0N}{b} \quad (2.25)$$

Where c_0 is the atomic concentration of the solute and N is the number of total atoms per unit volume. 28 (Cottrell) is sometimes replaced with 17 (Jaswon).

The critical resolved shear stress to release line of dislocation from a solute atom is:

$$\sigma_o = \frac{3\sqrt{3}A}{4\lambda^2\rho^2} \quad (2.26)$$

..per unit length of dislocation, assuming that the tensile axis and the slip direction are oriented at an angle of $\pi/4$. Here, λ is the length of slip distance in the dislocation.

A reasonable approximation of the above equation is given by:

$$\sigma \approx \frac{A}{(b^2r_o^2)} \quad (2.27)$$

Here r_o is the distance of the solute atoms from the dislocation core.

The relationship between the rate of straining, dislocation velocity and the density is:

$$\dot{\epsilon} = b\rho\bar{v} \quad (2.28)$$

where $\dot{\epsilon}$ is the strain-rate, b is the Burger's vector, ρ is the dislocation density and \bar{v} is the mean dislocation velocity.

These phenomena, namely static strain ageing and the yield point, dynamic strain ageing, and the low strain hardening exponent limit the ductility of the high chromium ferritic stainless steels that can be applied in a cold working operation such as sheet metal stamping. They result in the formation of necking due to localised deformation leading to the early termination of the uniform elongation. The mathematic treatment of these physical phenomena that control the deformation behaviour of the ferritic stainless steels allows their better understanding in order to overcome these practically.

2.4 Lubrication by Lamellar Solids

Forming limits of sheet metals can be increased by elevated temperatures, but this causes problems such as high friction due to adhesion and reduced tool life due to material transfer to the die. High friction in punch stretching causes lowered limit strains due to strain localisation [15] [24]. Lubrication can reduce the friction between the sheet and the die thereby raising the forming limits and improving the strain distribution [14]. Prevention of metal-metal contact between the sheet and the die is important for surface quality of the part and tool life. Lamellar solids have good load-bearing capacities to perform under high stamping pressures and they maintain their lubricity even at elevated temperatures [51]. Boron nitride is one such solid lubricant and it can reduce the friction to as low as 0.15 [51]. Molybdenum disulphide (MoS_2) is most commonly used in metal forming because of its ability to drastically lower friction [52], while tungsten disulphide (WS_2) has greater thermal stability and oxidation resistance in comparison, by a 100 °C [53]. The ceiling lubrication temperatures for the solid lubricants are limited by their oxidation [54]. The disulphides of

tungsten and molybdenum have excellent lubricating properties, and were often confused with graphite for their similar appearance and physical properties.

Solids such as graphite, owe their lubricity to their lamellar structure in which the crystal lattice is arranged in planes that are weakly bonded and ‘easy-shear’ occurs along them. Boron nitride, tungsten disulphide and molybdenum disulphide fall under this category and they have a hexagonal structure. BN is different from the dichalcogenides in that the boron and nitrogen atoms lie in the same plane (Figure 2. 17), whereas in the structure of WS_2 and MoS_2 the tungsten (or molybdenum) and sulphur atoms occupy lie in alternating planes (Figure 2. 18). Unlike graphite, these solids do not depend on moisture or ambient humidity for their lubrication action [52]. They also have the added advantage of being ‘clean’ over graphite and can be removed from the surface after the process by simply rinsing in water. Reports of the lubricity of tungsten disulphide are recent and few, and WS_2 has the same crystal structure as MoS_2 .

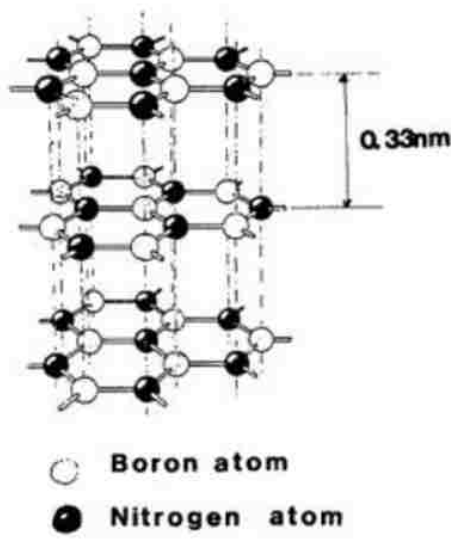
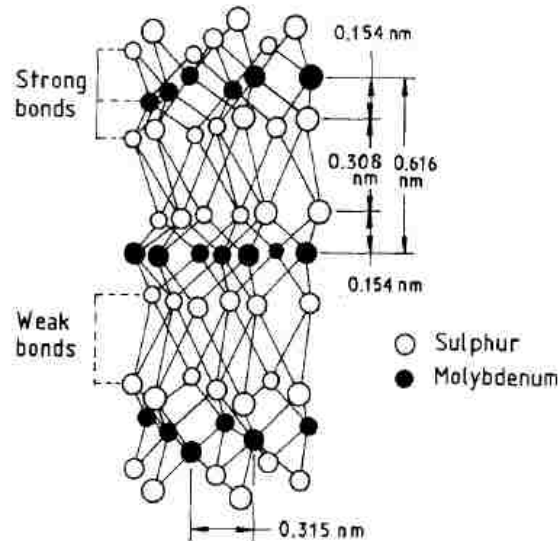
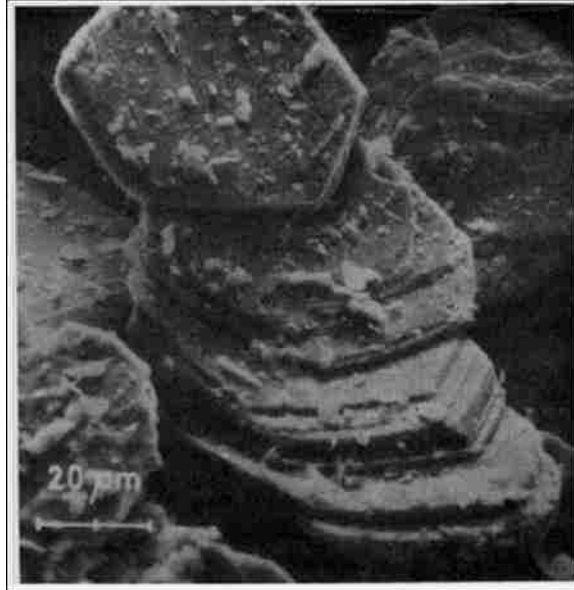


Figure 2. 17: The crystal structure of hexagonal Boron Nitride. The dotted lines represent weak van der Waals bonds permitting the ‘easy shear’ of the planes bonded thus [61].

The lamellar hexagonal structure makes the mechanical properties of these compounds anisotropic. Although they are of reduced strength along the shearing direction of the lamellar planes, normal to it they are hard [55]. Under sliding conditions after run-in, upon preferential orientation of the crystal lattice, they exhibit excellent low-friction and low-wear properties, but during run-in especially under high normal loads, they have a tendency to scratch and embed into the counterface if their orientation is not along the sliding direction. This behaviour depends on the relative hardness of the substrate, and may play an important role in stamping, where high loads and non-sliding contact occur.



(a..contd.)



(b)

Figure 2. 18: (a) The crystal structure of molybdenum disulphide [52], and (b) scanning electron microscope image of the lamellar arrangement and displacement of the hexagonal planes of molybdenum disulphide [62].

Boron nitride is a popular lubricant for its white colour, high temperature performance and economy. Being isoelectronic to carbon, it exists in three crystalline forms, namely hexagonal (h-BN), cubic (c-BN) and wurtzite (w-BN), of which c-BN is second in hardness only to diamond and h-BN is isostructural to graphite. In the lamellar hexagonal form, it reduces the coefficient of friction between sliding surfaces to as low as 0.29 [56]. Deacon and Goodwin tested graphite, MoS₂, BN and talc for their frictional properties while eliminating chemical effects (by using platinum substrates) [51] and reported a coefficient of friction lower than 0.2 for BN. No moisture is required for the lubricating action of BN unlike graphite, due to the absence of unbonded electrons in the structure. Transfer films formed by the lubricants contribute to their lubricity. Although they may be undesirable in the finished product, their formation on the mating surfaces is necessary in reducing the friction [55].

2.5 Summary of the Review of Literature

From the work that has been published so far, there is a wealth of information on the formability of austenitic stainless steel, its corrosion properties and the material behaviour specific to bipolar plates. But very little information is available about the sheet metal formability of ferritic stainless steels to complement their excellent corrosion properties suitable for bipolar plates

Ferritic stainless steels experience dynamic strain ageing during deformation and they have a low strain hardening exponent that limits their useful ductility. Moderately elevated temperatures (100 – 300 °C) are reported to be useful in overcoming these problems for cold working operations. Sheet metal forming operations are limited more by high die friction than by the ductility of the material and solid lubricants have the advantage of easy application and cleaning after the stamping operation while reducing friction between surfaces effectively.

Thus, temperature and solid lubrication in combination have been used in this work to overcome the limiting factors of stamping ferritic stainless steel bipolar plates for PEMFC.

CHAPTER 3: Materials and Experimental Methods

3.1 Introduction

In this chapter, the materials and experimental methods used in this study are described. The materials used in this study are described in section 3.2. The experimental methods include the design and fabrication of the stamping equipment, detailed in section 3.3. The characterisation methods used to evaluate the stamping quality are detailed in section 3.4.

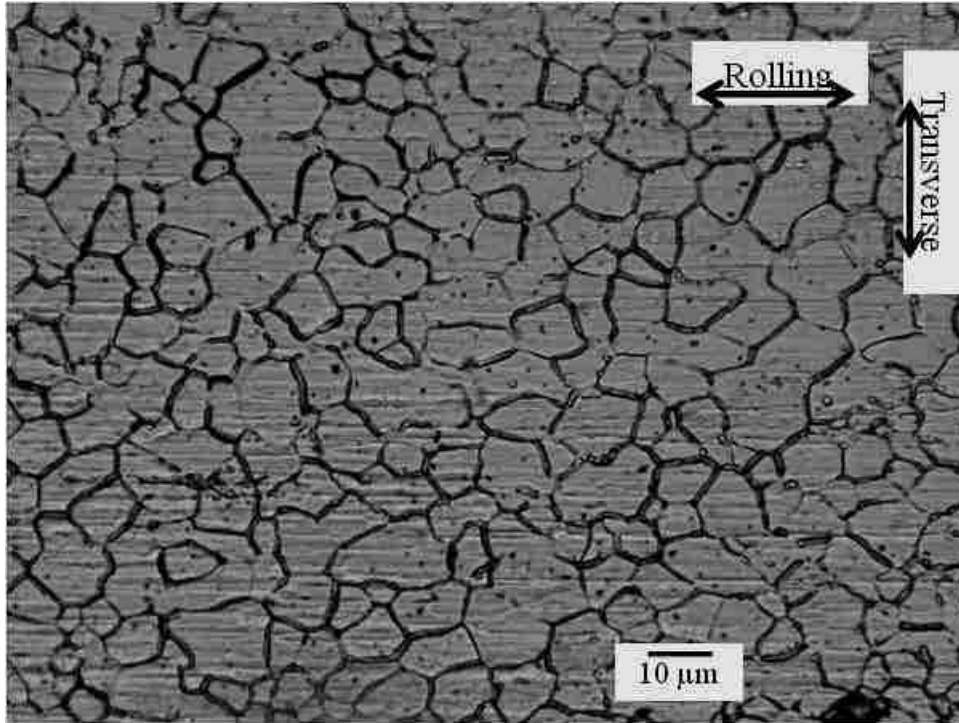
3.2 Materials and Microstructures

3.2.1 Microstructure and properties of the 30 % Cr ferritic stainless steel

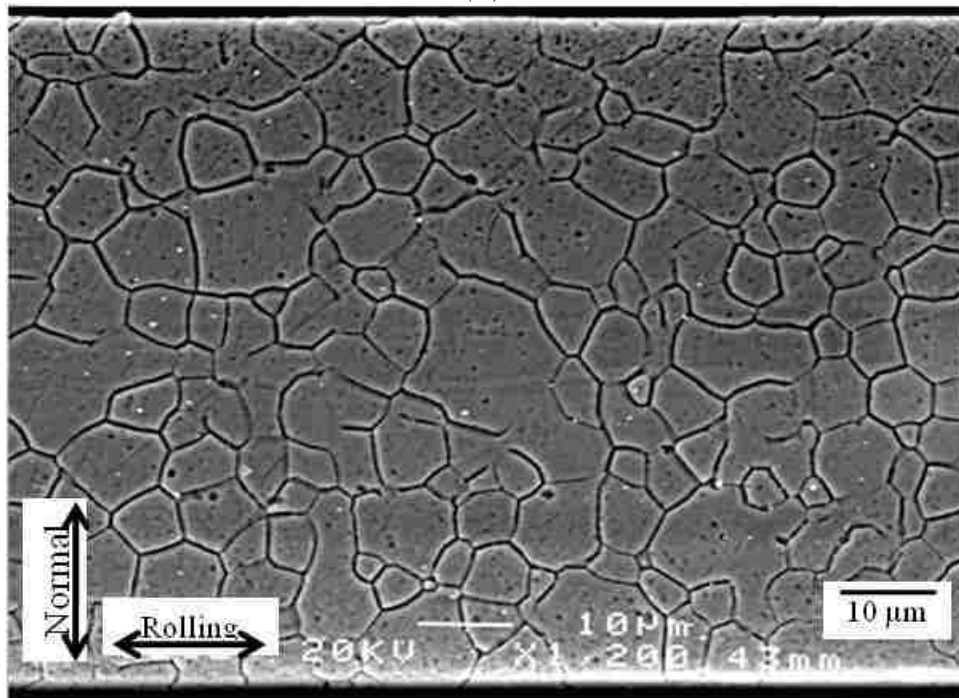
The ferritic stainless steel was used in the form of cold-rolled and annealed sheets of 75 μm thickness. The alloy was a high-chromium, nickel-free ferritic stainless steel containing 30 % wt. Cr, 0.025 % C and 0.035 % N, the complete composition of which is given in table 3.1 (from ICP analysis).

Table 3.1: Composition of the ferritic stainless steel used in this work:

Elements	Cr	C	N	Ti	Al	V	Ni	Fe
Weight %	30.0	0.025	0.035	0.034	0.045	0.36	-	balance



(a)



(b)

Figure 3. 1: (a) The microstructure of the sheet parallel to the surface (optical microscopy) and (b) microstructure of the cross-section of the sheet showing the equiaxed grains of the annealed condition (SEM).

The cross-sectional microstructure along the rolling and transverse directions are shown in Figure 3.1. The annealed microstructure consisted of equiaxed ferrite grains of $5.64 \pm 2.78 \mu\text{m}$, with coarse precipitates of titanium, vanadium and aluminium. Fine intercrystalline carbide precipitates of titanium were present in the microstructure. The coarse precipitates of Ti, V, Al and N present in the microstructure were distributed along the rolling direction. They were characterised using SEM and EDS and the results are presented in Figure 3. 2.

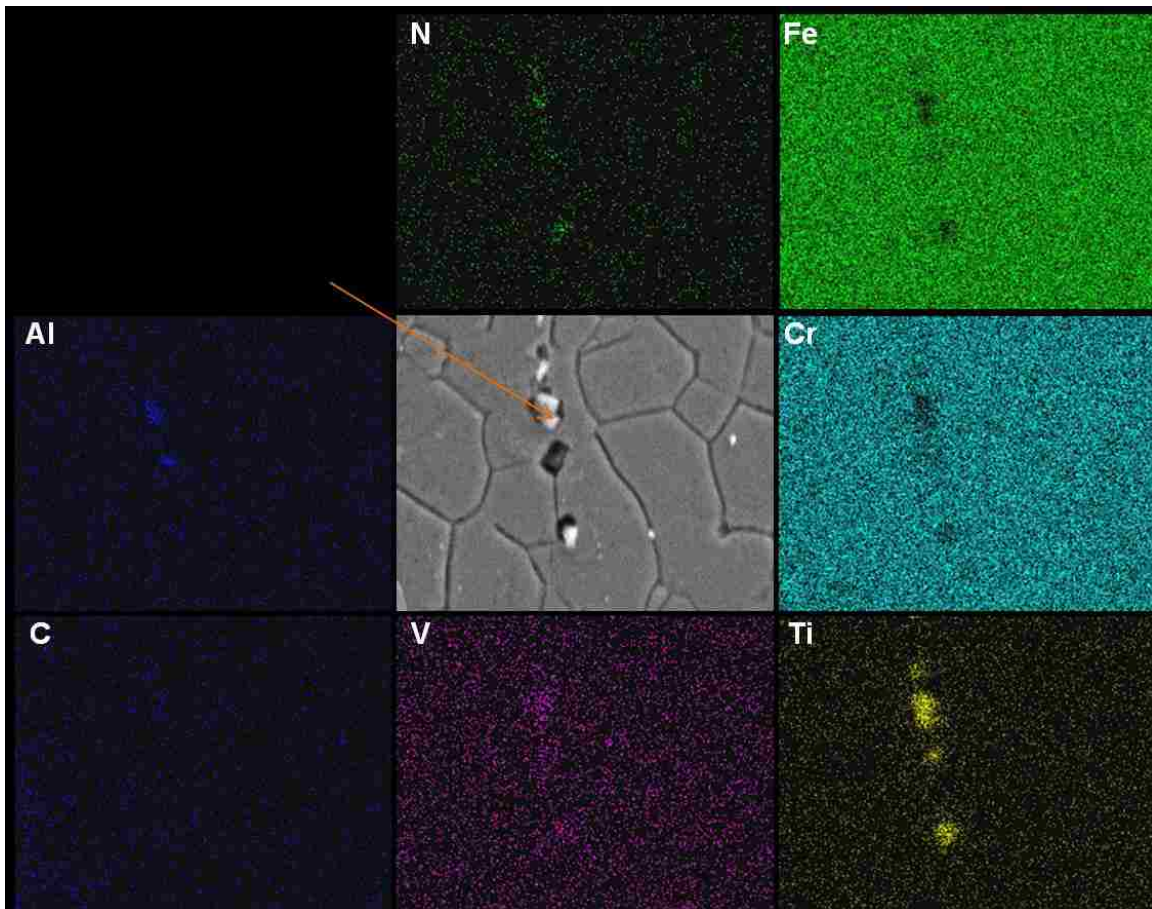


Figure 3. 2: (a) SEM micrograph of the coarse precipitates aligned along the rolling direction in the cross-section of the ferritic stainless steel and (b) EDS mapping of the area in (a) identifying the elements present in the precipitates as Ti, Al, V and N.

3.3 Description of the Stamping Experiments

3.3.1 Fabrication and operation of the stamping machine

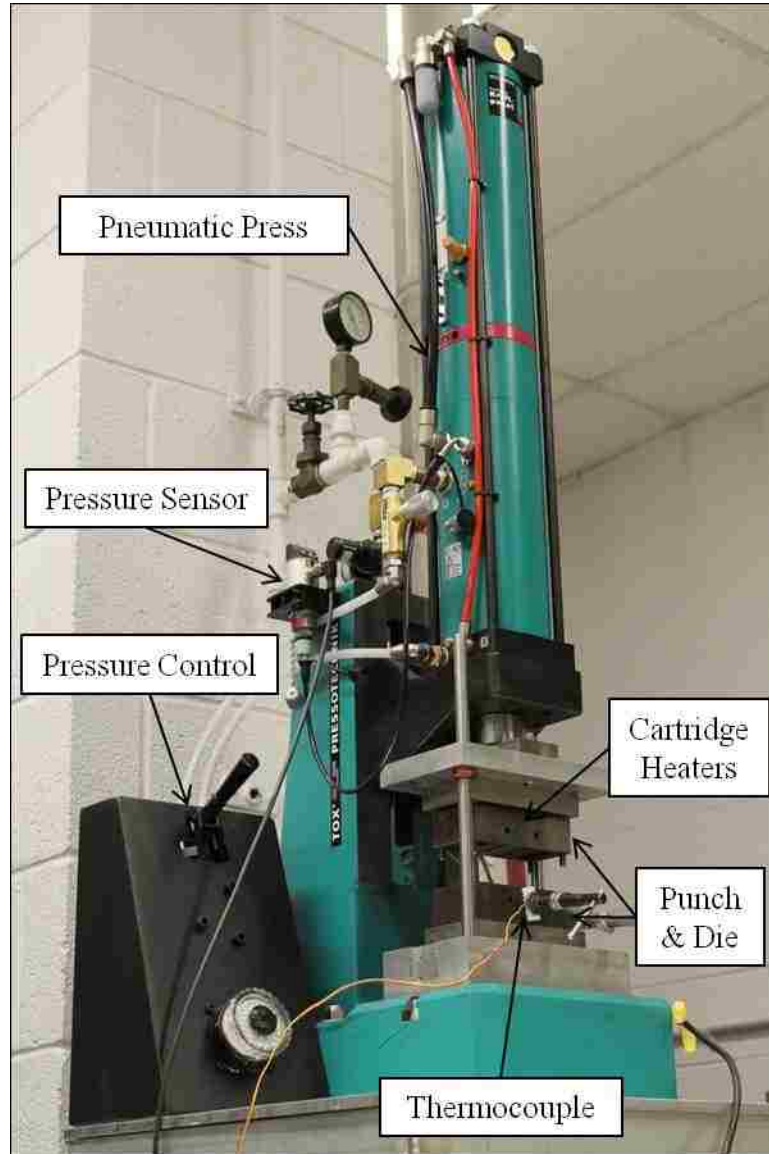
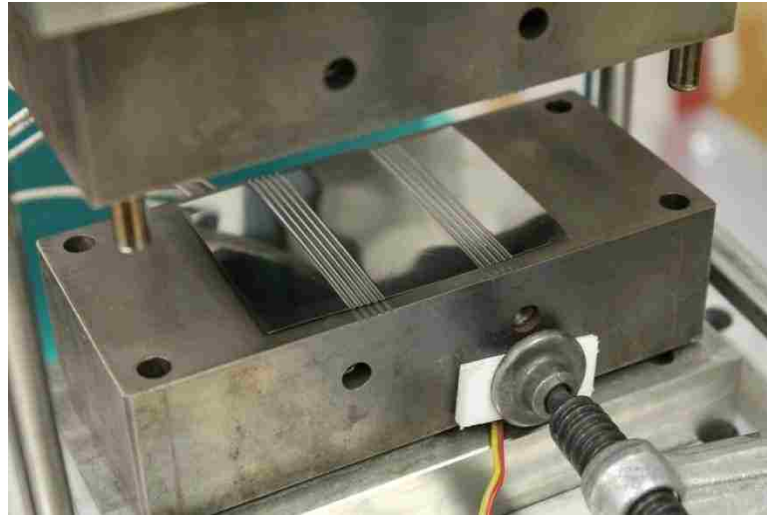


Figure 3. 3: The experimental stamping machine used in this work showing the punch and die assembly, with the cartridge heaters and thermocouple used to maintain the test temperatures.

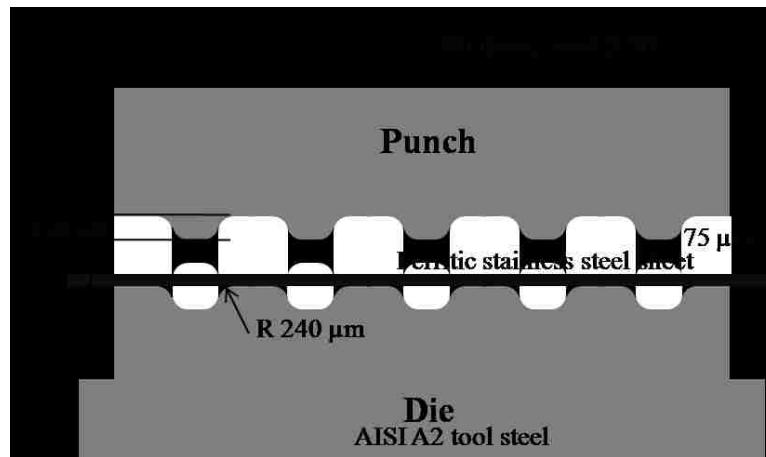
An experimental stamping machine was constructed for forming metallic bipolar plates and is shown in Figure 3. 3 along with the die set that was used. The stamping machine was constructed using a pneumo-hydraulic press (TOX – Pressotechnik S8.100.12.D, 10 – 100 kN load range) with an electronic pressure sensor for control (ZDO-01-40 AK). A pressure control valve controlled the pressure entering the press cylinder from the supply and the pressure sensor connected to a data acquisition system measures and recorded the cylinder pressure. The stamping machine was fixed onto a cross-frame table, with a locating plate on the base on which the lower die half was mounted. The upper die half, or the punch was attached to the piston head of the press. Platens were attached to the base of the frame and to the piston head of the pneumatic cylinder, fabricated out of AISI 4140 steel with titanium (6V-4Al) die holders to provide insulation between the heated die and the press. Two load cells measured the force experienced by the punch-head and the sheet-holding part of the die, known as the die shoulder.

For the forming of bipolar plate channels in stainless steel sheets, the die-set was fabricated out of AISI A2 grade tool steel and had two cartridge heaters inserted in the punch and die each. AISI A2 grade tool steel was selected for this process due to its high toughness and wear resistance required for stamping stainless steels. The die was heat-treated and tempered to 57 HRC. Temperature was maintained within a ± 3 °C range by means of a thermocouple inserted into the die and connected to a temperature controller (OMEGA Monogram MCS 77333). The micro-scale bipolar plate channels were machined into the punch and the die by wire-EDM. The dimensions of the channels are shown in Figure 3. 4. These dimensions are the industrial target and were therefore considered. The radius was set at greater than three times the thickness of the sheet to prevent the shear failure of the sheet at

the die radius during drawing [63]. The cross-sectional area and perimeter of the channel were selected for optimising the performance of the fuel cell in terms of specific power output of the cell.



(a)



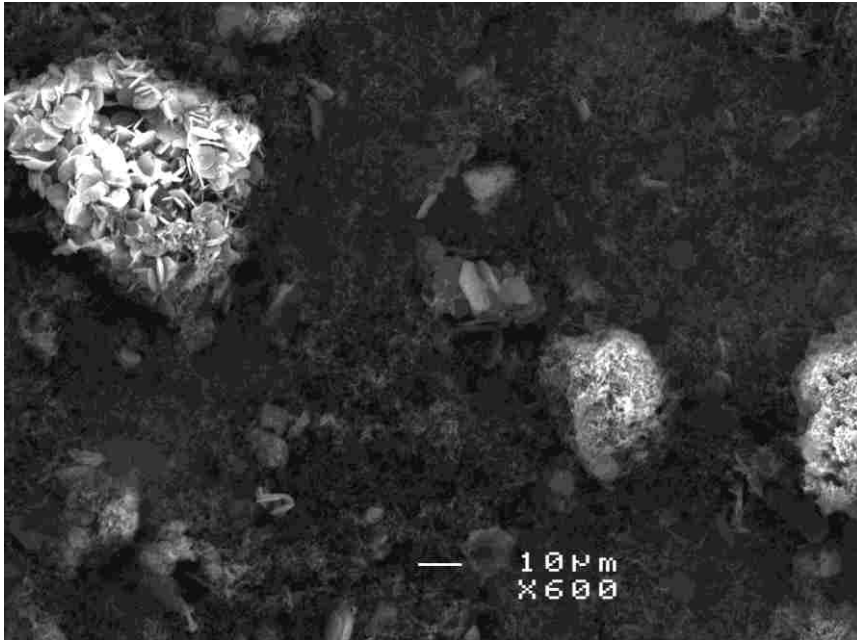
(b)

Figure 3. 4: (a) A closer view of the die set that was used the stamping the bipolar plate micro-channels along with a stamped foil. (b) Cross-sectional dimensions of the bipolar plate channels that were evaluated in this work.

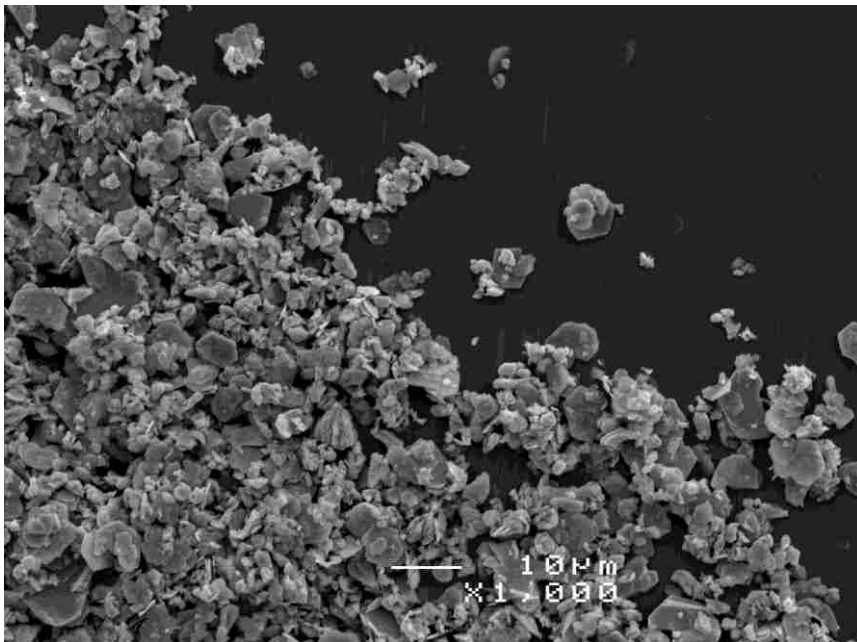
3.3.2 Procedure of the stamping experiments

Stamping of the micro-channels was performed at loads varied between 36 and 56 kN using the pneumatic control. Stamping was carried out at 25, 100 and 200 °C. The die was cleaned with acetone before each specimen was stamped. Stamping was performed placing the sheet with the rolling direction aligned with the tensile axis of the plane-strain channel drawing. The sheets were cut 5 mm wide by wire-EDM and cleaned with acetone before stamping.

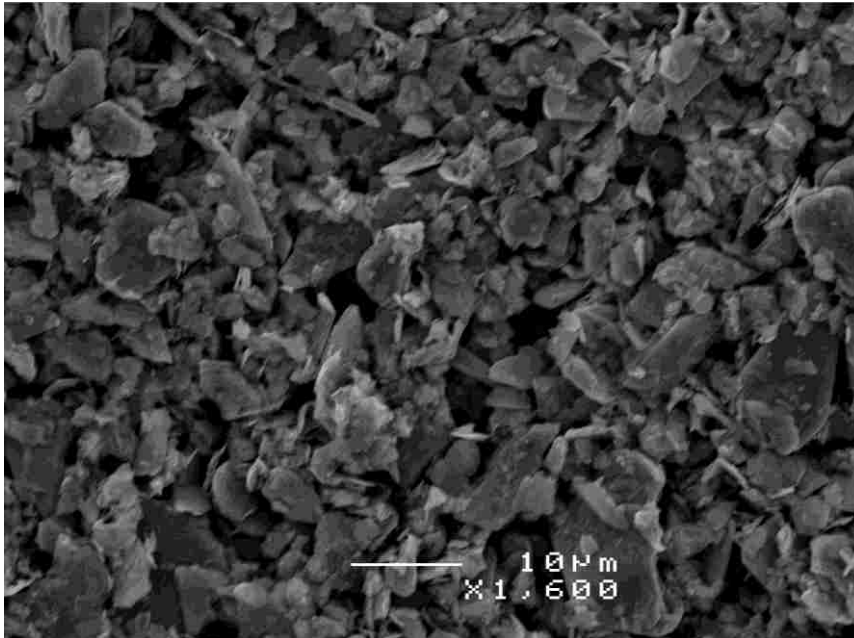
Stamping was carried out without lubrication and with the application of solid lubricants as a dry film on both sides of the sheet. BN, MoS₂ and WS₂ of particle size less than 2 μm were used (supplied by Sigma-Aldrich Co.). Ethanol was used as the carrier; a saturated suspension of the powders in ethanol were applied on the sheets using a swab and ensured dry before stamping so as to eliminate the effects of the carrier. The average lubricant film thickness was measured and found to be 20 μm before stamping. The difference in the distribution of the lubricant particles over the stainless steel surface upon application and before stamping is shown in Figure 3. 5.



(a)



(b) (...contd)



(c)

Figure 3. 5: SEM image of the distribution of lubricant particles over the ferritic stainless steel sheet surface applied using the technique described, (a) boron nitride, (b) tungsten disulphide and (c) molybdenum disulphide.

The various conditions under which stamping was carried out is shown in the test matrix in Table 3.2 that was used to organise the experiments.

Table 3.2: The conditions under which stamping was carried out:

Conditions of Stamping		
Temperature	Stamping Load	Lubrication
25 °C	36.95 kN	Unlubricated
100 °C	38.70 kN	BN
200 °C	40.45 kN	WS2
	42.20 kN	MoS2
	45.50 kN	
	48.80 kN	
	51.60 kN	
	54.40 kN	

3.4 Measurement and Characterisation

3.4.1 Strain measurement

Previously reported methods of measuring the strain distribution in stamped parts used circle grids that were electrochemically etched onto the surface of the sheet, but the size of these grids exceeds the dimensions of the channels and an alternative method has been used here for micro-scale stamping. Strain distribution along the stamped channels was measured by polishing the cross-section of strips and making Vicker's diamond-pyramid hardness indents with a load of 25 g for 10 s, spaced 100 μm apart along the length of the sheet. The strips were then stamped and the spacing of the indents measured using an optical microscope. This method is illustrated in Figure 3. 6.

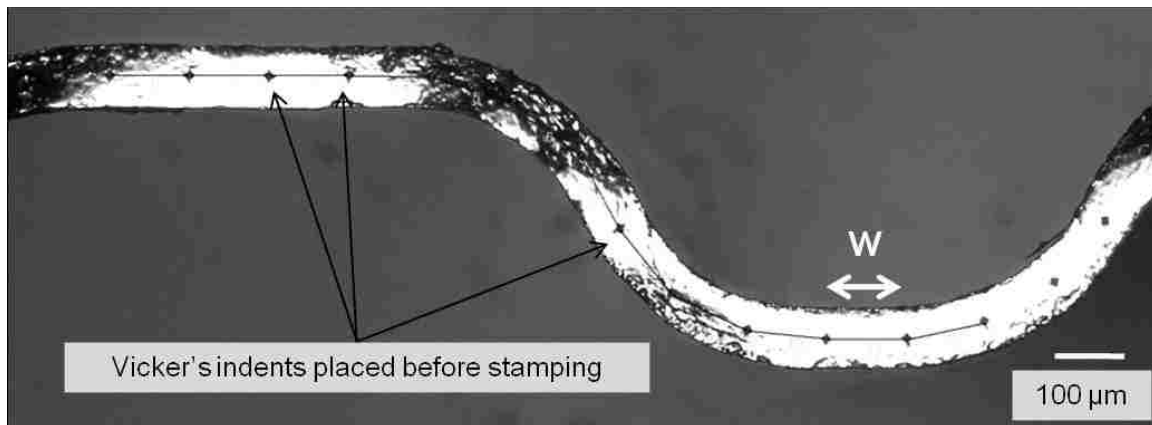
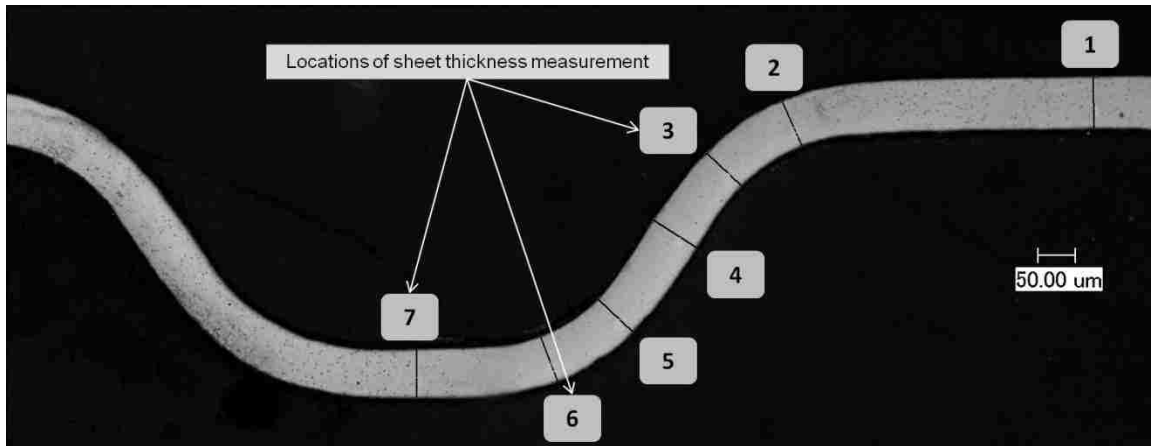
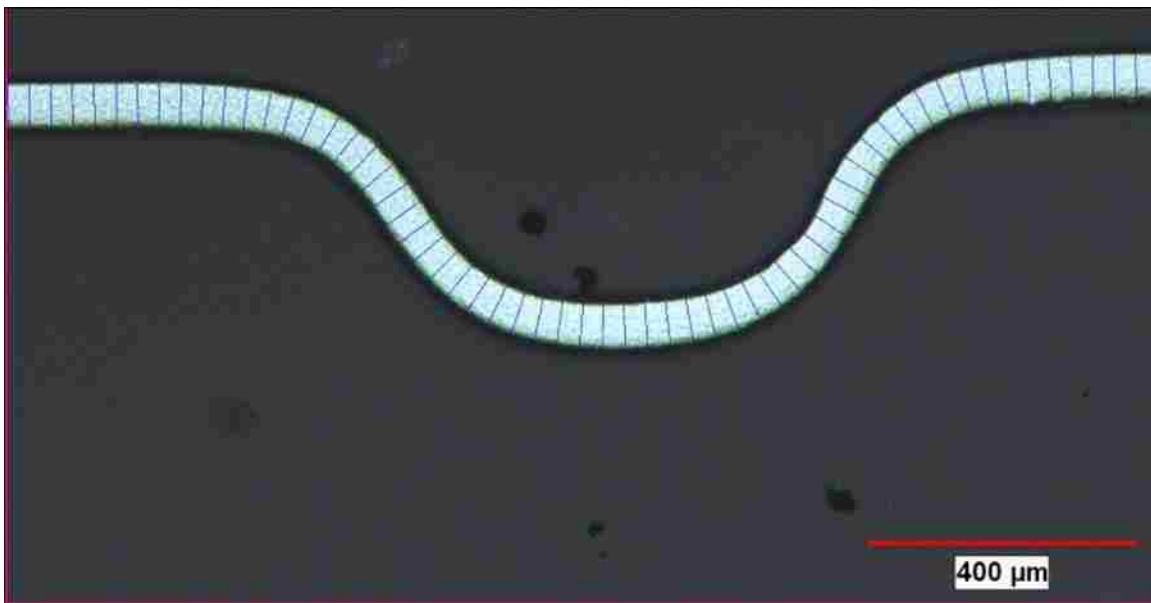


Figure 3. 6: The procedure employed in measuring tensile strains along the channel using Vicker's micro-hardness indents.

Quantitative dimensional measurements such as the depth of the channels and sheet thickness were made from optical micrographs of mounted cross-sectional samples. Mechanical polishing down to 1 μm diamond suspension was required to eliminate errors due to poor edge retention.



(a)



(b)

Figure 3. 7: The method of measurement used for calculating thickness strains in the stamped channel. Sheet thickness and channel depth measurements are made from polished cross-sections of the channels using an optical microscope as shown above, (a) in the seven locations indicated and (b) at 30 μm intervals for a finer strain distribution.

Figure 3. 7 (a) shows an example of how such a measurement was made. Measurement of sheet thickness was carried out at the seven locations indicated. Further, measurements were made at 30 μm intervals of the channel when a finer strain distribution

was required using Clemex Vision PE image analysis software, as is depicted in Figure 3. 7

(b).

Strain between two points ϵ_x , spaced 100 μm apart along the tensile direction is calculated as:

$$\epsilon_x = \frac{x_0 - x_i}{x} \quad (3.1)$$

Where x_0 is the initial indent spacing (100 μm) and x_i is the final indent spacing.

The through-thickness strain is calculated as:

$$\epsilon_y = \frac{t_0 - t_i}{t_0} \quad (3.2)$$

Where t_0 is the initial sheet thickness and t_i is the final sheet thickness measured at location i.

Due to the symmetry of the channel, measurements are made only on one half of the channel. Assuming volume constancy and plane-strain conditions, strain along the tensile direction and the negative of the through-thickness strain are equal. Strain in the thickness direction is used here for its ease of measurement.

3.4.2 Springback measurement: Channel depth

The depth of the channel was measured using optical microscopy. Stamped samples were metallographically mounted along their cross-section and polished. The depth of the channels was measured from the top of the channel land to the bottom of the channel as is shown in Figure 3. 8.

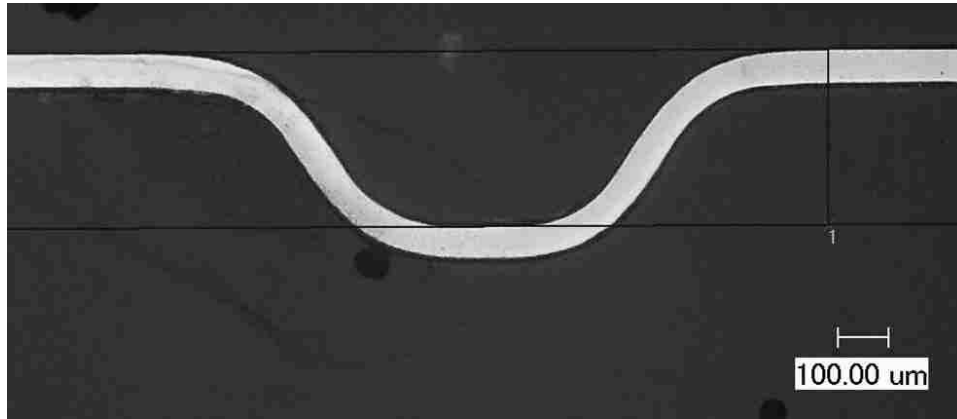


Figure 3. 8: The method of measuring channel depth using optical microscopy.

3.4.3 Microstructural characterisation

Microstructural characterisation of the material was performed by polishing mounted samples mechanically and then with 1 and 0.1 μm diamond suspension. They were then electrolytically etched in 60 % HNO_3 for 120 s using 1.5 V dc current. Stainless steel electrodes were used. Optical microscopy and scanning electron microscopy (SEM) were employed to observe the etched microstructures.

3.4.4 Characterisation of stamped surfaces

Surfaces of the stamped channels were observed using a JEOL 6400 scanning electron microscope (SEM) and surface roughness was measured using phase-shift optical profilometry (WYKO NT1100).

Surface roughness of the stamped channel was quantified by optical interferometry using monochromatic red light phase-shift interferometry (PSI). A 50x objective lens was used with a 1x field of view so as to maintain the area of measurement within the stamped channel. The area of measurement was 120 x 90 μm .

CHAPTER 4: Experimental Results

4.1 Introduction

This chapter presents the results of the experiments performed as described in the previous chapter. First, in section 4.2 the distribution of strain along the channel under the different stamping conditions is presented. Microstructural evolution upon stamping is presented next in section 4.3. Springback was measured by the lateral expansion of the five-channel series and by the depth of the channels, and the results are presented in section 4.4. Surface roughness and the surface morphology follow in section 4.5.

4.2 Distribution of Strain along the Stamped Channel

The locations of the equidistant Vicker's indents placed on a sheet and then channel stamped at 25 °C are shown Figure 4. 1(a) and the tensile strains calculated from these is shown in the strain distribution in Figure 4. 1 (b). The maximum ϵ_x was 0.15 and the minimum ϵ_x was 0.04 for the channel stamped at 25 °C. The through-thickness strains at these same locations which were found from the reduction in the sheet thickness at the same locations are plotted in Figure 4. 1(c). They were found to be equal to the tensile strain, thus confirming plane-strain conditions.

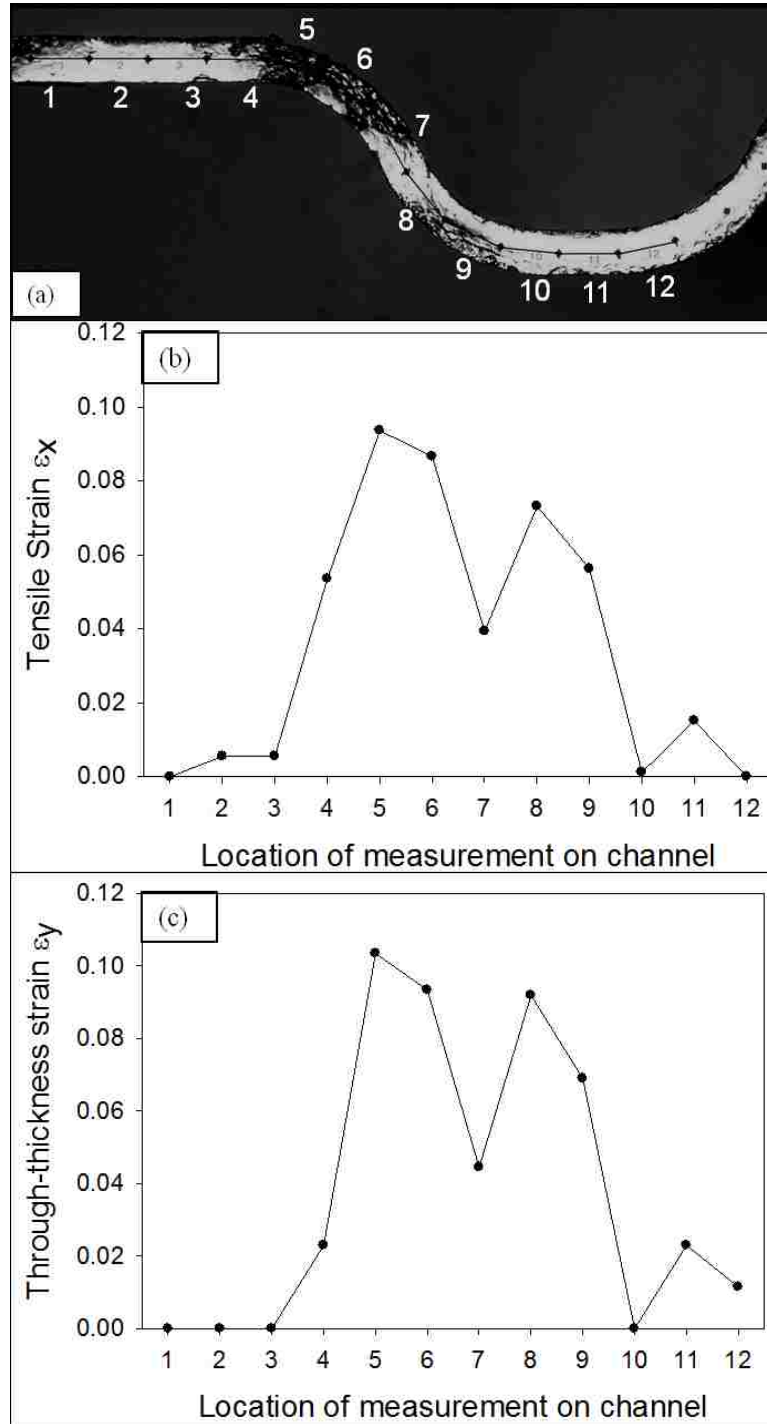


Figure 4. 1: (a) Locations of Vicker's indents along the cross-section of the channel after stamping. They were initially placed 100 μm apart and their spacing after stamping was measured using optical microscopy to calculate the tensile strain, plotted in (b). Through-thickness strains measured in the same locations as indicated in (a) are plotted in (c) to confirm plane-strain conditions.

4.2.1 Unlubricated stamping at elevated temperatures

Through-thickness strains were plotted for three loads (42.2, 48.8 and 54.4 kN) at the three temperatures tested. For these measurements seven locations were considered on the channel as indicated in Figure 3. 7. The through-thickness strain (ϵ_y) distribution at 25 °C is shown in Figure 4. 2(a). Strain peaks exist in the region between the radius and the channel wall (locations 3 and 5), while very low strain is experienced in the regions of the channel where the sheet is in contact with the die or the punch (locations 1 and 7). Increasing the temperature from 25 to 100 °C only marginally increases the ϵ_y strain peaks from 0.10 to 0.15 (Figure 4. 2[b]) but a further increase in temperature to 200 °C causes failure due to localised necking and the maximum ϵ_y increases to 0.33 (Figure 4. 2[c]). Cross-sections of channels stamped at these three temperatures are shown in Figure 4. 3. There is no visible thinning in the cross-section of the channel stamped at 25 °C and 100 °C shown in Figure 4. 3(a) and (b), but at all loads in the range tested at 200 °C, localised necking was observed as is seen in the micrograph in Figure 4. 3(c).

At 25 °C and 100 °C the most uniform distribution of strain is seen at the highest load considered, that is 54.4 kN. At 200 °C, a moderate load of 48.8 kN shows a more favourable strain distribution than the higher or lower loads.

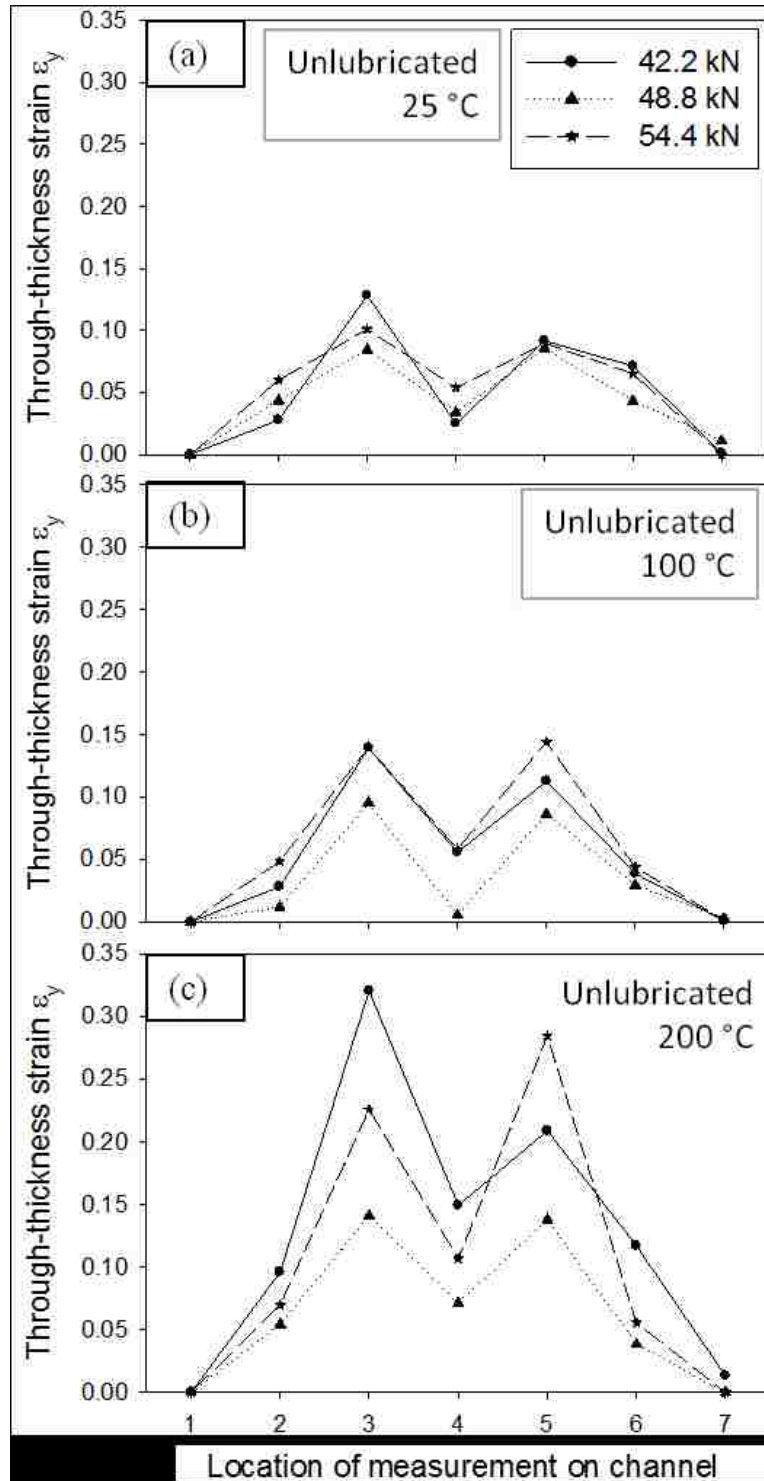


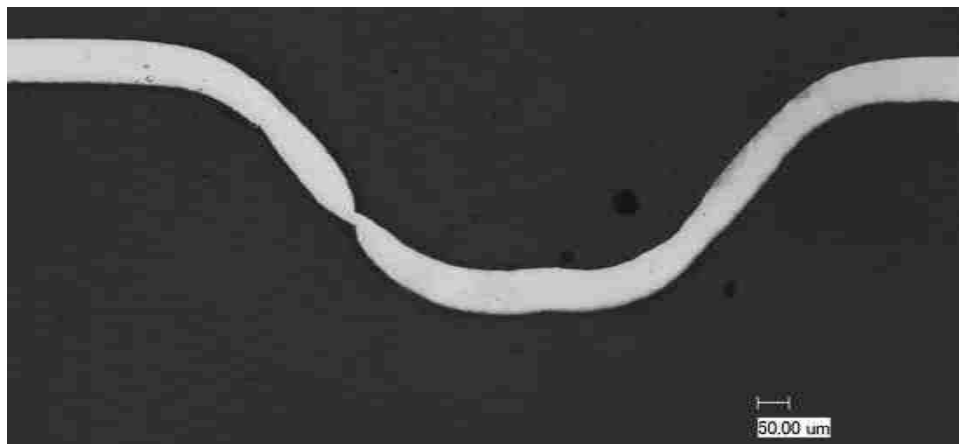
Figure 4. 2: Through-thickness strain along the channel at the seven locations indicated in Figure 3. 7 under unlubricated conditions at (a) 25 °C, (b) 100 °C and (c) 200 °C.



(a)



(b)



(c)

Figure 4. 3: Cross-sections of the channels stamped under unlubricated conditions at (a) 25 °C, (b) 100 °C and (c) 200 °C

4.2.2 Lubricated stamping at elevated temperatures

With lubrication, the distribution of ϵ_y improves with increasing temperature and favourable distribution occurs at lower loads. Figure 4. 4 shows the strain distribution along the stamped channel stamped with BN lubrication. The strain distribution is most favourable at 200 °C and moderate loads of 42.2 and 48.8 kN (Figure 4. 4 [c]). Figure 4.5 shows similar strain distribution plots for tungsten disulphide lubricated stamping and Figure 4. 6 shows the strain distribution for molybdenum disulphide lubrication.

The most uniform strain distribution was obtained from stamping with BN and MoS₂ at 200 °C where the strains at locations 2 through 7 on the channel are almost the same, at a stamping load of 42.2 kN (Figure 4. 4 (c) and Figure 4. 6 (c) respectively). On the other hand, WS₂ lubrication does not seem to prevent the localised straining to the same extent under the same conditions. With lubrication and higher temperatures, lower stamping loads (42.2 kN) produce better strain distribution.

In order to find the extent of localisation of the necking region, thickness strains were measured at 30 μm intervals on the stamped channel are shown in Figure 4. 7. Three typical conditions were selected, namely necking at 200 °C from unlubricated stamping, and lubricated stamping with WS₂ and MoS₂. A neck formed at 200 °C in Figure 4. 7 (a) shows that the sheet thickness is reduced by almost 70 % in the localised neck from the ϵ_y strain plot in Figure 4. 7 (b). Necking is highly localised and measures less than 30 μm in width. Strain distribution of channel stamped with WS₂ lubrication at 25 °C is plotted in Figure 4. 7 (d) for the locations shown in Figure 4. 7 (c). No necking is observed and the strain distribution is uniform without localisation. For the channel stamped with MoS₂ lubrication at 25 °C in

Figure 4. 7 (e), the strain distribution shows the complete absence of strain-peaks in the plot in Figure 4. 7 (f).

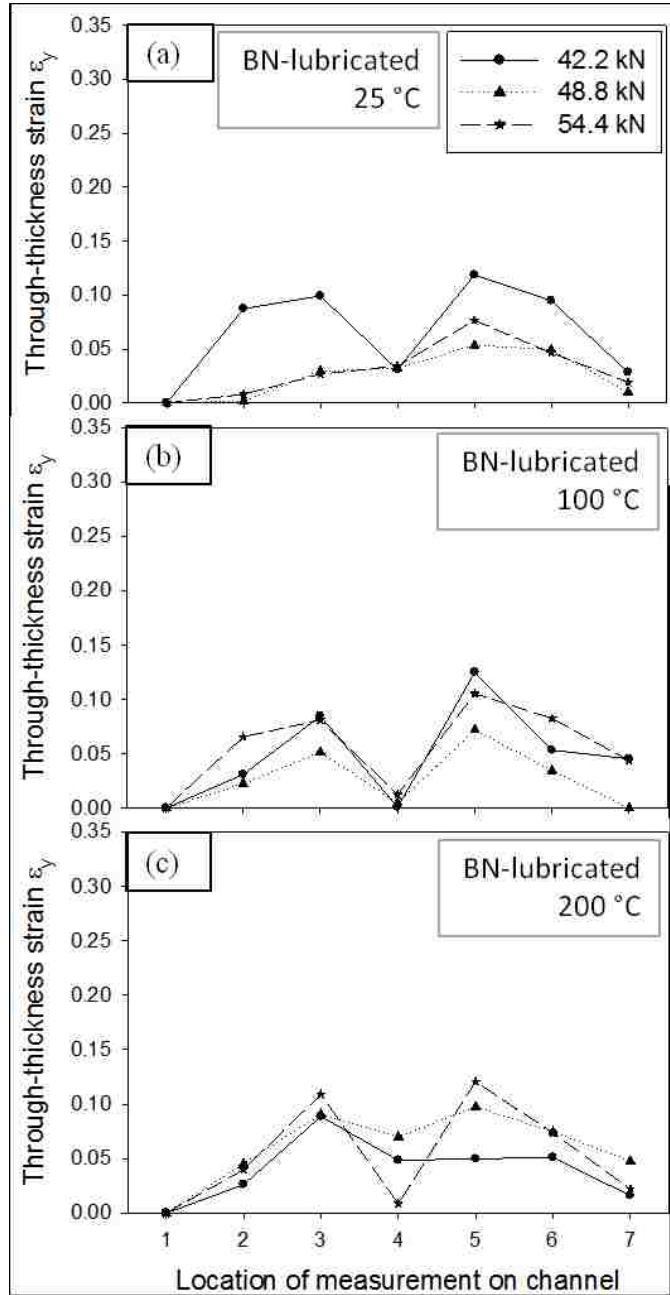


Figure 4. 4: Through thickness strain along the channel stamped with boron nitride lubrication at (a) 25 °C, (b) 100 °C and (c) 200 °C.

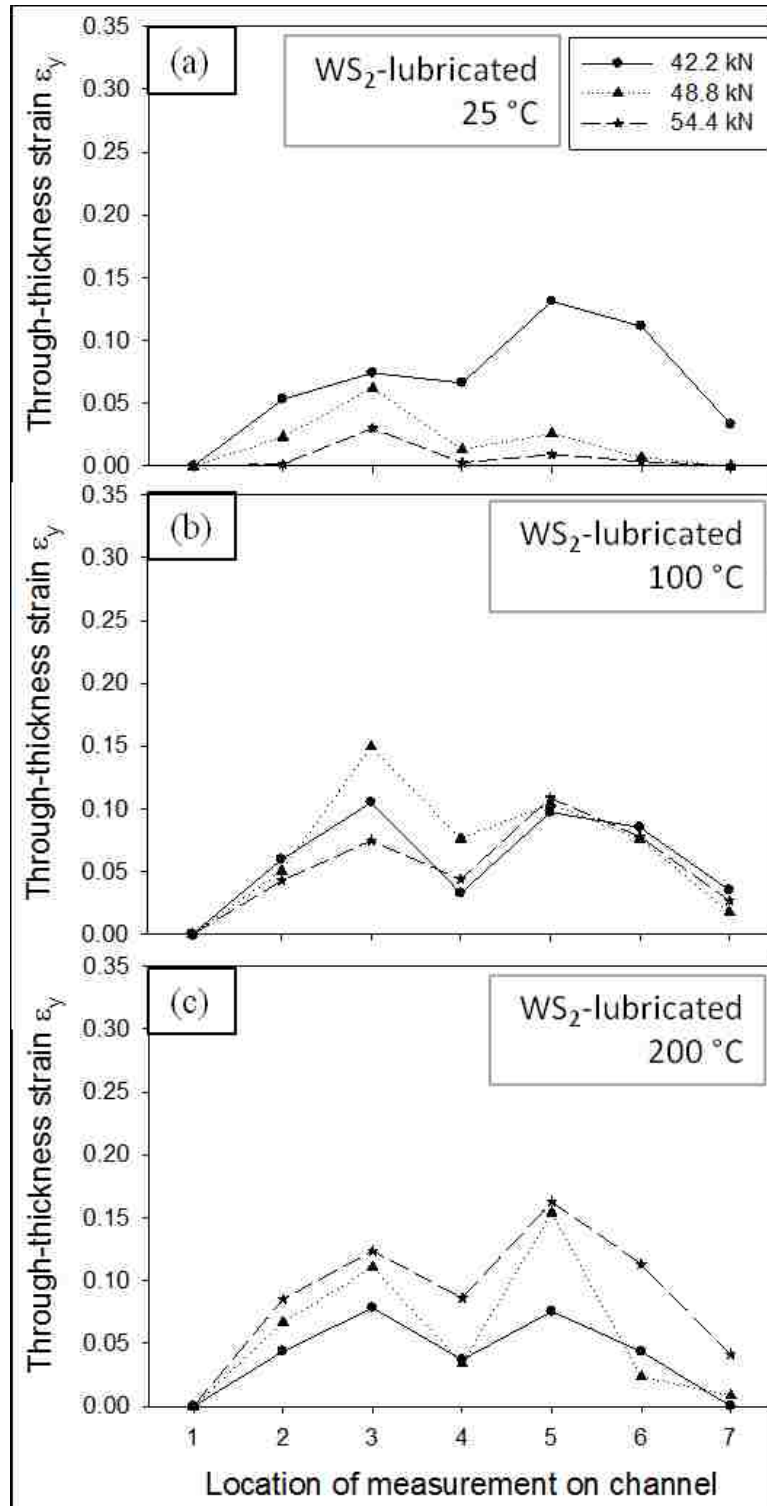


Figure 4. 5: Through thickness strain along the channel stamped with tungsten disulphide lubrication at (a) 25 °C, (b) 100 °C and (c) 200 °C.

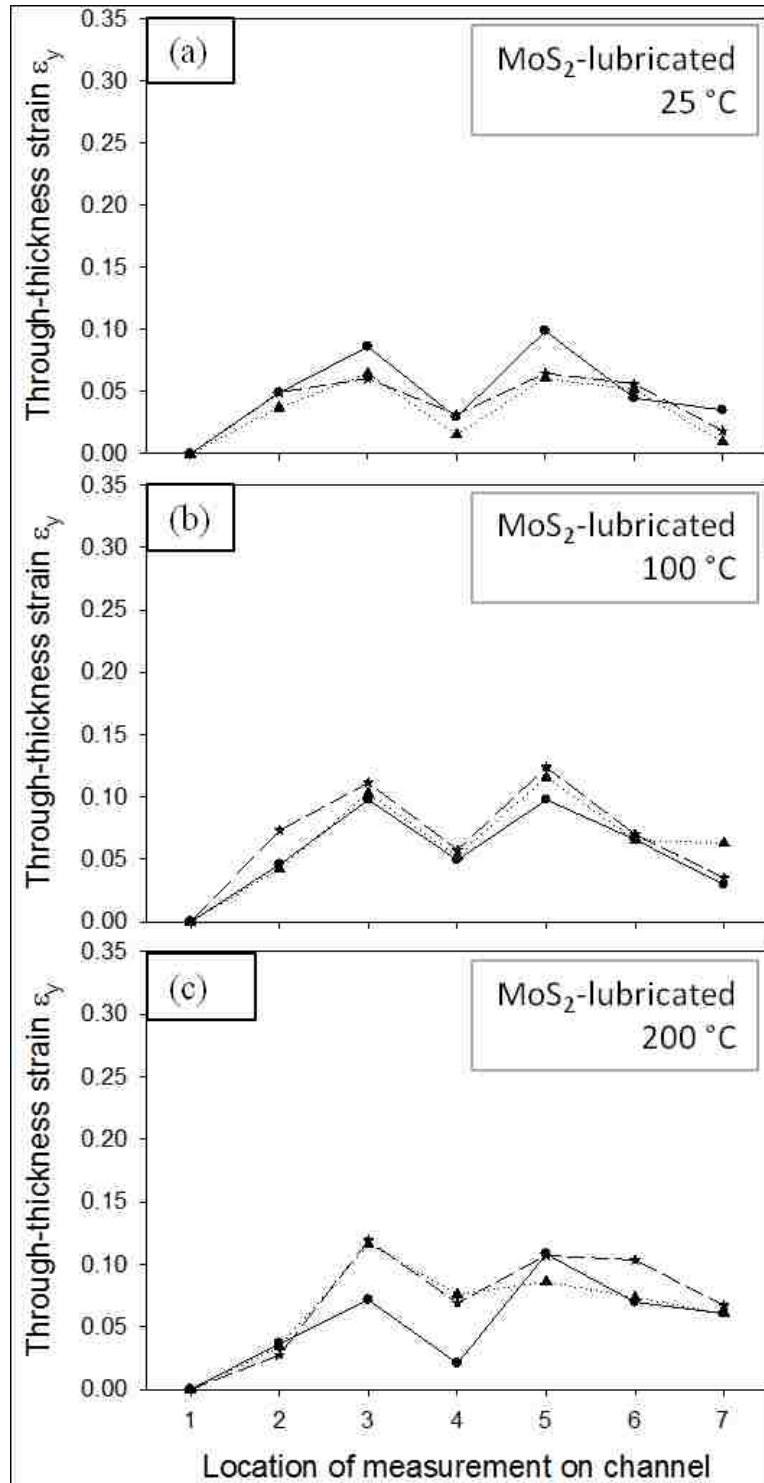


Figure 4. 6: Through thickness strain along the channel stamped with molybdenum disulphide lubrication at (a) 25 °C, (b) 100 °C and (c) 200 °C.

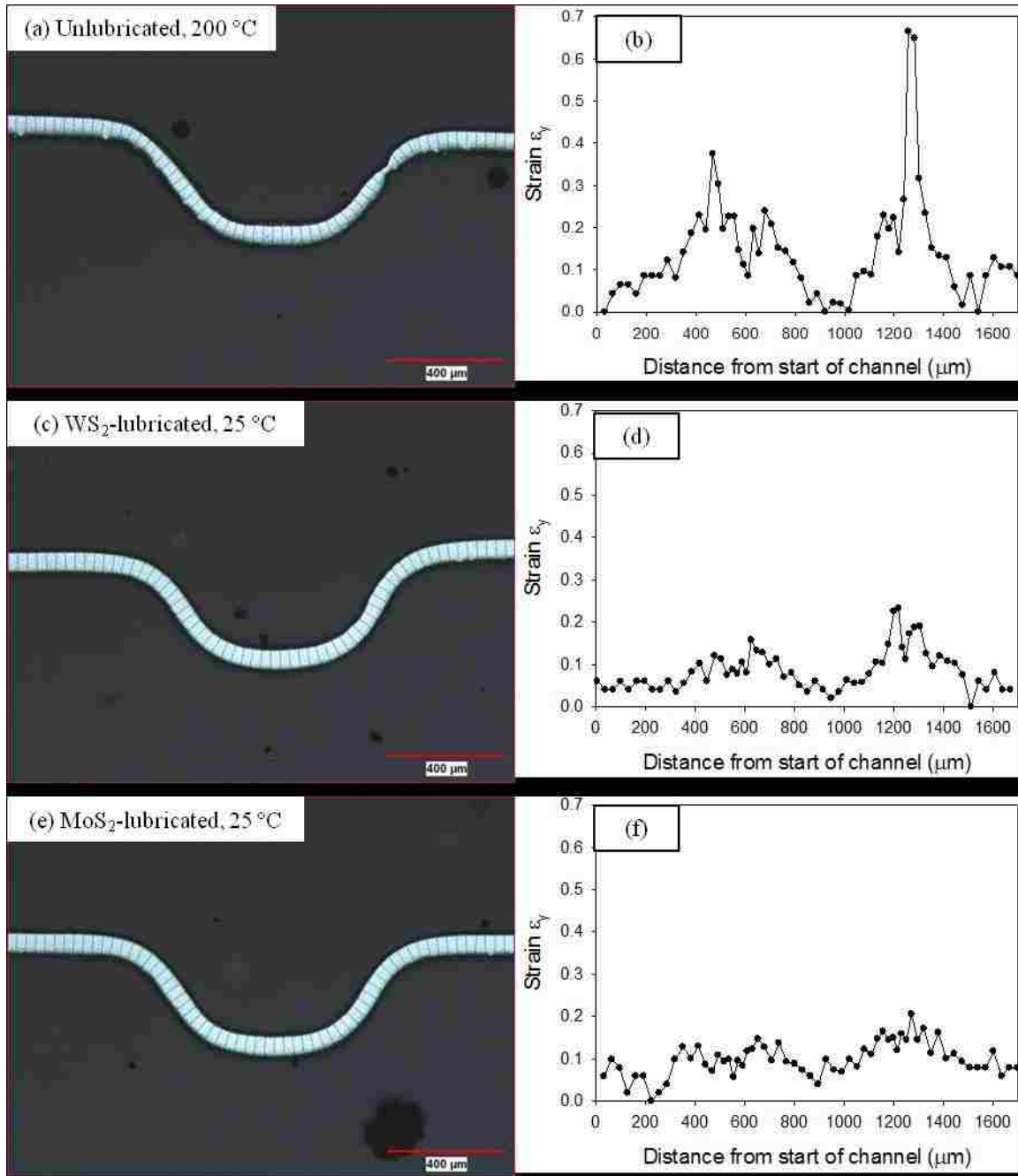
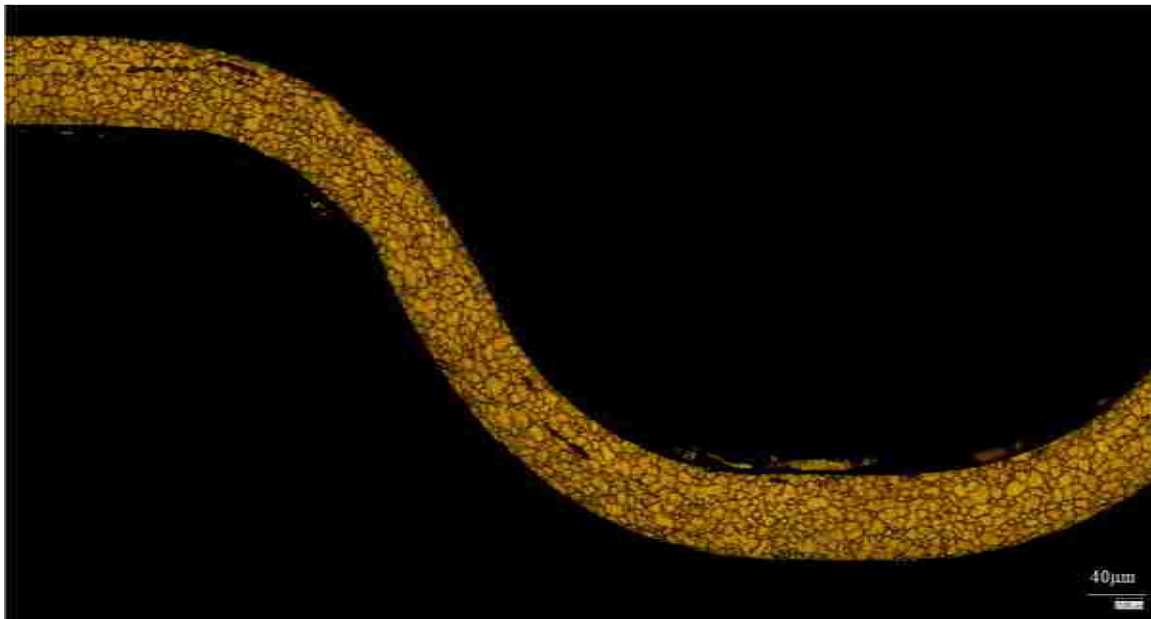


Figure 4. 7: Thickness strains calculated from sheet thickness measured at 30 μm intervals along the stamped channel. (a) Locations of measurement on channel stamped without lubrication at 200 °C and (b) the strains at these locations, (c) locations of measurement on channel stamped with WS₂ at 200 °C and (d) the strains at these locations, (e) locations of measurement on channel stamped with MoS₂ at 200 °C and (f) the strains at these locations.

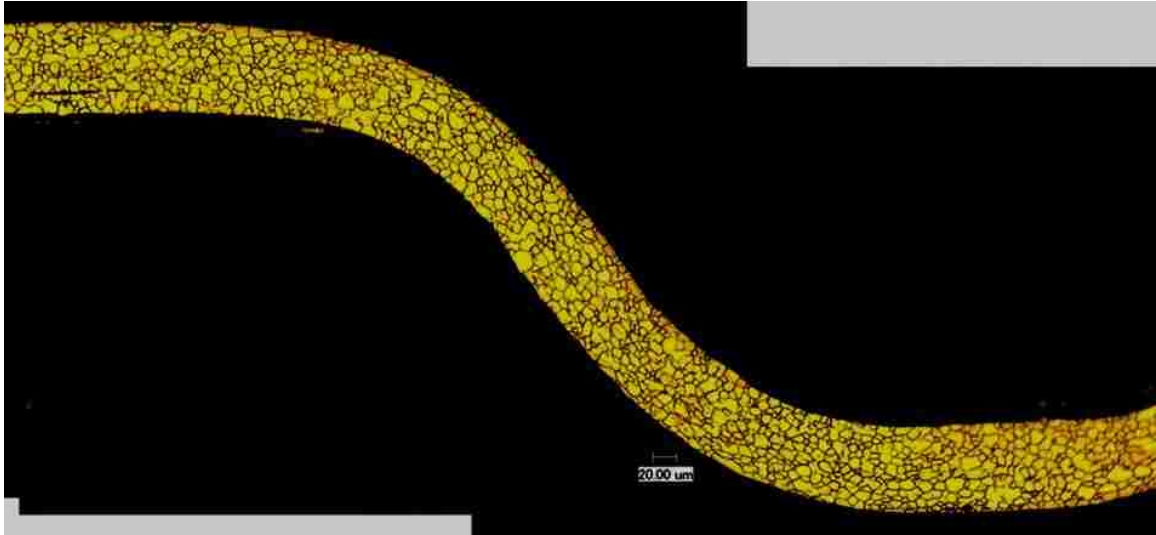
4.3 Microstructural Evolution

4.3.1 Unlubricated stamping

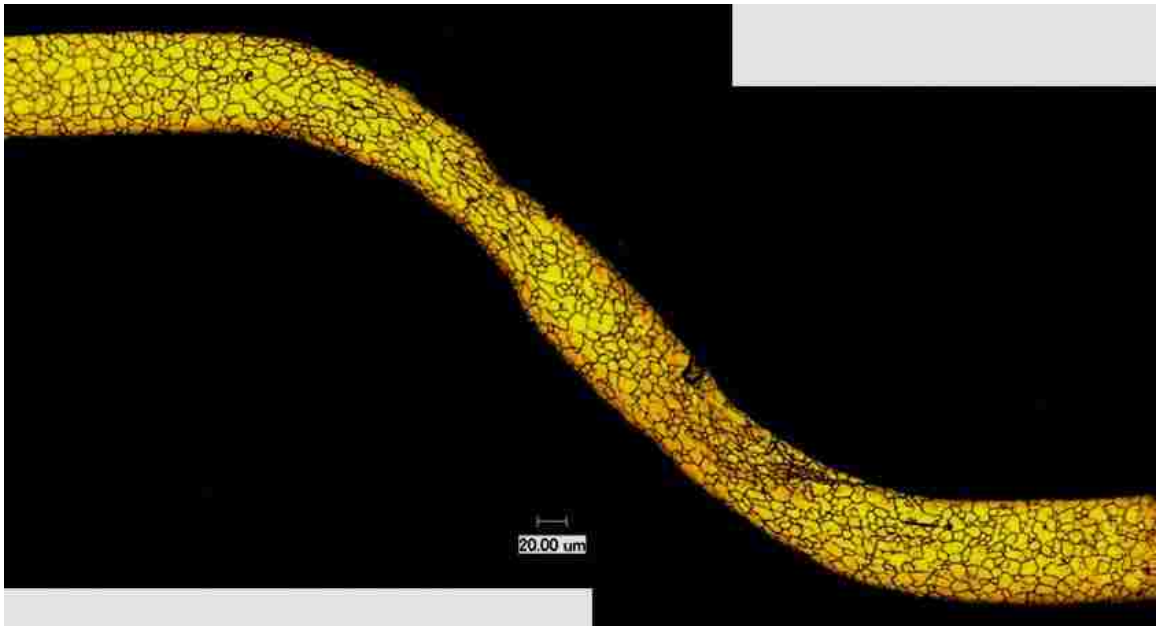
The microstructure of a channel stamped at 25 and 100 °C is shown in Figure 4. 8 (a) and (b). The grains are elongated on the outer side of the radius bends, where there is bending under tension (see location 2), while those on the inside of the bend are not. Grains are elongated along the channel sidewall as in location 4. Here the sheet is subjected to free uniaxial tension where the strain is high but not to the same extent as that on the outside of the radius bends. The channel stamped at 200 °C (Figure 4. 8[c]) on the other hand shows necking, which formed either at location 3 or 5 (i.e., bending and restraightening) under all loads at this temperature. The neck extends the length of 3 elongated grains, which indicates the extent of the localisation.



(a ..contd.)



(b)

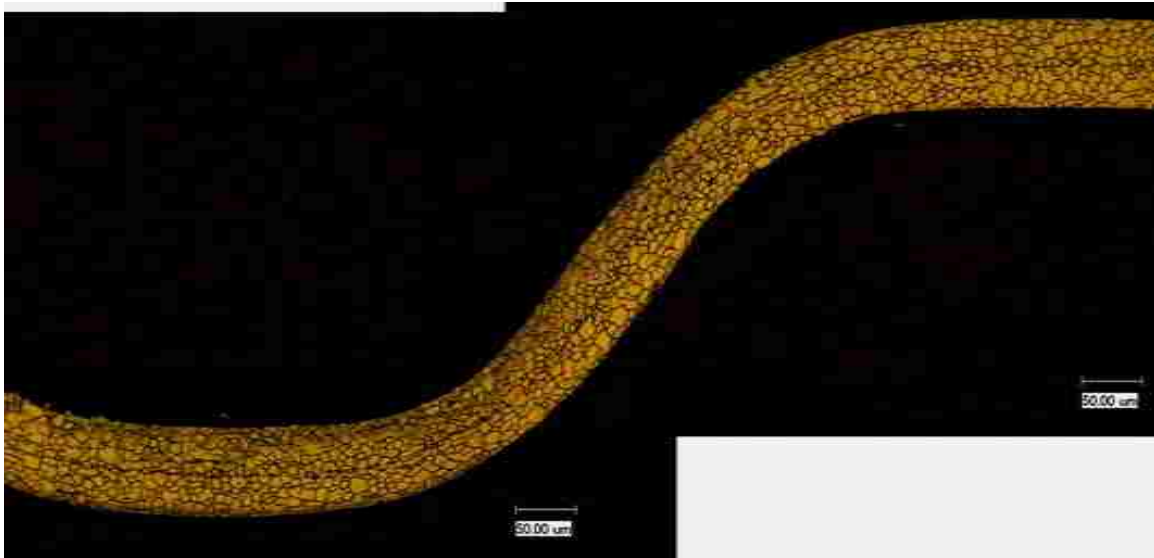


(c)

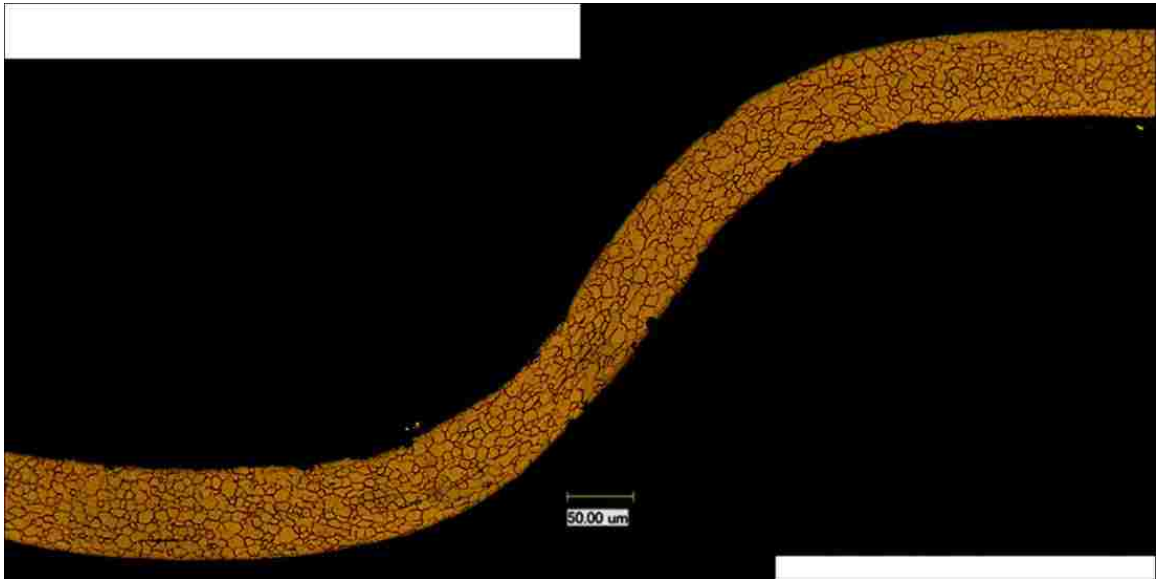
Figure 4. 8: The cross-sectional microstructures of the channels stamped without lubrication at (a) 25 °C, (b) 100 °C and (c) 200 °C. (Electrolytically etched with 60 % HNO₃).

4.3.2 Lubricated stamping at elevated temperatures

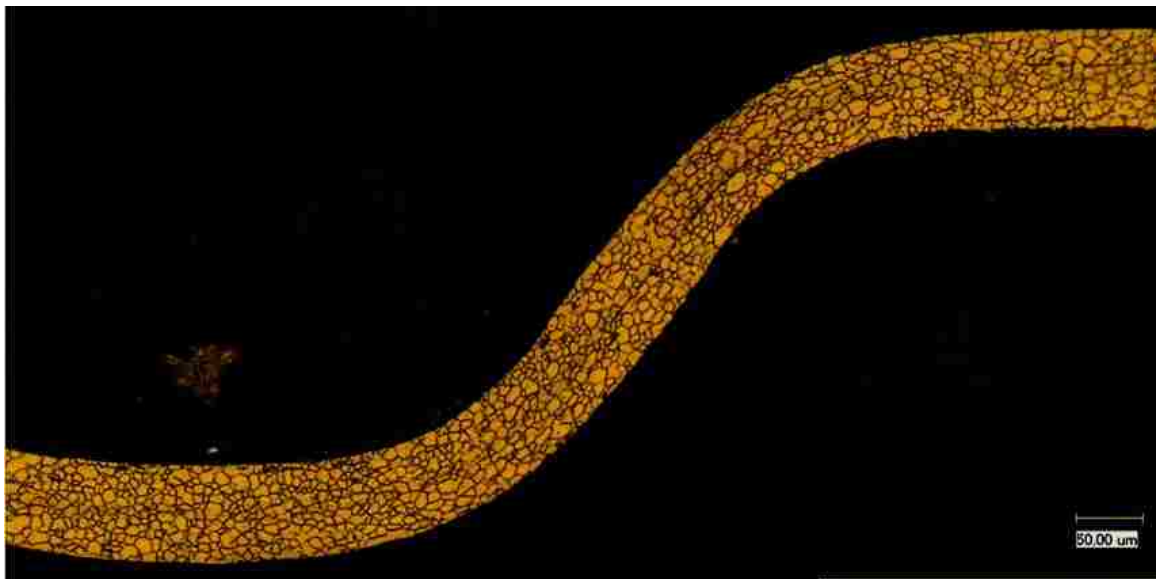
The microstructure of a channel stamped with BN, WS₂ and MoS₂ all at 200 °C with a stamping load of 48.8 kN are shown in Figure 4. 9. Necking is absent and there is a favourable distribution of sheet thickness along the entire channel. The localised occurrence of elongated grains is absent and this set of conditions exhibited the most uniform strain distribution (48.8 kN, 200 °C, MoS₂ lubrication in Figure 4. 9 [c]). The coarse precipitates do not seem to have any effect on the formability and they appear to behave like the matrix grains under straining.



(a ..contd.)



(b)



(c)

Figure 4. 9: The cross-sectional microstructures of the channels stamped at 200 °C with (a) BN, (b) WS_2 and (c) MoS_2 . (Electrolytically etched with 60 % HNO_3).

4.4 Springback Effects

4.4.1 Channel depth

The targeted depth of the channels in the die was 350 μm , but the actual depth of the stamped channels was less than this depth under all conditions. The incomplete channel depth was caused by springback that resulted from the recovery of the elastic component of the strain upon removal of the stamping load. The increased angle of the channel wall as a result of bending springback affects the depth of the stamped channel as is depicted in the schematic in Figure 2. 6.

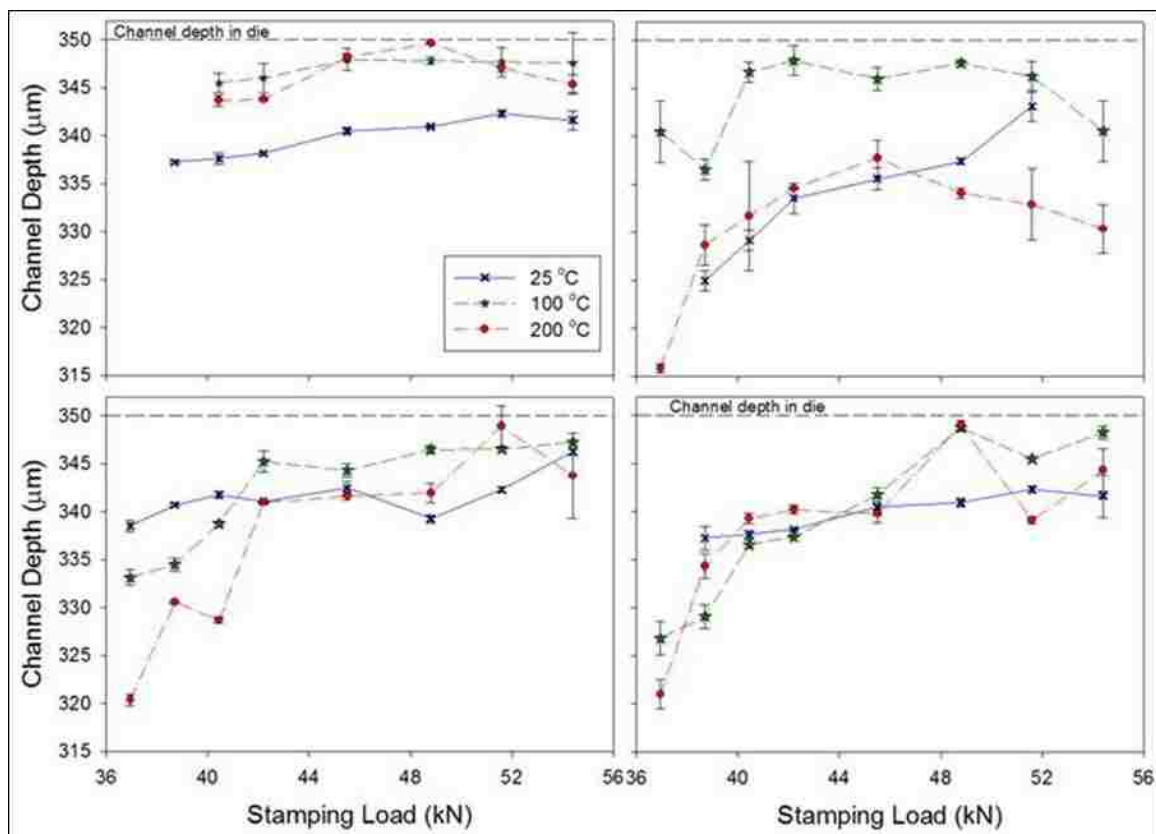


Figure 4. 10: Variation of channel depth with load at 25, 100 and 200 °C, (a) unlubricated, (b) BN, (c) WS₂ and (d) MoS₂.

The depths of the channels stamped under all the conditions in plotted in Figure 4. 10. The depth of the channel increases with temperature under unlubricated conditions (Figure 4. 10 [a]). Channel depth increases with stamping load until a maximum for that temperature is attained, and then remains constant. The depth of the channels increased with increasing the load up to a maximum, which was attained at 47.2 kN at 25 °C and at a lower load of 42.2 kN at 100 °C. At elevated temperatures, the depth of the channels increased by nearly 2 % due to the reduction in yield stress with temperature at a load of 51.6 kN. At 100 °C, the maximum depth attained was $347.96 \pm 1.17 \mu\text{m}$, while at 25 °C it was $344.13 \pm 0.35 \mu\text{m}$. At 200 °C, there was a reduction in channel depth at the higher end of the load range above 48.8 kN, which accompanied the adhesion of the sheet to the die at that temperature.

Lubrication does not significantly affect the depth of the channels stamped at 25 and 100 °C, but at 200 °C, channels stamped with lubrication are not as deep as those formed with unlubricated stamping (Figure 4. 10[b-c]). In addition to springback, channel depth in lubricated stamping is affected by the thickness of the lubricant film itself, and BN reduces the depth of the channels by 5 μm more than the other lubricants at elevated temperatures (Figure 4. 10[b]).

4.5 Roughening and Morphology of Stamped Surfaces

4.5.1 Roughness of stamped surfaces

The surface roughness (R_a) measured on the punch-side and die-side of the channels and its variation with temperature and stamping load under unlubricated conditions is shown in Figure 4. 11. The surface roughness of the undeformed blank was $100.53 \pm 1.7 \text{ nm}$. The roughness on the die-side was considerably higher than on the punch-side. The punch-side

shows only a slight increase in surface roughness with temperature, while the die-side surface roughness increased dramatically with an increase in temperature. The surface roughness on both sides showed an increase with stamping load.

The surface roughness for channels stamped with BN lubrication plotted in Figure 4. 12, lower loads produce erratic roughness, but moderate to high stamping loads show an almost steady roughness with load. The roughness is invariant with temperature. For WS₂ lubrication, there is a slight decrease in surface roughness with temperature, as is seen in the plots in Figure 4. 13. MoS₂ produced higher surface roughness than BN and WS₂ which increased slightly with temperature (Figure 4. 14).

The reduction in surface roughness due to the use of lubrication is more marked at elevated temperatures than at 25 °C. BN shows the best reduction in the surface roughness at 25 °C, whereas the performance of WS₂ at elevated temperatures is best. Under all conditions, the surface roughness is greater on the die-side of the stamped channel than on the punch side.

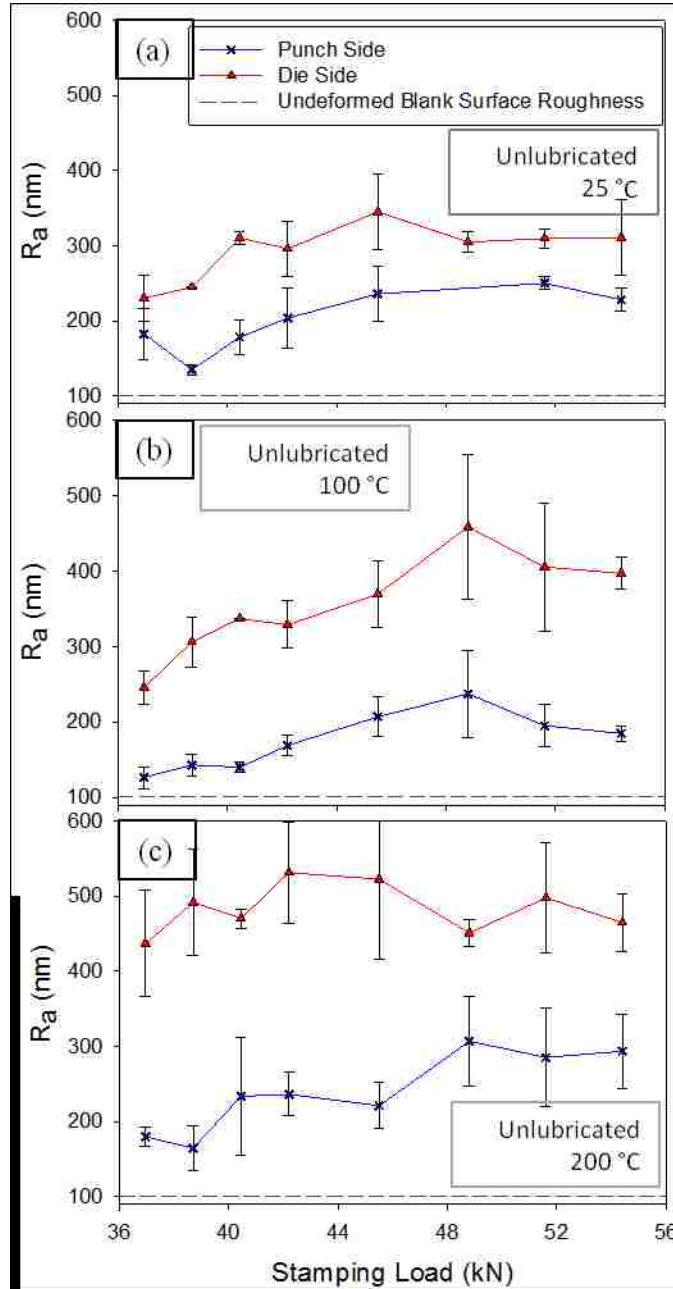


Figure 4. 11: The variation of surface roughness of the stamped channels with stamping load on the punch and die sides stamped under unlubricated conditions at (a) 25 °C, (b) 100 °C and (c) 200 °C.

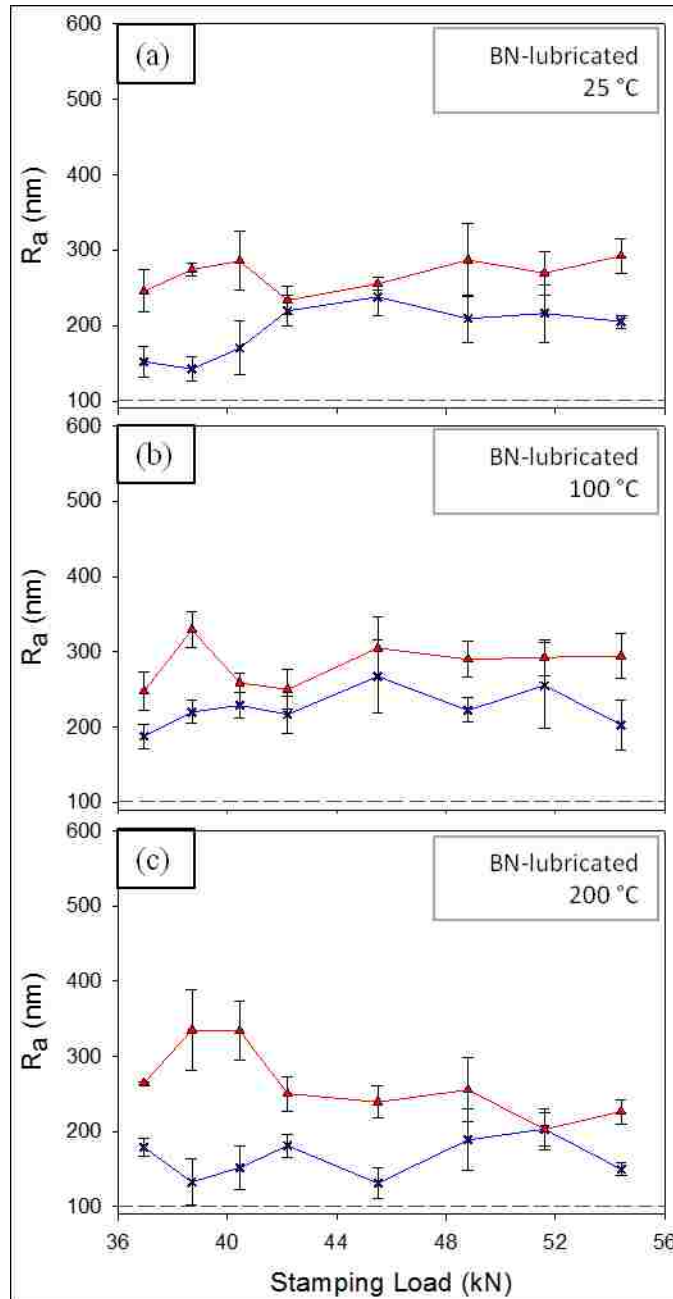


Figure 4. 12: The variation of surface roughness of the stamped channels with stamping load on the punch and die sides stamped with boron nitride lubrication conditions at (a) 25 °C, (b) 100 °C and (c) 200 °C.

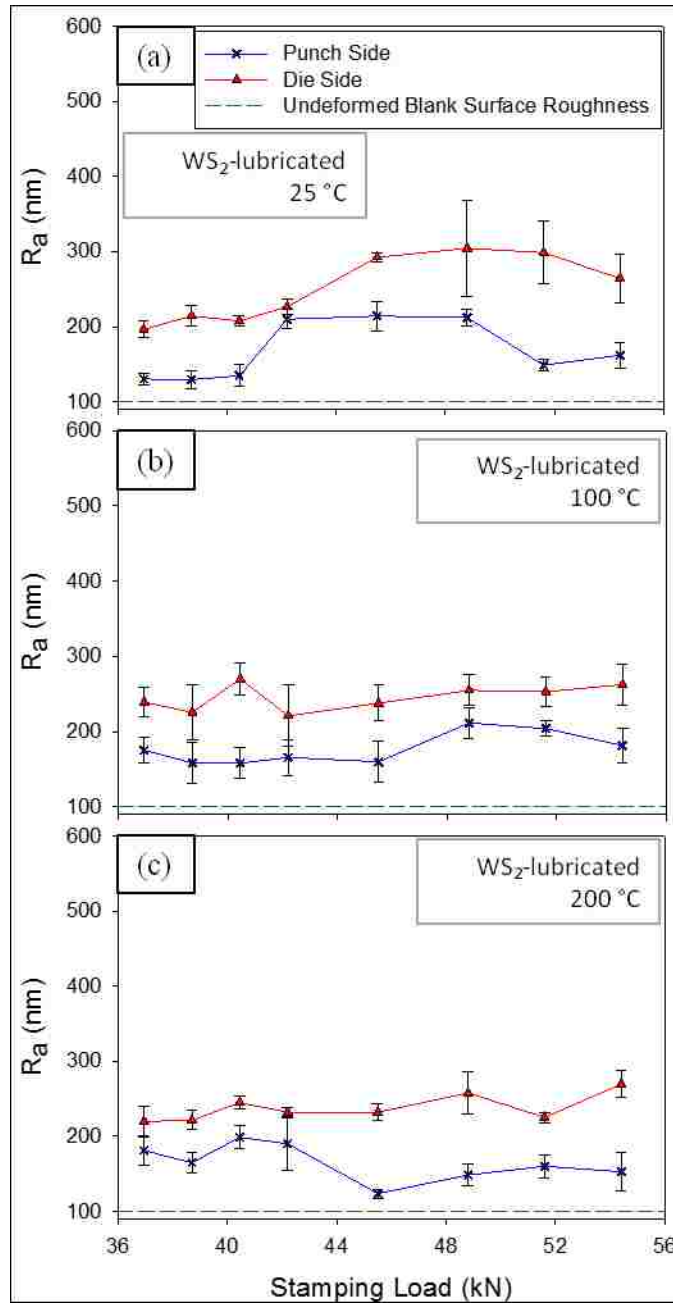


Figure 4. 13: The variation of surface roughness of the stamped channels with stamping load on the punch and die sides stamped with tungsten disulphide lubrication conditions at (a) 25 °C, (b) 100 °C and (c) 200 °C.

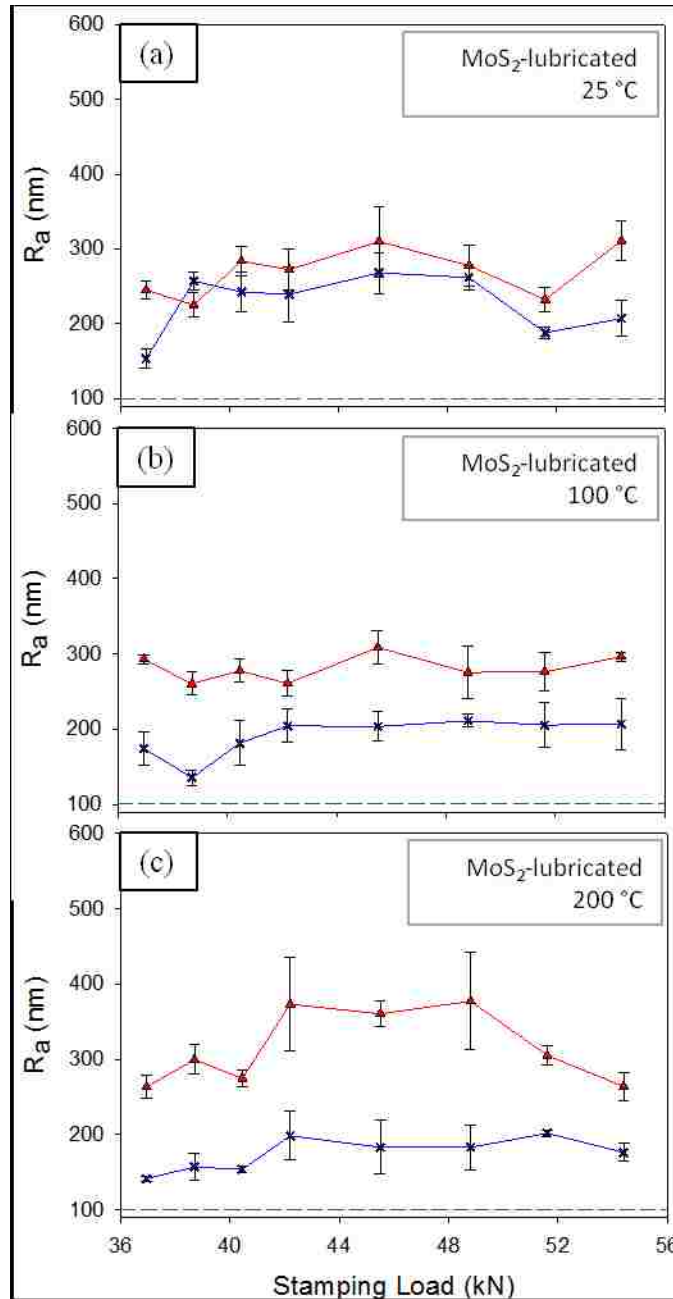


Figure 4. 14: The variation of surface roughness of the stamped channels with stamping load on the punch and die sides stamped with molybdenum disulphide lubrication conditions at (a) 25 °C, (b) 100 °C and (c) 200 °C.

4.5.2 Surface morphology of stamped channels

SEM images in Figure 4. 15 of the surfaces of the channels stamped without lubrication at 200 °C on the punch and die sides show the difference in morphology due to the different types of contact, namely sliding on the punch side (Figure 4. 15 [a] and [b]), and purely normal contact on the die side (Figure 4. 15 [c] and [d]). The channels on the inside and the outside of the radius bends show different surface morphologies as well. The inside of the bends show sliding wear as can be seen in the SEM image of Figure 4. 16(a). The outside of the radius bend where there is no contact with the die at any instant of the process shows roughening on the grain scale as seen in Figure 4. 16 (b) due to the relative movement of the neighbouring grains to accommodate the strains experienced during the process.

The surfaces of the channels stamped with BN are relatively damage free as can be seen in Figure 4. 17 (a) of the punch side and Figure 4. 17 (b) of the die side.

With WS₂ lubrication, damage is not observed either, but rather, transfer layers of the lubricant are formed. WS₂-lubricated stamping at 200 °C produced a transfer layer only on the punch side, as is seen in

Figure 4. 18 (a), and the backscatter image of the same location in Figure 4. 18 (b) shows the transfer layer appearing as bright patches indicating the presence of tungsten. The die-side does not have any transfer layers as can be seen from

Figure 4. 18 (c) and (d). MoS₂-lubricated stamping shows transfer layer formation on both the punch and die sides (Figure 4. 19). The transfer layers appear to be in the plate-like form as is seen in Figure 4. 20 (a) on the punch side of the channel stamped with MoS₂. The die side transfer layer is not arranged in plate-like form as can be seen from the SEM and back-scattered electron image in Figure 4. 20 (b) and (c).

Damage on a smaller scale than was seen in unlubricated stamping was observed at 100 and 200 °C under lubricated conditions on the die side of the channels such as that seen

in Figure 4. 21. Surface roughness is higher on the die side than on the punch side. WS₂ reduces the surface roughness most at elevated temperatures, although transfer layers are formed on the die side. MoS₂ produces transfer layers on the punch side as well as on the die side and is not as effective at elevated temperatures.

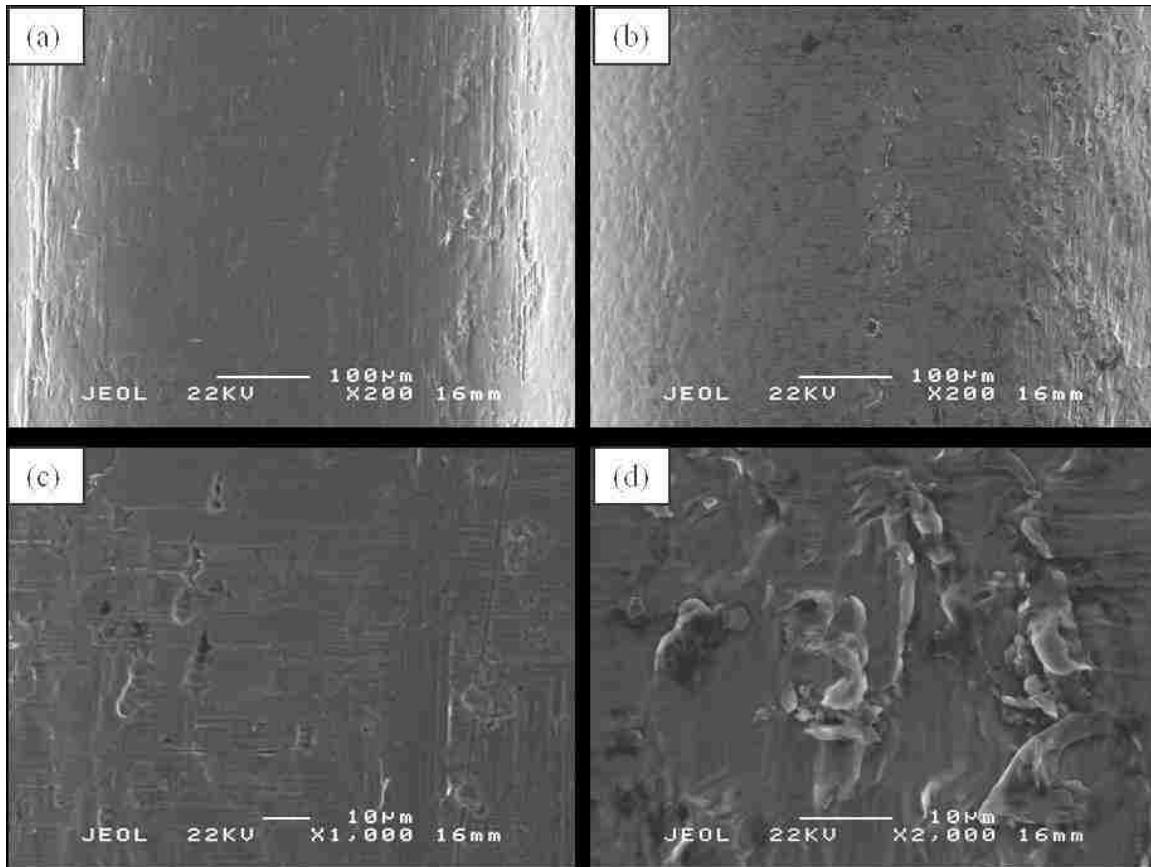
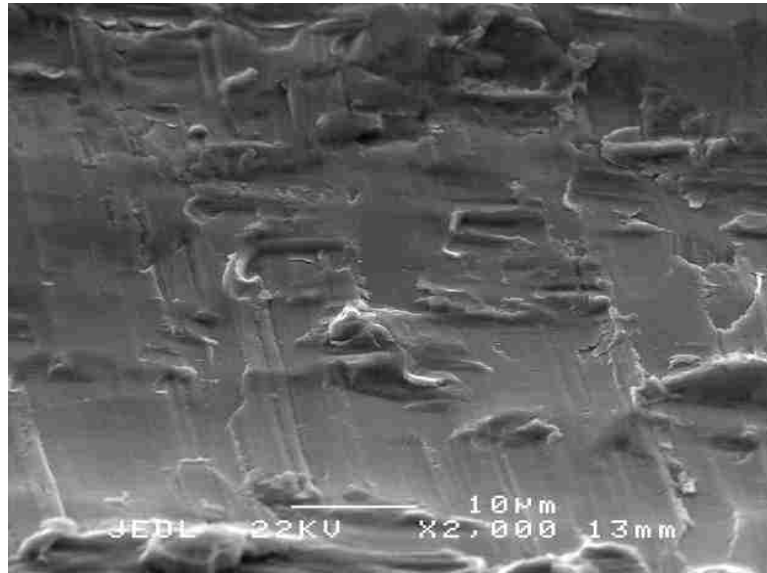
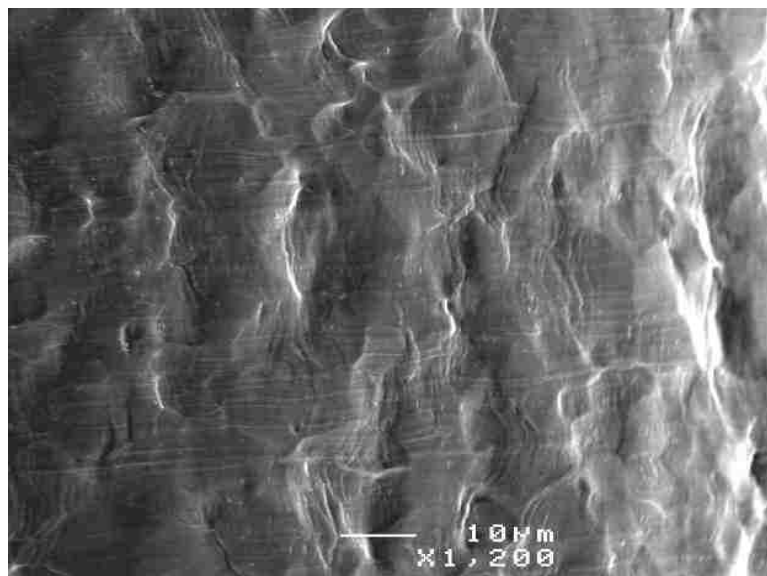


Figure 4. 15: SEM images of channel surfaces stamped without lubrication at 200 °C on (a) the punch side and (b) the die side. (c) and (d) show high magnification images of the punch and die sides respectively.

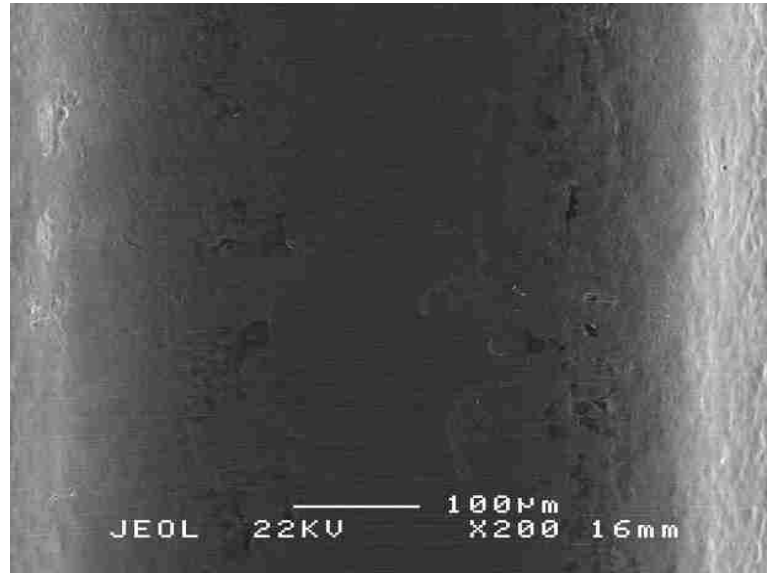


(a)

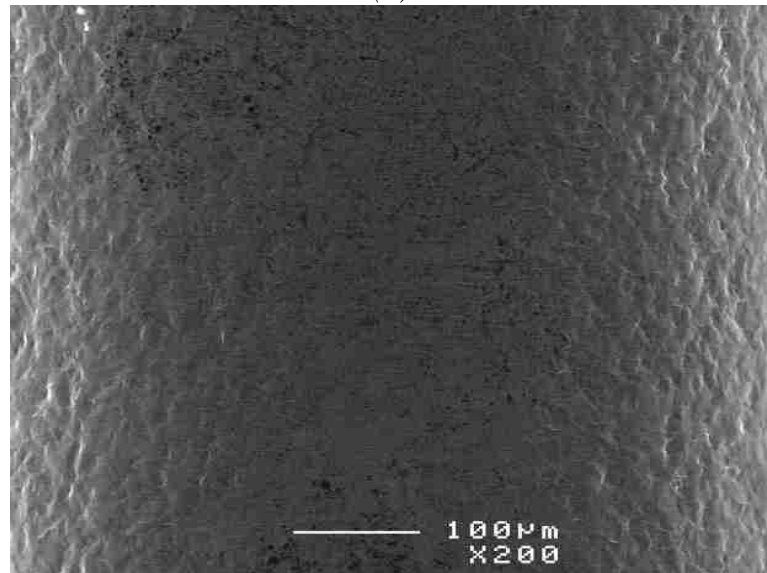


(b)

Figure 4. 16: SEM images of channel surfaces stamped without lubrication at 25 °C on the (a) inside and (b) outside of the die radius.



(a)



(b)

Figure 4. 17: SEM images of the surfaces stamped at 200 °C with BN lubrication on (a) the punch side and (b) the die side.

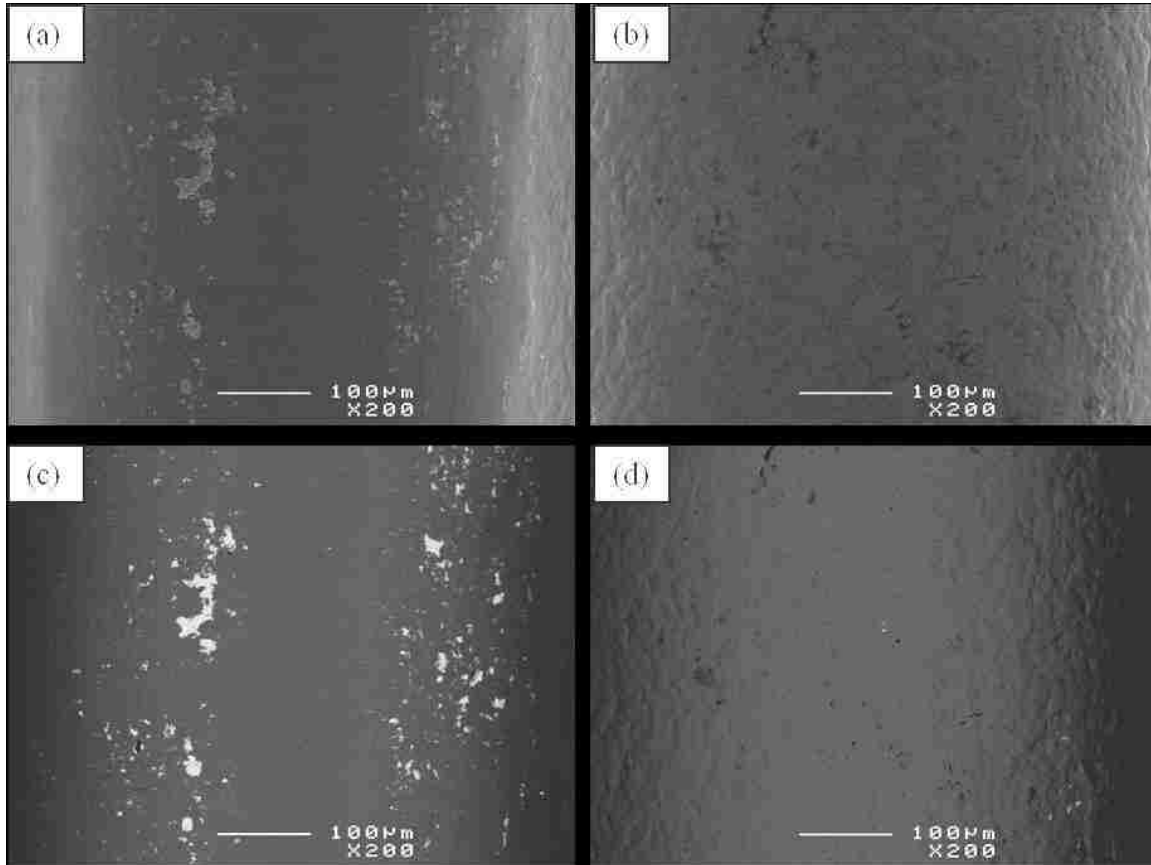


Figure 4. 18: SEM images of the surfaces stamped at 200 °C with WS₂ lubrication on (a) the punch side and (b) the die side. (c) Backscattered electron image of the location corresponding to (a) showing bright patches indicative of the presence of the heavier tungsten in the transfer layers, whereas the backscattered electron image of the die side in (d) corresponding to (b) indicates the absence of tungsten and therefore any transfer layers.

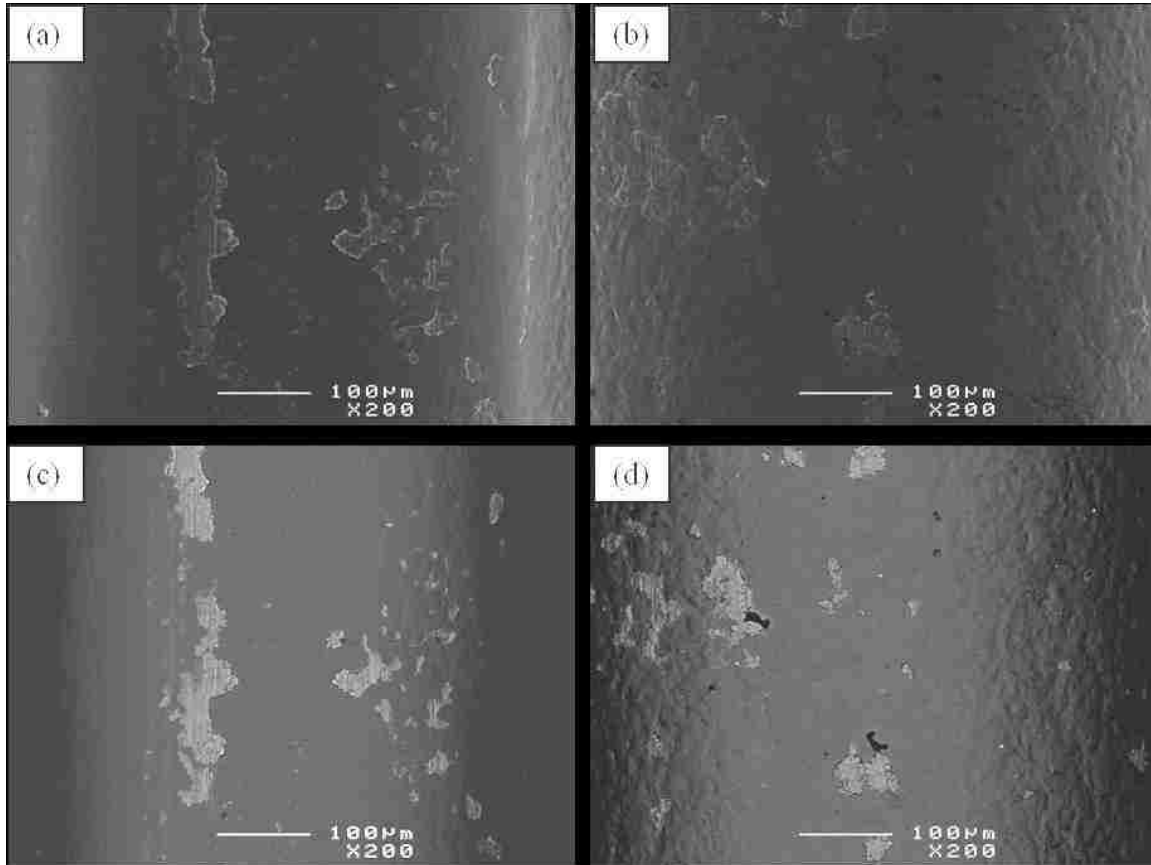
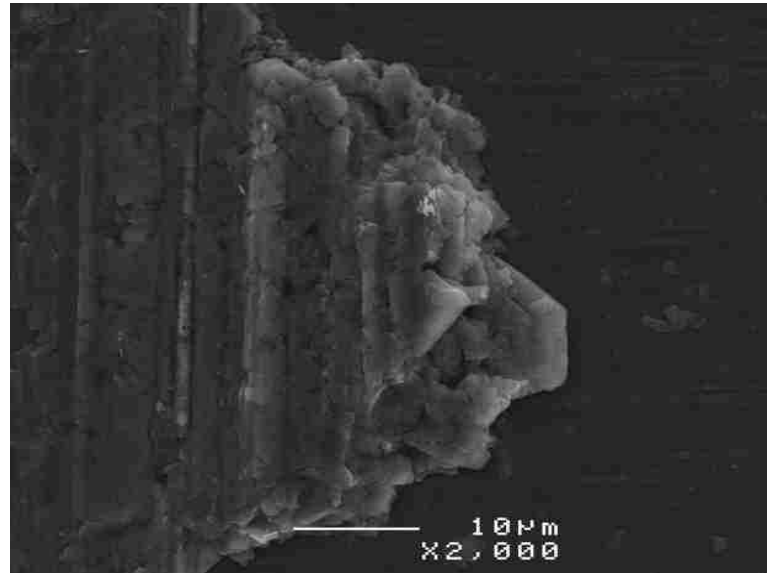
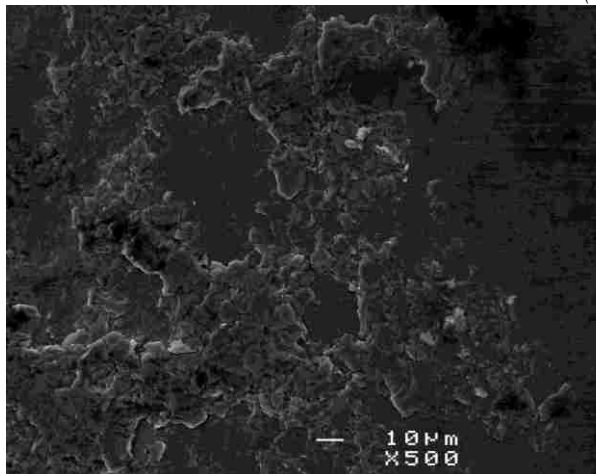


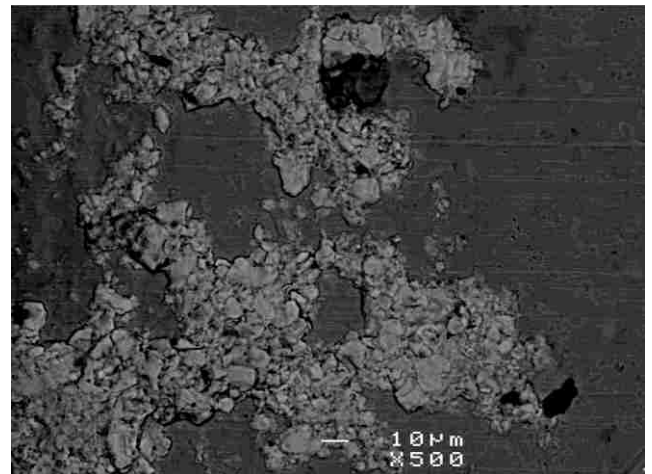
Figure 4. 19: SEM images of the surfaces stamped at 200 °C with MoS₂ lubrication on (a) the punch side and (b) the die side. (c) and (d) are backscattered electron images corresponding to (a) and (b) respectively, and bright patches in both images indicate the presence of transfer layers containing molybdenum on both the punch and die sides of the stamped channel.



(a)



(b)



(c)

Figure 4. 20: SEM images of the transfer layers formed on surfaces stamped at 200 °C with MoS₂ lubrication showing the difference in morphology of the transfer layers formed on the two sides of the channel. (a) Punch side transfer layer assuming a lamellar morphology, (b) die side transfer layer of an agglomerated morphology and (c) the corresponding backscattered electron image of (b).

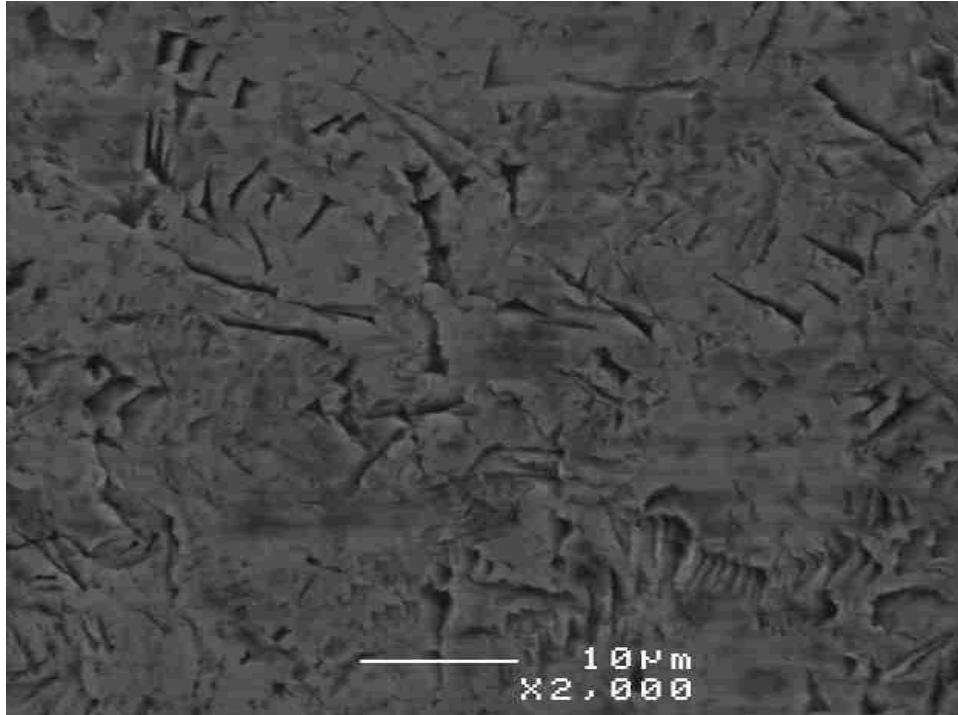


Figure 4. 21: Nature of damage made by the lubricant particles on the die-side of the channel stamped at 100 °C with BN lubrication.

CHAPTER 5: Discussion of Results

5.1 Introduction

Results of the experiments conducted thus far show that friction plays an important role in limiting the formability in this process and an attempt has been made in Section 5.2 to understand it in order to improve the quality of stamped bipolar plates. With the observations made in the previous chapter, a tribological model has been developed to explain the nature of deformation and die contact that the sheet experiences during the process. The effects of first temperature and then lubrication on this ensue in Sections 5.3 and section 5.4 respectively. Within the stamping parameters selected for the study, a processing window in which the stamping quality is optimum has been arrived at and is presented in Section 5.5.

5.2 Tribology of the Stamping Process

Friction between the punch and the sheet during stamping opposes deformation. Peaks in the strain distribution exist away from the pole of the punch in a region known as the ‘crown’ [13]. This was attributed to the friction between the sheet and the punch and failure due to necking occurred there. Although the deformation and strain states are different in plane-strain channel stamping from those in punch-stretching or cylindrical deep drawing, the tribology and contact nature are comparable. Figure 5. 1 shows a schematic of the forces acting on a sheet undergoing plane-strain channel stamping. According to the tribological model of deep-drawing presented by Schey (1983) [28], the maximum pressure is experienced at the die radii where the sheet is bent over the die under tension. The high circumferential stresses cause the frictional force to be greatest at

this location. There are three distinct types of deformation along the channel: tensile deformation opposed by the frictional force of punch (or die), uniaxial tensile stretching without any contact friction, and bending under tension.

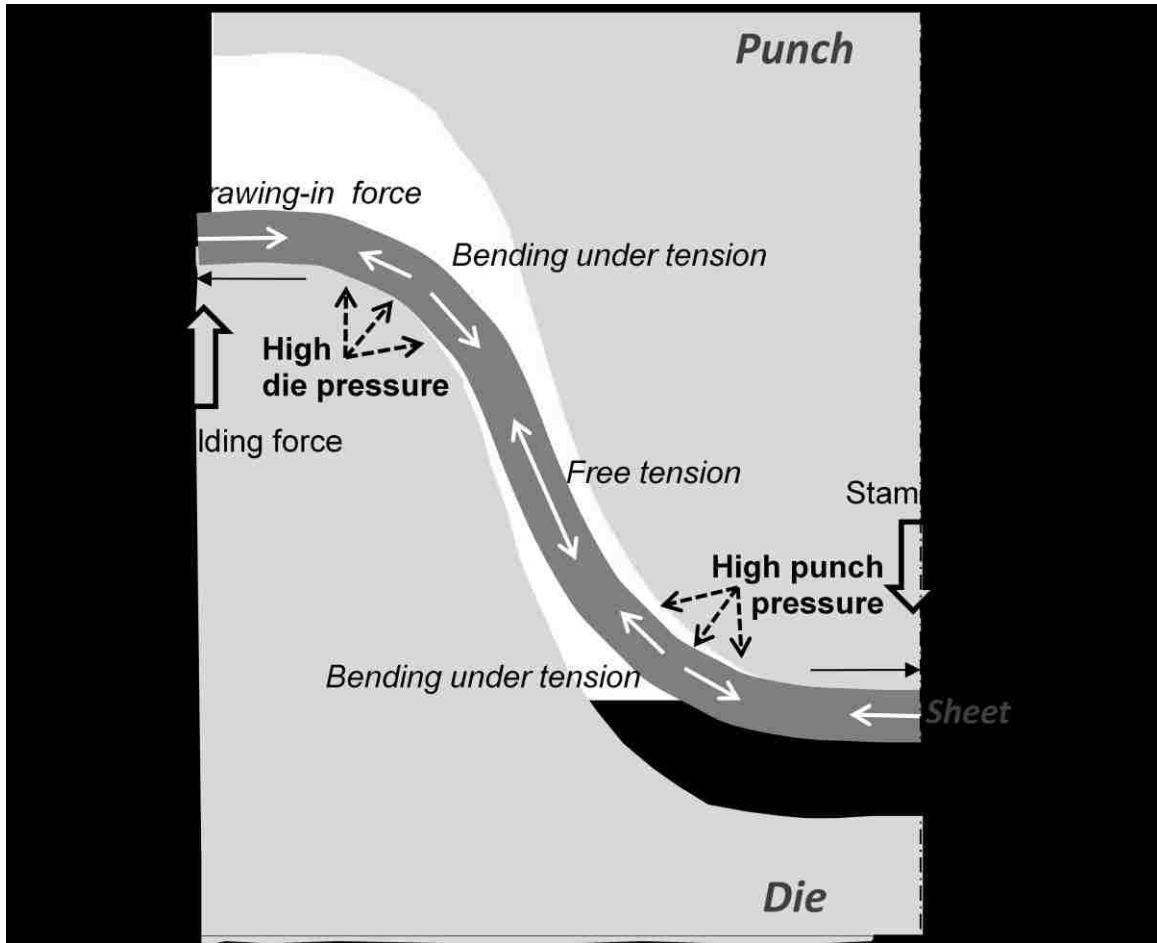


Figure 5. 1: Schematic of the forces acting on a sheet by the die during a channel stamping process.

Figure 5. 2 shows seven locations demarcated along the stamped channel. Location 1 is that part of the sheet which is clamped under the blank holder where the friction between the sheet and the die holds it in place and prevents material from being drawn into the channel. Location 7 is that part of the sheet which is in contact with the

punch and this region undergoes deformation while always in contact with the punch. Locations 2 and 6 are stretched over the radius whilst experiencing high circumferential compressive stresses in addition to tension. The frictional force is high due to the high die pressure. Locations 3 and 5 experience these same conditions in the initial phase of the stamping and then they undergo restraightening as they are drawn into the channel. Due to the differing strain states, this region experiences the greatest strain and under critical conditions of temperature or load or a combination of both, failure occurs here, either by necking or tearing. Location 4 deforms without any contact and friction, and its deformation is essentially tensile. The localised straining measured along the tensile and through-thickness directions show that the highest strain is measured at locations 3 and 5 while locations 1 and 7 experience very little strain.

In the microstructures of the stamped channel shown in Figure 4. 8, the grains on the outer side of the radius bends are elongated along the direction of the tensile strain, while those on the inside of the bend are not. Higher frictional forces at the locations of die contact will cause less strain in those regions of the sheet, and the strain necessary for the geometry will occur at the outside of the radii and the sidewalls (locations 3, 4 and 5). The less the deformation experienced in the high-friction zones, the more the other regions will strain. When this localisation causes limiting strains to develop in the bending and restraightening locations, failure by necking or tearing will occur.

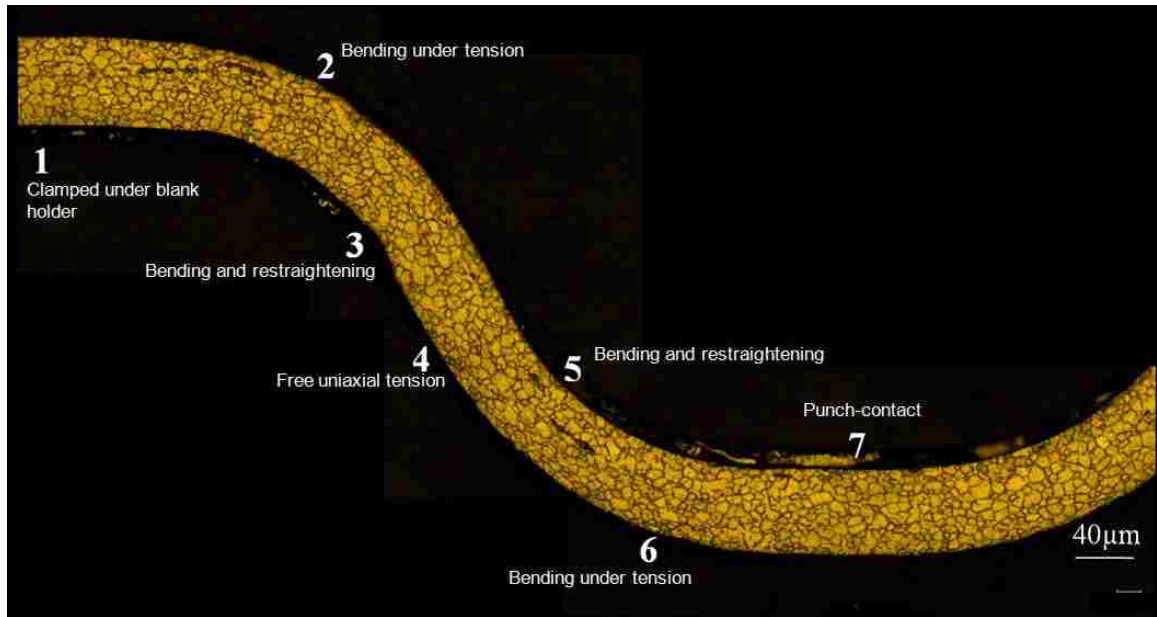


Figure 5. 2: Seven zones demarcated on the channel, where the deformation is distinctly different due to the different natures of contact in these locations and geometry of the process.

The surface roughness on the punch-side is less than on the die-side. Sliding contact between the sheet and the die causes the flattening of asperities and the surface on this side has a lower R_a value. The die-side surface first undergoes roughening on the grain-scale due to non-contact deformation and then comes into contact with the die. There is no sliding and the contact with the die is purely normal, under the stamping load. The effect of temperature on the roughness of the die-side surface is much greater than on the punch-side.

5.3 Effect of Temperature on the Process

Elevated temperatures increase the dimensional accuracy in stamping due to the reduced springback from the decrease in the yield stress with increasing temperature.

Increasing the temperature from 25 °C to 100 °C significantly increases the depth of the channels, due to the lowering of the yield stress and the onset of plastic deformation at a lower strain. Wolff and Ball (1991) [38] report the yield stress at 20 °C to be 570 MPa at an elongation of 5 %, whereas at 100 °C, the yield stress is 530 MPa at 4 % elongation. The increase in channel depth with increasing temperature is due to this.

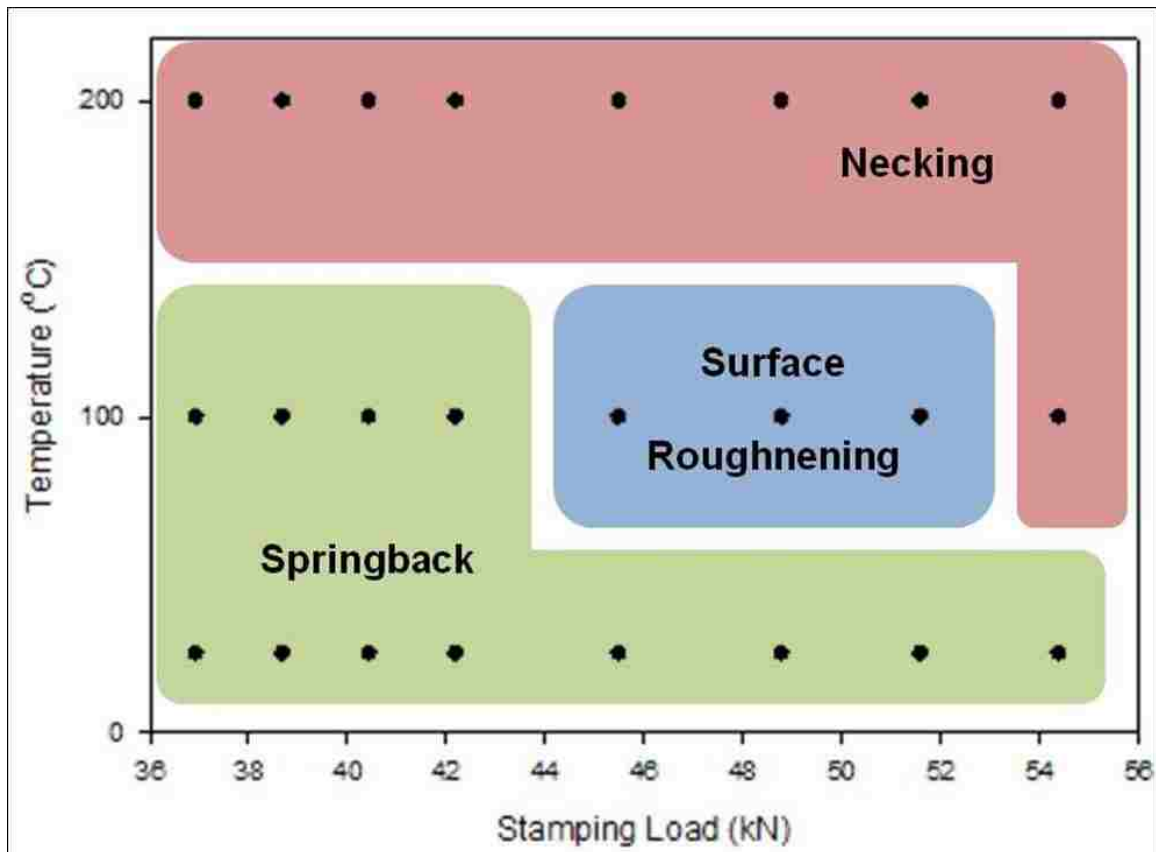


Figure 5. 3: The major limiting criteria under unlubricated warm stamping conditions as a function of temperature and stamping load.

The major limiting factors of unlubricated stamping as a function of temperature and stamping load are seen in the map in Figure 5. 3.

Coefficient of friction due to the adhesion of the sheet to the die increases with temperature. The through-thickness strain distribution does not vary significantly with an increase in stamping temperature from 25 to 100 °C, but at 200 °C, there is severe sheet thinning until failure in the regions in which there is localised straining. The increased friction between the sheet and the die causes less deformation in regions of die contact, and localised straining occurs in locations undergoing bending and restraightening and free tension.

5.4 Effect of Lubricants on the Process

Friction between the sheet and die at regions 1 and 7 (as indicated in Figure 3. 7) restricts the deformation of the sheet, and the strain is localised in the other regions of the channel. At locations 3 and 5 there is high circumferential stress on the sheet as it is bent over the radius under tension.

The absence of necking in lubricated stamping at 200 °C, where unlubricated stamping produced necking is evidence that reduced friction improves formability. High friction restricts plastic flow in the regions of die contact (regions 1 and 7, and regions 2 and 6) and causes the strain required to form the channel to localise in regions 3, 4 and 5. The greater the frictional force, the more the localisation of strain, and limiting (necking) strains develop in regions 3 and 5, causing failure.

Punch and die side surfaces formed under lubricated conditions show different morphologies not only due to the different types of contact nature but also due to the anisotropy of the mechanical properties of lamellar solid lubricants. Under sliding conditions on the punch side, the re-orientation of the lubricant particles with the basal

planes along the sliding direction occurs, creating favourable conditions for lubrication action. The transfer layers are formed due to the sliding pressure. On the other hand, purely normal contact exists on the die side and there is no time for the lubricant particles to align themselves along the surfaces before the end of the process. This causes the sheet and the lubricant to interact at the instant of contact under the stamping load with the lamellar solid particles aligned randomly. Since the hardness of the lamellar solids are significantly high along the basal plane direction [55], particles so aligned embed into the surface under the stamping load acting normal to the sheet and cause the morphology seen in Figure 4. 21. Because the hardness of the ferritic stainless steel decreases with increasing temperature, but that of the lubricant does not to the same extent, this form of damage increases with temperature. With molybdenum disulphide, transfer layers are seen on both the punch and die sides at 200 °C, which causes the increased roughness at this temperature in comparison to the other lubricants as seen in Figure 4. 14. Upon normal loading of the die over the sheet with the lubricant, this random orientation of the lubricant particles will cause the surface morphology on the die side seen in Figure 4. 21.

5.5 Surface Roughening and Evolution of Stamped Surfaces

The surface roughness on the punch-side is less than on the die-side. Sliding contact between the sheet and the die causes the flattening of asperities and the surface on this side has a lower R_a value. The die-side surface first undergoes roughening on the grain-scale due to non-contact deformation and then comes into contact with the die. There is no sliding and the contact with the die is purely normal, under the stamping load. The surface morphology seen in Figure 4. 15(d) shows large craters. The high surface

roughness measured on this surface is due to these features. The effect of temperature on the roughness of this surface is much greater than on the punch-side.

Lubrication reduces the surface roughness considerably. The increase in roughness with temperature under lubricated stamping is lower on both the punch- and the die-sides. Under perfectly lubricated conditions, the roughness on both sides of the sheet will be only due to the accommodative grain-scale movement of material in and out of the plane of the sheet, normal to the deformation. The actual roughness of the punch-side of the sheet will depend on the lubricity under sliding conditions, while the die-side roughness depends on the load-bearing capacity of the lubricant to separate the surfaces under high stamping loads.

The higher roughness on the die-side than on the punch side even under lubricating conditions is due to the higher grain-scale movement on the outside of the bending neutral axis than on the inside. Higher deformation (evidenced by the greater elongation of the grains on the die-side of the sheet) leads to a higher roughening of the surface on the grain-scale, since bending is also reported to cause more surface roughening than in free tensile deformation [64].

The manufacturing process is known to affect the corrosion resistance [5] and contact resistance [6] of the bipolar plate. Surface roughening plays an important role in the performance of the stamping as a bipolar plate. But the measure of surface roughness alone cannot determine the surface quality, and the accompanying morphology is important. For example, the grain-scale roughening will be important if the corrosion mechanism is intergranular. Sliding wear on the punch-side along with the lubricant

transfer layers may have compromised the corrosion-resistant passive layers. These can be confirmed upon further corrosion tests on the stamped sheets.

5.6 Optimum Processing Window

The channels formed at 100 °C with loads of 45 – 50 kN show the least springback with minimal strain localisation and this processing window produces optimum bipolar plate channel quality. Deeper channels are produced at this temperature than at 25 °C without a significant increase in the peaks in the strains or the excessive thinning that is observed at 200 °C.

BN, although improving the strain distribution along the channel and decreasing the surface roughness better than the other lubricants, decreases the depth of the channels by 5 µm. WS₂ does not improve the strain distribution as much as the other lubricants although the surface roughness at all temperatures is best with this lubricant. MoS₂, while although not decreasing the surface roughness to the same extent as BN and WS₂, produces the most uniform strain distribution (at 200 °C and 42.2 kN) without significantly affecting the channel depth, and has thus been selected as the optimum conditions for the stamping of these channels.

Table 5.1: The text matrix incorporating the results of this work to aid in the determination of the optimum processing window

Unlubricated	25 °C	100 °C	200 °C
36.95 kN			
38.70 kN			
40.45 kN	INSUFFICIENT	HIGH SURFACE	
42.20 kN	CHANNEL DEPTH	ROUGHNESS	NECKING
45.50 kN			
48.80 kN			
51.60 kN			
54.40 kN			
BN-lubricated	25 °C	100 °C	200 °C
36.95 kN			
38.70 kN			
40.45 kN			
42.20 kN			
45.50 kN			
48.80 kN			
51.60 kN			
54.40 kN			
WS ₂ -lubricated	25 °C	100 °C	200 °C
36.95 kN			
38.70 kN			
40.45 kN			
42.20 kN			
45.50 kN			
48.80 kN			
51.60 kN			
54.40 kN			
MoS ₂ -lubricated	25 °C	100 °C	200 °C
36.95 kN			
38.70 kN			
40.45 kN			
42.20 kN			
45.50 kN			
48.80 kN			BEST OVERALL
51.60 kN			QUALITY
54.40 kN			

These processing conditions have been selected based on formability alone. The performance of the bipolar plates stamped under these different conditions must be tested for their interfacial contact resistance, corrosion properties and mating with the gas diffusion membrane. It will then be possible to select processing conditions as a function of the performance of the bipolar plates in the fuel cell environment. This work provides useful information towards this end.

5.7 Behaviour of the Alloy

This alloy has been designed to best suit both the processing and the application. The high interstitial content present is precipitated with Ti, V and Al coarsely in order to free the chromium for the corrosion resistant passive layers. These precipitates are large, so as not to cause embrittlement and they appear to deform along with the matrix grains, as can be discerned from the stamped microstructures in Figure 4. 8 and Figure 4. 9. Their effect on the corrosion behaviour of the stamped bipolar plates in PEMFC environments remains to be seen, but there is evidence from lack of chromium in these precipitates (Figure 3. 2) that they will perform favourably.

Size effects affect the strength and deformation of a material, and this effect becomes more pronounced as the number of grains along the cross-section are less than ten. This is because grain boundaries are responsible for the formation of mobile dislocations by the strain accommodation process during deformation [65]. This leads to a lower strain hardening exponent than a bulk specimen of the same material and the uniform elongation is less as a consequence. A fine grain size is a method of reducing the

size effects to a minimum and the material considered in this work has on average 13 grains across the sheet thickness.

CHAPTER 6: Summary and Conclusions

6.1 Warm Unlubricated Stamping of Ferritic Stainless Steel

The stamping of micro-scale bipolar plate channels in 30 % Cr ferritic stainless steel was carried out in the warm forming temperature range of 25-200 °C in the stamping load range of 36-56 kN. The main conclusions of this work are as follows:

1. The dimensional accuracy of the channels is increased when the stamping was carried out at 100 °C rather than at 25 °C, but a further increase in temperature to 200 °C causes failure by localised necking. Springback effects are considerably reduced by increasing the temperature of stamping from 25 to 100 °C.

2. High stamping loads increase the localised strain (greater than 50 kN), possibly due to the increase in the frictional force, but a minimum stamping load of 45 kN is required to ensure full channel depth. Stamping load must be selected within this range for a given stamping temperature.

3. Surface roughness increases with stamping temperature and the roughness on the die-side of the channel is higher than on the punch-side.

4. 100 °C and 45 – 50 kN has been identified as the warm-forming region in which the stamping of micro-scale channels produces ferritic stainless steel bipolar plates of optimum quality.

6.2 Lubricated Warm Stamping of Ferritic Stainless Steel

The effect of solid lubricants (BN, WS₂ and MoS₂) on the stamping of metallic bipolar plate channels in 30 % Cr ferritic stainless steel foils of 75 µm thickness in the 25-200 °C temperature range was evaluated in order to determine the optimum processing conditions. The findings of this work are summarised as follows:

1. Stamping of micro-scale bipolar plate channels in ferritic stainless steel foils of 75 µm was evaluated in the temperature range of 25-200 °C and load range of 36-56 kN under unlubricated conditions and with lamellar solid lubricants.

2. Under unlubricated conditions, localised straining and surface roughness of the stamped channels increased with temperature and stamping load, and failure by necking occurred at 200 °C at all loads.

3. Channel depth increased with stamping load and springback was reduced considerably by increasing the temperature to 100 °C.

4. BN, WS₂ and MoS₂ were applied to the process and were evaluated based on the strain distribution along the channel, the surface roughness and the channel depth in the tested temperature and load range.

5. BN improved the strain distribution along the channel, especially at 200 °C, but the channel depth was less by 5 µm compared to the other lubricants.

6. WS₂ did not improve the strain distribution to the same effect as the other lubricants, but the surface roughness of the channels was the lowest at all temperatures.

7. MoS₂ produced the best strain distribution at 200 °C, and the surfaces developed transfer layers on both the punch and the die sides.

8. The optimum conditions for stamping bipolar plate channels have been identified as 200 °C, stamping load of 45 – 50 kN and MoS₂ lubrication.

6.3 Recommendations for Future Work

This work was performed in order to achieve a larger goal, which is to design the manufacturing process of this critical fuel cell component to impart optimum corrosion, electrical and structural properties. There is a strong relation between the processing conditions and the performance of bipolar plates and the first step towards understanding this is to study the effect of different manufacturing parameters on the stamping quality. Satisfactory stampings should next be subjected to corrosion tests, electrical contact resistance tests and flexural tests. An optimum processing window can then be determined based not only on stamping quality but also on the comprehensive performance of the stamping as a bipolar plate in fuel cell conditions.

REFERENCES

- [1] Y Wang, KS Chen, J Mishler, SC Cho, XC Adroher, A review of polymer electrolyte membrane fuel cells: Technology, applications, and needs on fundamental research, *Appl. Energy*, 88 (2011) 981-1007.
- [2] RC Makkus, AHH Janssen, FA de Bruijn, RKAM Mallant, Use of stainless steel for cost competitive bipolar plates in the SPFC, *J.Power Sources*, 86 (2000) 274-282.
- [3] H Tawfik, Y Hung, D Mahajan, Metal bipolar plates for PEM fuel cell—A review, *J.Power Sources*, 163 (2007) 755-767.
- [4] H Wang, JA Turner, Ferritic stainless steels as bipolar plate material for polymer electrolyte membrane fuel cells, *J.Power Sources*, 128 (2004) 193-200.
- [5] E Dur, ÖN Cora, M Koç, Effect of manufacturing conditions on the corrosion resistance behavior of metallic bipolar plates in proton exchange membrane fuel cells, *J.Power Sources*, 196 (2011) 1235-1241.
- [6] C Turan, ÖN Cora, M Koç, Effect of manufacturing processes on contact resistance characteristics of metallic bipolar plates in PEM fuel cells, *Int. J. Hydrogen Energy*, 36 (2011) 12370-12380.
- [7] S Mahabunphachai, ON Cora, M Koç, Effect of manufacturing processes on formability and surface topography of proton exchange membrane fuel cell metallic bipolar plates, *J.Power Sources*, 195 (2010) 5269-5277.
- [8] GM Goodwin, Application of Strain Analysis to Sheet Metal Forming Problems in the Press Shop, SAE Technical Paper No. 680093, 1968.
- [9] SP Keeler, WA Backofen, Plastic instability and fracture in sheets stretched over rigid punches, *Trans. ASM.*, 56 (1963) 25-48.
- [10] SP Keeler, Determination of forming limits in automotive stampings, *Sheet Met. Ind.*, 42 (1965) 683-691.
- [11] AK Ghosh, SS Hecker, Stretching limits in sheet metals: In-plane versus out-of-plane deformation, *Metallurgical Transactions*, 5 (1974) 2161-2164.
- [12] Z Marciniak, K Kuczyński, Limit strains in the processes of stretch-forming sheet metal, *Int.J.Mech.Sci.*, 9 (1967) 609-612.

- [13] AK Ghosh, SS Hecker, Failure in thin sheets stretched over rigid punches, *Metallurgical Transactions A*, 6 (1975) 1065-1074.
- [14] AK Ghosh, A method for determining the coefficient of friction in punch stretching of sheet metals, *Int.J.Mech.Sci.*, 19 (1977) 457-470.
- [15] B Kaftanoğlu, Determination of coefficient of friction under conditions of deep-drawing and stretch forming, *Wear*, 25 (1973) 177-188.
- [16] WA Backofen, *Deformation processing*, 1972, Addison-Wesley, Reading, MA, U.S.A.
- [17] R Hill, On discontinuous plastic states, with special reference to localized necking in thin sheets, *J.Mech.Phys.Solids.*, 1 (1952) 19-30.
- [18] SL Semiatin, JJ Jonas, *Formability and Workability of Metals: Plastic Instability and Flow Localization*, 1984, American Society for Metals, Metals Park, Ohio 44073, U.S.A.
- [19] GE Dieter, *Workability Testing Techniques*, 1984, American Society for Metals, Metals Park, Ohio 44073, U.S.A.
- [20] MK Mickalich, ML Wenner, Calculation of springback and its variation in channel forming operations, *SAE Technical Paper No. 880526*, 1988, 99–100.
- [21] ML Wenner, On work hardening and springback in plane strain draw forming, *J. Applied Metalworking*, 2 (1983) 277-287.
- [22] RA Ayres, ML Wenner, Strain and strain-rate hardening effects in punch stretching of 5182-0 aluminum at elevated temperatures, *Metallurgical Transactions A*, 10 (1979) 41-46.
- [23] B Kaftanoglu, JM Alexander, On quasistatic axisymmetrical stretch forming, *Int.J.Mech.Sci.*, 12 (1970) 1065-1084.
- [24] H Darendeliler, T Altan, Analysis of axisymmetric cup drawing in relation to friction, *J.Mater.Process.Technol.*, 58 (1996) 293-301.
- [25] PL Charpentier, Influence of punch curvature on the stretching limits of sheet steel, *Metallurgical Transactions A*, 6 (1975) 1665-1669.
- [26] EJ Obermeyer, SA Majlessi, A review of recent advances in the application of blank-holder force towards improving the forming limits of sheet metal parts, *J.Mater.Process.Technol.*, 75 (1998) 222-234.

- [27] B Kaftanoğlu, Determination of coefficient of friction under conditions of deep-drawing and stretch forming, *Wear*, 25 (1973) 177-188.
- [28] JA Schey, *Tribology in Metalworking: Friction, Lubrication and Wear*, 1983 American Society for Metals, Metals Park, Ohio 44073, U.S.A.
- [29] AL Schaeffler, Constitution diagram for stainless steel weld metal, *Metal Progress*, 56 (1949) 680-680B.
- [30] RO Williams, HW Paxton, The Nature of Ageing of Binary Iron-Chromium Alloys Around 500 °C, *J. Iron Steel Inst.*, (1957) 358-374.
- [31] R Lagneborg, Deformation in an iron-30% chromium alloy aged at 475°C, *Acta Metallurgica*, 15 (1967) 1737-1745.
- [32] LF Spencer, Welding of Stainless Steel Compositions, *Steel Proc. March*, 38 (1952) 244-249.
- [33] JJ Heger, Stainless Steels- Their Characteristics, *Steel*, 123 (1948) 71.
- [34] C Zener, as quoted by CS Smith, *Trans. AIME*, 175 (1948) 47-51.
- [35] RE Schramm, RP Reed, Stacking fault energies of seven commercial austenitic stainless steels, *Metallurgical Transactions A*, 6 (1975) 1345-1351.
- [36] ACTM Van Zwieten, JH Bulloch, Some considerations on the toughness properties of ferritic stainless steels—A brief review, *Int.J.Pressure Vessels Piping*, 56 (1993) 1-31.
- [37] IM Wolff, A Ball, Substitutional alloying and deformation modes in high chromium ferritic alloys, *Metallurgical Transactions A*, 23 (1992) 627-638.
- [38] IM Wolfe, A Ball, Ductility in high-chromium super-ferritic alloys—II. Plastic deformation and crack-zone shielding, *Acta Metallurgica et Materialia*, 39 (1991) 2771-2781.
- [39] H Thielsch, Physical and welding metallurgy of chromium stainless steels, *The Welding Journal*, 30 (1951) 209-250.
- [40] RWK Honeycombe, *The plastic deformation of metals*, 2nd ed., 1984 Edward Arnold, Baltimore, MD, U.S.A.
- [41] W Sylwestrowicz, EO Hall. The deformation and ageing of Mild steel, *Proceedings of the Physical Society*.Section B. 64 (1951) 495-502.

- [42] EO Hall. The deformation and ageing of mild steel: II Characteristics of the Lüders deformation, Proceedings of the Physical Society. Section B. 64 (1951) 742-747.
- [43] A Portevin, F Le-Chatelier. Sur un phénomène observé lors de l'essai de traction d'alliages en cours de transformation, Comptes Rendus de l'Académie des Sciences, Paris, 176 (1923) 507-510.
- [44] D Hull, DJ Bacon, Introduction to Dislocations, 1984, Pergamon Press, Oxfordshire, U.K.
- [45] F Nabarro. Mechanical effects of carbon in iron, Proceedings of the Physical Society (1948) 38-45.
- [46] R Gullberg, A Plumtree. Static strain aging in an Fe-25 pct Cr alloy, Metallurgical Transactions. 4 (1973) 1427-1429.
- [47] S Hartley. Strain-ageing in tantalum, Acta Metallurgica. 14 (1966) 1237-1246.
- [48] AH Cottrell, BA Bilby. Dislocation theory of yielding and strain ageing of iron, Proceedings of the Physical Society. Section A. 62 (1949) 49-62.
- [49] E Pink, A Grinberg. Serrated flow in a ferritic stainless steel, Materials Science and Engineering. 51 (1981) 1-8.
- [50] AH Cottrell, MA Jaswon. Distribution of Solute Atoms Round a Slow Dislocation, Proceedings of the Royal Society of London. Series A, Mathematical and Physical Sciences. 199 (1949) pp. 104-114.
- [51] RF Deacon, JF Goodman. Lubrication by lamellar solids, Proceedings of the Royal Society of London. Series A, Mathematical and Physical Sciences. (1958) 464-482.
- [52] WO Winer. Molybdenum disulfide as a lubricant: A review of the fundamental knowledge, Wear. 10 (1967) 422-452.
- [53] SV Prasad, JS Zabinski, NT McDevitt. Friction behavior of pulsed laser deposited tungsten disulfide films(C), S T L E Tribology Transactions. 38 (1995) 57-62.
- [54] SF Murray, SJ Calabrese. Effect of solid lubricants on low speed sliding behavior of silicon nitride at temperatures to 800°C, Lubrication Engineering. 49 (1993) 955-964.
- [55] J.K. Lancaster, Anisotropy in the mechanical properties of lamellar solids and its effect on wear and transfer, Wear. 9 (1966) 169-188.

- [56] ER Braithwaite, *Solid Lubricants and Surfaces*, Pergamon Press, Oxford, U.K., 1964.
- [57] WF Hosford. Sheet metal forming: a review, *JOM*. 51 (1999) 39.
- [58] L Peng, et al. Fabrication of metallic bipolar plates for proton exchange membrane fuel cell by flexible forming process-numerical simulations and experiments, *J. Fuel Cell Sc. Tech.* 7 (2010) 0310091-0310099.
- [59] CC Silva, JP Farias, HC Miranda, RF Guimarães, JWA Menezes, MAM Neto. Microstructural characterization of the HAZ in AISI 444 ferritic stainless steel welds, *Mater Charact.* 59 (2008) 528-533.
- [60] A Plumtree, R Gullberg. Strain Ageing in Ferritic Chromium Steels. *Scand J Metall.* 2 (1973) 44-48.
- [61] JM Martin, T Le Mogne, C Chassagnette, MN Gardos. Friction of hexagonal boron nitride in various environments, *Tribol.Trans.* 35 (1992) 462-472.
- [62] WJ Bartz, K Müller. Investigations on the lubricating effectiveness of molybdenum disulfide, *Wear.* 20 (1972) 371-379.
- [63] BS Levy, CJ Van Tyne. Predicting breakage on a die radius with a straight bend axis during sheet forming, *J.Mater.Process.Technol.* 209 (2009) 2038-2046.
- [64] D Raabe, M Sachtleber, H Weiland, G Scheele, Z Zhao. Grain-scale micromechanics of polycrystal surfaces during plastic straining, *Acta Materialia.* 51 (2003) 1539-1560.
- [65] MF Ashby. The deformation of plastically non-homogeneous alloys, *Philosophical magazine.A*, 21 (1970) 399-424.

VITA AUCTORIS

Name Lakshmi Ravi Narayan

Birth 1986, Bangalore, India

Education Bachelor of Engineering (B. E.), Production Engineering
Birla Institute of Technology, Mesra, India
2006-2010

Master of Applied Science (M. A. Sc.), Engineering Materials
University of Windsor, Windsor, ON, Canada
2010-2012

Collaborative reports with industry based on this work

1. L. R. Narayan, A. T. Morales, A. T. Alpas, “Warm Stamping of 30 % Cr Ferritic Stainless Steel for Bipolar Plates” General Motors Collaborative Report, 2011, CL – 11/241/CML.

2. L. R. Narayan, A. T. Morales, A. T. Alpas, “Solid Lubricants for the Warm Stamping of 30 % Cr Ferritic Stainless Steel for Bipolar Plates” General Motors Collaborative Report, 2012

Conference presentations based on this work:

1. L. R. Narayan, A. T. Morales, A. T. Alpas, “Warm Stamping of 30 % Cr Ferritic Stainless Steel for Bipolar Plates”, SAE World Congress 2012, April 24, Detroit MI.

2. L. R. Narayan, A. T. Morales, A. T. Alpas, “Solid Lubricants for the Warm Stamping of 30 % Cr Ferritic Stainless Steel for Bipolar Plates”, STLE Annual Meeting and Exhibition 2012, May 10, St. Louis, MO.

3. L. R. Narayan, A. T. Morales, A. T. Alpas, “Solid Lubricants for Warm Stamping of Metallic Bipolar Plates”, poster presented at North American Deep Drawing Research Group (NADDRG) Fall Symposium May 15, 2012.